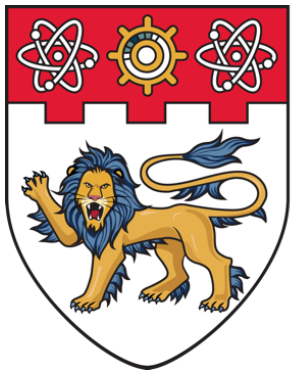

NANYANG TECHNOLOGICAL UNIVERSITY
SINGAPORE

ON THE ORIGIN OF FERROELECTRIC PHOTOVOLTAIC EFFECTS IN VERTICAL $BiFeO_3$ HETEROSTRUCTURES

AMR AHMED KORANY ABDELSAMIE

SCHOOL OF MATERIALS SCIENCE AND ENGINEERING

2021

ON THE ORIGIN OF FERROELECTRIC PHOTOVOLTAIC EFFECTS IN VERTICAL $BiFeO_3$ HETEROSTRUCTURES

AMR AHMED KORANY ABDELSAMIE

SCHOOL OF MATERIALS SCIENCE AND ENGINEERING

A thesis submitted to the Nanyang Technological University
in partial fulfilment of the requirement for the degree of
Doctor of Philosophy

2021

Statement of Originality

I hereby certify that the work embodied in this thesis is the result of original research, is free of plagiarised materials, and has not been submitted for a higher degree to any other University or Institution.

05 Aug 2021

. . . . . .
Date

. . . . . .
Amr Ahmed Korany Abdelsamie

Supervisor Declaration Statement

I have reviewed the content and presentation style of this thesis and declare it is free of plagiarism and of sufficient grammatical clarity to be examined. To the best of my knowledge, the research and writing are those of the candidate except as acknowledged in the Author Attribution Statement. I confirm that the investigations were conducted in accord with the ethics policies and integrity standards of Nanyang Technological University and that the research data are presented honestly and without prejudice.

05 Aug 2021

. . . . . .
Date

. . . . . .
A/Prof. Li Shuzhou

Authorship Attribution Statement

This thesis contains materials from one paper published in the following peer-reviewed journal in which I am listed as first co-author as follows.

Sections 5.2 and 5.3 from chapter 5 are published as Yiqi Hu, Amr Abdelsamie, et al., Effect of polarization rotation on the optical and photovoltaic properties of $BiFeO_3$ thin films, 2021 J. Phys.: Condens. Matter 33 354002, DOI: 10.1088/1361-648X/ac0d19.

The contributions of the co-authors are as follows:

- Prof. You Lu edited and revised the manuscript.
- Prof. You Lu and I proposed the idea and designed and performed the photovoltaic and linearly polarized UV-vis absorption experiments at the School of Materials Science and Engineering, NTU.
- Prof. You Lu prepared the La-doped $BiFeO_3$ thin films.
- I co-wrote the manuscript draft with Yiqi Hu and Prof. You Lu with input from all coauthors.

05 Aug 2021

. . . . . .

Date

. . . . . .

Amr Ahmed Korany Abdelsamie

Abstract

Developing clean and sustainable energy sources has become increasingly important to humankind. Specifically, solar energy which is abundant and can be directly converted into electricity that is essential for modern life. *Photovoltaic cells* (PVs) are the constructed platforms to convert sunlight into electrical power. A typical solar cell consists of *p-type/n-type* bilayer made of silicon. In these devices, the emergent electrochemical potential difference at their interface establishes an electric field that assists in separating the photoexcited charges. This implies that the output photovoltage is limited by the material's bandgap. In fact, in terms of efficiencies, Shockley-Queisser (SQ) model anticipated maximum power conversion efficiency of 33.7% in semiconductor of bandgap 1.34 eV. Unfortunately, this theoretical limit is approaching, and alternative solutions are required. On the other hand, *Bulk photovoltaic cells* are potential substitutes to junction solar cells. They rely on noncentrosymmetric crystals, such as *ferroelectrics*, as an active layer. In these cells, the photoexcited charge carriers can be separated throughout the bulk of the crystal. Accordingly, the output photovoltage is not related to the material's bandgap, and hence sky-high open-circuit voltages can be reached. Moreover, the construction of the cell is simpler if compared to the commercial solar cells comprising pn- or pin-junctions or tandem cells.

Despite its discovery in 1956, it was only 2009 when the interest in bulk photovoltaic effects was renewed upon the emergence of switchable PV behavior in $BiFeO_3$ crystals. Since then, much effort has been dedicated in attempt to explain the mechanism of photovoltaic effects in ferroelectrics since the cell structure is complicated assuming the existence of multiple potential charge separation sources. This resulted in divided opinion on whether Schottky barrier, domain wall, bulk effects or even a combination of these effects are behind such interesting behavior that can be termed *ferroelectric photovoltaic effect*. This motivated this work which employs the prototypical ferroelectric bismuth ferrite ($BiFeO_3$) films sandwiched between two metallic electrodes.

This experimental dissertation aims at the fabrication and characterization of single crystalline $BiFeO_3$-based photovoltaic cells. For this, a physical vapor deposition technique, namely, pulsed laser deposition (PLD), is adopted to fabricate the devices. Bismuth ferrite films were first probed and analyzed for their crystal and ferroelectric structures. Afterwards, the electrical properties were examined under either white or monochromatic lights revealing the photovoltaic property of the devices under test.

A direct evidence of the predomination of Schottky barrier is revealed in $BiFeO_3$ by illuminating the devices with unpolarized white light. By systemically studying the thickness-dependent photovoltaic behavior in $BiFeO_3$ films ranging from 38 to 500 nm, the thinnest film showed a one order-of-magnitude higher current density. The measured behavior indicates the PV response stemmed from the interface effect. In this context, the thinner the film, the more efficient is the charge carrier collection. Also, the top interface was modulated from Schottky to ohmic characters which further endorsed the obligation of Schottky barrier presence to promote photovoltaic behavior in ferroelectric photovoltaics. Furthermore, oscillating photocurrents are measured in vertical $BiFeO_3$ capacitors under linearly polarized light. When the sample is illuminated by linearly polarized white or 520 nm lights, the photocurrent is maximized [-110], or normal to in-plane polarization. This is found to be consistent with the linear dichroism in $BiFeO_3$ and indicates the domination of interface band-bending PV. On the other hand, shone by linearly polarized 405 nm laser, bulk PV came to picture manifested by the photocurrent spiking along the in-plane polarization which was confirmed by the theoretical calculations of bulk PV.

The findings provide insights into fundamental and technological perspectives of the ferroelectric photovoltaic effects. Fundamentally, it offers new understanding of light-matter interaction in ferroelectrics revealing two competitive phenomena, namely, linear dichroism and bulk photovoltaic effect. Moreover, the outcomes pave the way to enhance the PV output in ferroelectrics for solar cells and optoelectronic applications. Also, it establishes grounds for developing self-powered linearly polarized light photodetectors.

Lay Summary

A growing demand to find cleaner and more efficient energy sources has increased in respond to the *energy crisis* occurred during 1970s. Energy crisis arose when the oil prices were raised by around 70% of its original price leading to fuel shortages, particularly in the western world. Indeed, solar energy is considered as one of the promising energy source alternatives to fulfill such demands. Solar radiation includes infrared, visible, and ultraviolet lights that can be converted into electrical power. Solar cells, or solar *photovoltaics*, are devices designed to turn the sunlight into electricity. Mankind invented solar cells through complicated chemical and physical methods. These solar cells are composed of two-layer semiconductors which contain opposite charges. The driving mechanism of the light-to-electricity is the potential force at the interface between the two regions due to the charge contrast. Unfortunately, the theoretical value of the power conversion efficiency of such devices has reached the limit. Therefore, a replacement to traditional photovoltaics is much in demand.

The simplest way to construct solar cells is by incorporating foreign species into silicon (the most common commercial material in solar cell market). These dopants provide negatively charged electrons in one side and positively charged holes (or absence of electrons) in the other side. Consequently, a potential difference develops at the junction, thus called *junction solar cells*. Based on this, sunlight is absorbed by the semiconducting material. Then, loose electrons and holes are produced. Afterwards, the built-in electric field pushes the charges to the external circuit generating a constant electric current as long as the device is under light.

However, there exist “inherent” solar cells, called *bulk photovoltaic cells*. Photovoltaics adopting ferroelectric materials can also generate photocurrents. Ferroelectrics are those materials that spontaneously possess electric polarization and are widely used in sensors and memories. A single layer comprising ferroelectric material can innately separate electron-hole pairs yielding an electric current without the involvement in complicated processing. In contrast to the traditional solar cell, the driving force of the bulk photovoltaic

mechanism is distributed throughout the bulk of the ferroelectric material. It is worth mentioning that the electric field associated with the ferroelectric polarization is higher in magnitude. Thus, a major benefit of this cell is that the high output voltages are expected to develop across the crystal.

First discovered in 1954, ferroelectric solar cells have been researched, yet still exhibiting low efficiencies compared to the conventional ones. One major reason is the lack of understanding of the origin. In other words, bulk photovoltaic mechanism is usually confused with the junction at the ferroelectric/metal interface. In fact, the ferroelectric/metal interface resembles the junction solar cell which complicates the ferroelectric solar cell. It is foggy whether the ultimate ferroelectric photovoltaic output originates from either source. Therefore, addressing this problem may lead to a cooperative bulk and junction photovoltaic mechanisms in the same cell. However, researchers have not treated this problem in detail which hinders its application to real world.

This dissertation researches the origin of the photovoltaic mechanism in ferroelectrics. In this premise, the prototypical ferroelectric material belonging to the perovskite oxide family, bismuth ferrite, is exploited. This substance is strong in terms of ferroelectric and optical properties. Several research strategies were designed and applied in order to attempt to clarify the confusion in the field. This encompasses tuning the structure of the solar cell and testing the output under white light and single-colored lasers. The key findings of this work are twofold. Firstly, by exposing the ferroelectric photovoltaic cell to the sunlight, the junction photovoltaic dominates the measured output. On the other hand, if laser source of high energy is adopted, the bulk effects come to the picture. Thus, the findings provide a route to enhance the PV output in ferroelectrics for solar cells and optoelectronic applications.

Acknowledgements

This dissertation would not have been possible without funding from Nanyang Technological University (NTU) that awarded me the Singapore International Graduate Award (SINGA) scholarship to pursue my PhD at the School of Materials Science and Engineering (MSE).

First, I would like to express my gratitude to my supervisor, Prof. Wang Junling, for giving me the opportunity to be a part of his research group. Thank you for introducing me to the $BiFeO_3$ world. I am also grateful to Prof. Li Shuzhou who took the responsibility after Prof. Wang moved to the Southern University of Science and Technology.

Special thanks are conveyed to Prof. You Lu for assisting, training and giving me considerable counselling during my PhD time. I acknowledge that without him, this work wouldn't come to light. I also would like to thank Dr. Wang Le and Dr. Chang Lei for helping and training me while initiating my PhD project. Also, I would like to thank my group members and lab mates who created good and comfortable atmosphere during my PhD work. This includes Dr. Zhou Shuang, Dr. Zhou Yang, Ms. Yang Tiantian and Ms. Zhang Xiyuan. I would like to express my sincere gratitude and appreciation to Dr. Guo Rui, research fellow at National University of Singapore, for her endless help and support during my PhD period.

I would also like to thank my friends in NTU and Singapore: Ahmed Said, John Henawy, Ahmed Samir, Omar Abdelrahman and Ayman Shahin. Also, special gratitude goes to the two precious friends I made in Singapore: Wissal Bouaicha and Nihed Lasmar. Thank you all for your friendship and efforts to make my PhD time much enjoyable.

Lastly, but not the least, I would like to express my deep gratitude to my parents and my siblings for their support in all aspects of life.

Table of Contents

Table Captions

Figure Captions

Figure 1.1: Concept of light-to-electricity conversion in two types of solar cells. (a) Conventional solar cell. In this type of solar cells, photoexcited electron-hole pairs are separated by the electric field at the p-n junctions (usually, doped silicon). (b) Bulk photovoltaic cell. Here, charge carriers are separated throughout the whole bulk of spatially homogeneous material and hence given the term (bulk). The driving mechanism of the charge separation in bulk PVs is the crystal asymmetry. Therefore, crystals lacking the center of symmetry are (natural) solar cells.

Figure 2.1: Typical polarization-electric field loop of the $BaTiO_3$ ceramic. Ferroelectricity stems from the relative shift of the Ti^{3+} ion in the oxygen octahedron to either up or down with respect to the initial position in perfect perovskites. However, applying an electric field above the coercive field $\mp E_c$ can switch the Ti cation between the two positions.

Figure 2.2: Electrostatic description of ferroelectrics. **(a)** Freestanding ferroelectric layer with a developed depolarization field E_{dep} opposite to the polarization direction P. **(b)** The polarization is screened by the free charges in metallic electrodes in contact with it leading to a weakened E_{dep}.

Figure 2.3: Schottky barrier at metal/semiconductor interface. The band diagram of free-standing metal **(a)** and intrinsic semiconductor **(b)**. **(c)** Band bending at the metal-semiconductor after charge reorganization.

Figure 2.4: Band diagram representation of ferroelectric material in two possible polarization states. **(a)** and **(b)** The band edge curves down and up at the head and tail, respectively. Switchable conduction behavior of ferroelectrics in **(c)** and **(d)**. In fact, sandwiching a ferroelectric layer between two metal electrodes gives rise to back-to-back diode effects, or switchable diode effects.

Figure 2.5: Depiction illustrates the construction of the unit cell of $BiFeO_3$ crystal. It is characterized by two distorted perovskite unit cells leading to a rhombohedral unit. However, the structure can be simplified by describing it in terms of pseudocubic (pc) notation. In pseudocubic notation, the two oxygen octahedra are tilted in opposite directions with respect to $[111]_{pc}$ direction. In addition, the spins at the Fe^{3+} sites couple antiferromagnetically. The pseudocubic and rhombohedral axes are given in the inset images.

Figure 2.6: Polarization-electric field (PE) hysteresis loop of $BiFeO_3$. **(a)** PE loops of $BiFeO_3$ epitaxial films measured along three different orientations. Crystal orientation-dependent remnant polarization show evolution from 60 $\mu C/cm^2$ along $[001]_{pc}$ to 100 $\mu C/cm^2$ towards $[111]_{pc}$. **(b)** PE loop of single $BiFeO_3$ crystal demonstrating a rectangular loop.

Figure 2.7: Ferroelectric domain structure of $BiFeO_3$. **(a)** Eight possible orientations of total polarization. Schematic of two-adjacent-domain configurations of $BiFeO_3$ leading to formation of **(b)** 71^o, **(c)** 109^o and **(d)** 180^o domain walls.

Figure 2.8: Magnetic structure of $BiFeO_3$. **(a)** Unit cell of $BiFeO_3$ with the antiferromagnetic axis L normal to the canted local moment M within the same plane and total ferroelectric polarization P perpendicular to the AFM plane. **(b)** The spin cycloid forming sinusoidal wave propagating along $<110>_{pc}$ with wavelength ~62 nm.

Figure 2.9: Classification of photovoltaic effects based on the mechanism of the separation of photoexcited charges. **(a)** Barrier photovoltaic effect produced in junction-based cells such as doped silicon *pn*-junctions (inset). The current-voltage characteristics are governed by the ideal diode giving rise to the IV curve assigned as "Dark". The curve is shifted to "Illumination" upon illuminating the cell by light of energy larger than the material's bandgap. **(b)** Bulk photovoltaic effect (BPVE) in homogeneous materials lacking center of symmetry. The electrical conduction is characterized by linear behavior since the material is uniform as plotted by the black line. The advantage of BPVE is the switchability

following the reversal of the center of symmetry yielding a bipolar photovoltaic response (blue and red lines).

Figure 2.10: E Early photovoltaic current measured in ferroelectric single crystals. **(a)** Steady-state photocurrent measured in $BaTiO_3$ single crystal while studying the pyroelectric effect. **(b)** Photovoltaic current along negative direction of polarization axis in $LiNbO_3$.

Figure 2.11: Ballistic mechanism of bulk photovoltaic effect. **(a)** Asymmetric potential barrier at the impurity center as proposed by Glass to explain the bulk photovoltaic effect in iron-doped lithium niobate Fe:$LiNbO_3$. Effect of the symmetry of the crystal on the photo-excited charge carriers in **(b)** Centrosymmetric and **(c)** Non-centrosymmetric crystals. Normally, the charge carriers are thermalized to the bottom of the conduction band in centrosymmetric crystals owing to the inelastic scattering. In contrast, noncentrosymmetry can shift the carriers in conduction band resulting in sizable photocurrents.

Figure 2.12: Angular dependence of the bulk photocurrent. **(a)** First observation of the dependence of the photocurrent on the light polarization in $BaTiO_3$ crystals. Perpendicular light polarizations gave rise to currents of opposite directions. Sinusoidal behavior of the photocurrent in linearly polarized light illuminated Fe-doped $LiNbO_3$ crystal along z-direction **(b)**, y-direction **(c)** and x-direction **(d)**.

Figure 2.13: Dependence of bulk photovoltaic response on the light intensity and temperature. Light intensity dependence of the IV curves of low photoconductivity ferroelectric in **(a)** Fe:$LaNiO_3$ under 473 nm laser and high photoconductivity in **(b)** Fe:$KNbO_3$ under 488 nm illumination. Temperature-dependence of the photovoltaic behavior in **(c)** $BaTiO_3$ crystal[105] and **(d)** $BiFeO_3$ thin films.

Figure 2.14: Role of defects in bulk photovoltaic effects in $BiFeO_3$ single crystal. Defects are intentionally introduced to the crystal via controlling the Bi content. **(a)** Crystal with

minimal Bi ions exhibits highest photoconductivity at wavelengths below bandgap which indicates the activity of the induced gap states by Bi vacancies. **(b)** No photocurrent is detected at the corresponding wavelengths.

Figure 2. 15: Ferroelectric photovoltaic device configurations. **(a)** Planar configuration where the active layer is directly illuminated while the current is measured along the in-plane direction. **(b)** Vertical configuration with the current is collected parallel to the illumination direction.

Figure 2.16: Impact of domain walls on the photovoltaic output in $BiFeO_3$ films with periodic 71° DWs. Devices under test shined by unpolarized white light with co-planar electrodes parallel **(a)** and perpendicular **(b)** to the domain walls generating photovoltaic response **(c)** and photoconductivity **(d)**, respectively. **(e)** The behavior was explained solely by electrostatic potential step at the DWs. Employing linearly polarized 405 nm laser source, a sizable PV output measured in both directions which is explained by contributions from the local noncentrosymmetry as well as the band-bending at the DWs **(f)**. On contrary, the measured effect was interpreted by the bulk PV mechanism in which the DWs controlling the overall photoconductivity **(g)**. Hence, the device was modeled as resistors connected in either series or parallel giving rise to anisotropic PV response.

Figure 2.17: Ferroelectric polarization-modulated Schottky barrier photovoltaic effect in $Pt/BiFeO_3/SrRuO_3$ heterostructure. Current density-voltage curves in dark and light conditions associated with the ferroelectric polarization in up- **(a)** and down- **(b)** states. The switchable behavior was explained by the modulation of Schottky barrier from up **(c)** to down **(d)** states. Also, monitoring the photocurrent evolution with the applied voltage pulses led to a hysteretic behavior superimposed on the polarization-electric field loops **(e)**.

Figure 2.18: Ballistic current mechanism measured in $BaTiO_3$ thin films. **(a)** IV curves measured in Pt/(20 nm)$BaTiO_3$/Pt stack under different light intensities revealing ~1% efficiency. The $BaTiO_3$ thickness scaling of the V_{oc} **(b)** and photocurrent **(c)** demonstrate

the PV enhancement after exceeding the mean free path of the nonthermalized charge carriers **(d)**.

Figure 3.1: The operating principle of the pulsed laser deposition (PLD). The laser beam (yellowish) impinges the rotating target ablating ions from its surface. The ablated material (Purple) is released towards the substrate surface. Finally, the thin film is formed on top of the substrate.

Figure 3.2: Nucleation of vapor species on single crystal substrate. **(a)** Schematic representation of the atomic processes involved in the film growth. Orange circles array represents the substrate while the blue color indicates foreigner species. However, the nucleus shape depends on the contact angle with the substrate material resulting in **(b)** Non-wetting, **(c)** incomplete wetting and **(d)** Good wetting phenomena.

Figure 3.3: Types of growth of epitaxial thin films (blue layer) on bulky substrate (orange colored base). **(a)** Homoepitaxy where the grown thin film is identical to the substrate material yielding a coherent growth. **(b)** Heteroepitaxy. In this kind of growth, the film chemical composition differs from the substrate. The mismatch in crystal lattice parameters between the film and substrate substances induces strain effects at the film side.

Figure 3.4: Basic modes of epitaxial thin films growth. **(a)** Volmer-Veber or the island mode. **(b)** Frank-Van der Merwe or the layer-by-layer mode. **(c)** Stranski-Krastanov or the layer plus island mode. **(d)** Step-flow growth mode.

Figure 3.5: Concept of x-ray diffraction (XRD). **(a)** XRD in real space where the real crystal exists and d_{hkl} is the separation between the planes. Bragg's law is fulfilled when the path difference between the incident and scattered beams ($2d_{hkl}sin\theta$) is an integral number of the X-rays wavelength. **(b)** XRD in reciprocal space in which each blue ball corresponds to family of parallel crystallographic planes. Here, $G_{hkl}$is the reciprocal lattice vector and is defined by ($|G_{hkl}| = 2\pi/d_{hkl}$).

Figure 3.6: High-resolution x-ray diffraction on epilayer (blue)-substrate (orange). **(a)** Euler cradle. **(b)** Symmetric $2\theta - \omega$ scan. In this, the source and detector move simultaneously with $\omega = 2\theta/2$ maintaining the scattering vector Q direction fixed normal to the sample surface. Hence, structural information from the out-of-plane direction can be extracted. (c) Rocking curve scan. The source move while fixing the detector.

Figure 3.7: Working principle of atomic force microscope (AFM). **(a)** Setup of a typical AFM in the tapping mode. Tip attached to a vibrating cantilever that raster the surface of the sample. Cantilever deflections are detected by means of laser reflected off the back side of the cantilever to a 2D 4-segmented photodiode which are differentiated into vertical deflections **(b)** and lateral torsions **(c)**.

Figure 3.8: Color code of **(a)** IP PFM and **(b)** OOP PFM where the cantilever is set parallel to $[-110]_{pc}$ direction.

Figure 3.9: Sawyer-Tower circuit. It consists of two capacitors connected in series; the reference capacitor and the ferroelectric capacitor under test. A triangular wave voltage is applied to the sample. The total current due to charge motions is integrated over time. This current has contributions from charge displacement and leakage mechanisms. At the end, the remnant polarization and coercive field can be extracted.

Figure 3.10: (a) Spectra of the halogen lamp used to provide white light to the sample surface. **(b)** Working wavelength range of the linear polarizer used in this thesis.

Figure 4.1: Lattice mismatch in BFO/LSMO/STO heterostructure. **(a)** Unit cells of bulk BFO, LSMO and STO before growth demonstrating compressive strain in BFO grown on STO in contrast to the tensile strain induced in LSMO/STO. **(b)** After growth, the mismatch is accommodated by distorting the crystal lattices to maintain the unit cell volume constant. LSMO unit cell is elongated in-plane while compressed along c-axis. The opposite for BFO case is true.

Figure 4.2: Atomic force microscope (AFM) images of the STO and LSMO. **(a)** As-received STO substrate with mixed SrO and TiO_2 terminations explained in the inset. **(b)** DI water leaching yields a step-terraced structure with the miscut direction pointed by the white arrow. **(c)** LSMO grown on top of the treated STO substrate copying its morphology.

Figure 4.3: Topography of BFO thin films. **(a)** Atomic force microscope of thickness-variable BFO grown on LSMO/4STO. **(b)** Schematic demonstrating the emergence of saw teeth morphology on the BFO film due to the growth of single structural variant r_1 induced by the miscut in the STO substrate. **(c)** AFM image taken at the step between LSMO and BFO layers (top image). The profile curve revealed thickness of 70 nm is plotted in bottom image.

Figure 4.4: Piezoresponse force microscopy (PFM) studies exemplified by the 500 nm BFO/LSMO/4STO sample. **(a)** Lateral PFM phase image of size $4 \times 4\ \mu m^2$ showing the in-plane polarization pointing to $[110]_{pc}$ throughout the measured area. **(b)** Vertical PFM phase image of the same spot with upward out-of-plane polarization component **(c)** Illustration of the measurement set up where the cantilever is aligned along [-110]. Vertical polarization switching is implemented by applying +10 V to the tip yielding phase image **(d)** and amplitude image **(e)**. **(f)** Side view of the samples and the coloring code used in vertical PFM images.

Figure 4.5: High resolution x-ray diffraction patterns of the thickness-dependent BFO series grown on 10 nm LSMO/4STO. **(a)** Symmetric 2θ-ω scan revealing phase purity of the BFO films. **(b)** Zoomed-in image around (002) peaks in which BFO peaks gradually shift to higher 2θ values. **(c)** Analysis of the out-of-plane lattice parameter indicates the strain release in BFO films by reducing the c_{pc} axis in thicker films.

Figure 4.6: Thickness-dependent macroscopic ferroelectric properties of BFO films. **(a)** The polarization-electric field hysteresis loops of the BFO capacitors with different thicknesses **(b)** Typical Janovec-Kay-Dunn coercive field law. The straight line is a least-squares fit yields scaling exponent of K = -0.66. The inset shows a slight increase in the remnant polarization in thinner films from 65 $\mu C/cm^2$ to 67 $\mu C/cm^2$.

Figure 4.7: Thickness-scaling of photovoltaic effects in BFO vertical capacitors. Current density - voltage J-V curves measured under light in the down- **(a)** and up- **(c)** ferroelectric polarization states. **(b)** Plot of the extracted values of the V_{OC} and I_{SC} as a function of the BFO thickness fitted as straight line and exponential decay, respectively. **(d)** Schematic of the device under test. The unpolarized white light is provided through the objective lens to the platinum pad.

Figure 4.8: Fits of the typical J-E0.5 curves of Pt/(240 nm) BFO/LSMO heterostructure at 300 K.

Figure 4.9: Light intensity response of the device performance. **(a)** J-V curves in up- and down-polarization states under different white light intensities. **(b)** Linear dependence of V_{OC} on logarithmic light intensity. Despite the linearity in both polarization orientations, the fitted lines' slopes are different which might be correlated with the interface band-bending.

Figure 4.10: Comparison of the PV behavior upon front- and back-irradiation of the transparent device. **(a)** Sketch of the setup for the testing device. BFO/LSMO bilayer is grown on top of a transparent STO substrate to allow light transmission. Both measuring configurations are in upstate which is defined by polarization arrow points to the Pt electrode. **(b)** A parallel shift of the (J-V) curves (indicated by the gray arrows) after illuminating through the transparent STO/LSMO.

Figure 4.11: Schematic representation of the polarization-modulated interface ferroelectric photovoltaic effect. The ferroelectric photovoltaic cell can be modelled as two back-to-back rectifying diodes. **(a)** Upward polarization state in which the bottom interface band-bending dominates the overall photovoltaic output. **(b)** Downward polarization induces a higher band-bending at the top interface. The electronic band structure is plotted to the left side of the stack. Dashed straight lines represent Fermi levels. E_{bi} is the built-in electric field due to the band-bending at $BiFeO_3$/metal interfaces.

Figure 4.12: Tuning the top metal/BFO interface in the vertical capacitors. **(a)** (P-V) loops of metal electrode/BFO/LSMO films showing progressive offset in the positive side of the loop **(b)** Light (J-V) curves for the BFO/LSMO heterostructures with different top electrodes.

Figure 4.13: (a) Correlation between the switchable V_{OC} against coercive field extracted from P-V and J-V plots. Dependence of extracted V_{OC} on **(b)** electronegativities, **(c)** work function and **(d)** oxidation free energies of the top electrode metals.

Figure 4.14: Electrical measurements of BFO/LSMO heterostructures in dark at room temperature. **(a)** J-V curves collected in dark. **(b)** Schottky plots.

Figure 5.1: Illustration of the orientation of $BiFeO_3$-based photovoltaic cell with respect to the light polarization. In **(a)** Incoming white light propagates along z-direction through an objective lens before being linearly polarized by Glan-Thomson calcite-type polarizer. The sample is being rotated to the targeted azimuthal angle θ. Additionally, the in-plane ferroelectric polarization, along $[110]_{pc}$, is taken as a reference such that $\theta=0^o$ at which light polarization is parallel to the in-plane ferroelectric polarization **(b)**.

Figure 5.2: Modulation of photovoltaic performance in vertical $BiFeO_3$ heterostructures with light polarization. **(a)** Sinusoidal signal of the short-circuit current (black) and open-circuit voltage (blue) in 120-BFO sample in up-polarization state. **(b)** Normalized I_{SC} versus polarization angle in the same sample measured in up- (black) and down (red) ferroelectric polarizations. **(c)** Normalized I_{SC} in 500-BFO sample measured in up- and down ferroelectric polarization. **(d)** Tuning the crystal symmetry of BFO via lanthanum doping led to notable change in the modulation behavior in I_{SC}.

Figure 5.3: Calculated out-of-plane bulk photocurrent in monodomain (001)-oriented $BiFeO_3$ at different azimuthal angles in up- ferroelectric polarization state. The calculations were carried out for 405 nm (3.1eV) and 520 nm (2.4 eV) wavelengths. The generated photocurrents under both lights are in phase with different amplitudes.

Figure 5.4: Absorption coefficients of 170 nm $BiFeO_3$ **(a)** and $Bi_{0.8}La_{0.2}FeO_3$ **(b)** grown on transparent $SrTiO_3$ and measured by UV-vis spectrophotometer.

Figure 5.5: Polarized absorption spectra of $BiFeO_3$ **(a)** and $Bi_{0.8}La_{0.2}FeO_3$ **(b)** thin films. The absorption spectra were collected from -90° to 90°.

Figure 5.6: Tauc plots indicating the direct and indirect bandgaps for $BiFeO_3$ **(a)** and **(b)** and $Bi_{0.8}La_{0.2}FeO_3$ **(c)** and **(d)**. The extracted bandgaps show the same value for the two orthogonal directions in both samples.

Figure 5.7: Anisotropic light absorption in $BiFeO_3$ and $Bi_{0.8}La_{0.2}FeO_3$. **(a)** Wavelength-dependent percentage of deviation in light absorption between two orthogonal light polarizations. **(b)** Normalized integrated areas under the absorption curves from 400 nm to 600 nm as a function of the polarization angle. **(c)** Schematic illustrating the anisotropy in absorption in $BiFeO_3$ unit cell.

Figure 5.8: Photovoltaic output under monochromatic light compared to white light. Light current density-voltage in **(a)** Down polarization state and **(b)** Up polarization state.

Figure 5.9: Angular dependence of the photocurrents in Pt/BFO/LSMO. **(a)** Short-circuit current under 520 nm illumination in down ferroelectric polarization state. **(b)** I_{SC} under 405 nm illumination in down polarization state. Short-circuit current in up polarization state in illuminated 520 nm **(c)** and 405 nm **(d)** conditions.

Figure 5.10: Normalized anisotropic absorption in $BiFeO_3$ film as a function of polarization angle at 520 nm **(a)** and 405 nm **(b)** wavelengths. The data are extracted from polarization-dependent absorption curves.

Figure 5.1: Depiction illustrates the origin of interface- and bulk-induced photovoltaic effects in vertical capacitor based on $BiFeO_3$. **(a)** In-gap photon energy produce photovoltaic response originating from the band-bending at BFO/metal interface.

Illuminated by 520 nm laser, generated self-trapped exciton in the bulk of BFO which travel to the interface before being separated by Schottky barrier. **(b)** Above-bandgap illumination (405 nm) preferentially generates bulk photovoltaic effects in up ferroelectric polarization state with the interface effect still present. However, in down-state, the interface band-bending comes to the picture again since the top interface is activated and directly exposed to the illuminating light.

Figure 6.1: Summary of the findings in this PhD dissertation. This dissertation researches the photovoltaic mechanism in vertical $BiFeO_3$ heterostructures. Adopting white light yields photovoltaic output dominated by the interface band-bending at the $BiFeO_3$/metal. Three experimental strategies were designed including thickness-dependent PV, upside-down illumination and tuning the top electrode material. In addition, noble metals are recommended to be used with $BiFeO_3$ for maximized performance. Exploiting linearly polarized lights confirms the hypothesis that interface band-bending dominates the overall output by illuminating the cell by white light. In contrast, above-bandgap illumination gave rise to bulk photovoltaic action in which the interface PV still presents.

Figure 6.2: Topography and PFM images of Bi_2FeCrO_6 thin films. Topography of BFCO grown in mixed oxygen/argon 1Pa/0Pa **(a)**, 1Pa/6Pa **(b)** and 1Pa/9Pa **(c)**. In-plane PFM phase signal at oxygen/argon 1Pa/0Pa **(d)**, 1Pa/6Pa **(e)** and 1Pa/9Pa **(f)**.

Figure 6.3: X-ray diffraction results of the samples series. **(a)** Symmetric 2θ-ω scan around (003) peak. **(b)** Asymmetric 2θ-ω scan around (222) peak.

Figure 6.4: Direct bandgap of the BFCO series. **(a)** Direct bandgap plot. **(b)** Extracted bandgap values.

Abbreviations

SQ	Shockley-Queisser limit
BPVE	Bulk Photovoltaic effect
BFO	Bismuth Ferrite ($BiFeO_3$)
BFCO	Bi_2FeCrO_6
LSMO	$La_{0.7}Sr_{0.3}MnO_3$
Pt	Platinum
DW	Domain wall
CT	Charge Transfer
J_{sc}	Short-Circuit current density
J_{sc}^{Up}	Short-Circuit current density in up polarization state
J_{sc}^{Down}	Short-Circuit current density in down polarization state
V_{oc}	Open-Circuit Voltage
V_{oc}^{Up}	Open-Circuit Voltage in up polarization state
V_{oc}^{Down}	Open-Circuit Voltage in down polarization state
IP	In-Plane
OOP	Out-Of-Plane
PLD	Pulsed Laser Deposition
HRXRD	High Resolution X-ray Diffraction
AFM	Atomic force microscope
PFM	Piezoresponse force microscopy

Chapter 1

Introduction

This chapter familiarizes the reader with the nature of this doctoral thesis. It begins with the motive behind this experimental work which is driven by the lack of understating of the origin of the photovoltaic response measured in ferroelectric capacitors. This is followed by presenting the research problem and hypothesis tested. Also, the thesis organization is offered while the last section summarizes the original findings and outcomes of this thesis.

1.1 An alternative route for solar energy conversion

Solar energy is an abundant, clean and sustainable energy source in which, unfortunately, a tiny amount is exploited by the humankind. Sunlight converts into three different energy forms, namely electric energy, heat and chemical fuels.[1-3] *Photovoltaics* are the devices which directly convert the sunlight into electricity and one of the promising solutions to meet the global energy demand. Conventionally, the built-in electric field at p-n junction is exploited to separate electron-hole pairs producing a sizable photocurrent and hence a photovoltage.[4] However, in terms of efficiencies, these traditional p-n solar cells can only produce low light-to-electricity efficiencies.[5] Much effort has been devoted in order to improve the solar cells efficiencies which, unfortunately, will come to an end following the fundamental limit predicted by Shockley-Queisser (SQ) model in 1961. The model predicted efficiency up to 33.7% for a semiconductor with bandgap 1.34 eV in single layer solar cells.[6,7] Consequently, more efficient conversion of the solar energy into electricity is one of the challenging tasks that face mankind which, in turn, grows the need to look for alternatives.

Solar cells based on *bulk photovoltaic effect* are one of the proposed alternatives to exceed the SQ limit. Such devices take the advantage of the noncentrosymmetry of polar crystals to separate the photoexcited charge carries before making their way to the electrodes. This implies that photocurrent is generated in the bulk of the active layer and above-bandgap-photovoltages can be achieved.[8-12] Additionally, the complication of the cell fabrication is avoided since such device requires a solo active layer. The comparison between the conventional and bulk photovoltaics is introduced in Figure 1.1.

Particularly, ferroelectrics are materials that can fulfill this condition, i.e., the noncentrosymmetry which is manifested by the spontaneous electric polarization. One of the characteristic aspects of the bulk photovoltaics over the conventional barrier solar cells is the switchable polarization giving rise to “bipolar” solar cells. More interestingly, Schottky diodes are known to form at the ferroelectric/metal electrodes and can provide additional charge separation platform.[13-15] This implies that bulk and interface effects might

coexist in the ferroelectric solar cells. Hence, understanding of the ferroelectric photovoltaic effects is vital from both the fundamental and technological perspectives. Fundamentally, it is central to the field to give deeper insights on the physics of light-matter interaction. On the technological perspective, deducing the origins of the ferroelectric photovoltaic helps to boost the overall efficiency.

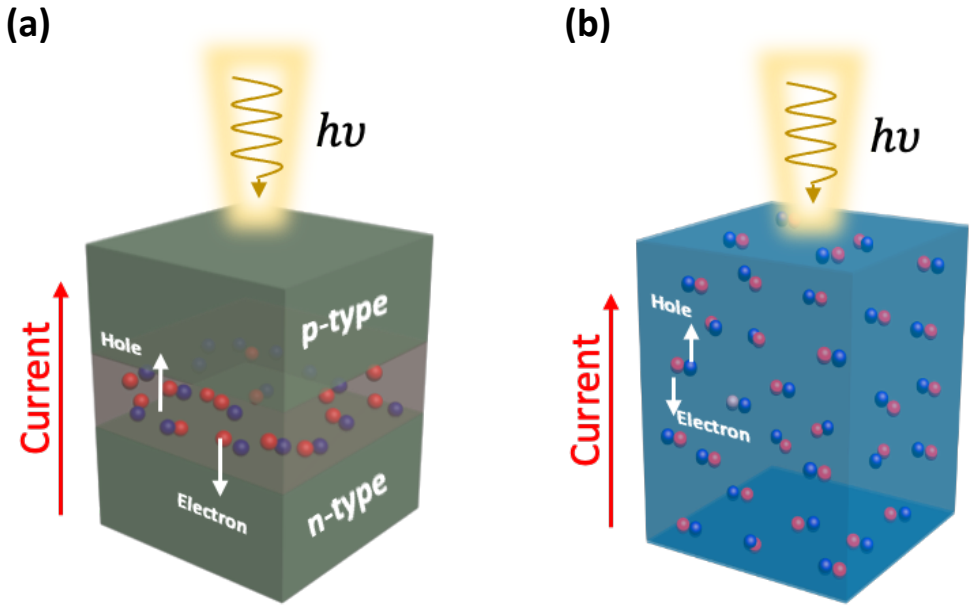

Figure 1.1: Concept of light-to-electricity conversion in two types of solar cells. **(a)** Conventional solar cell. In this type of solar cells, photoexcited electron-hole pairs are separated by the electric field at the p-n junctions (usually, doped silicon). **(b)** Bulk photovoltaic cell. Here, charge carriers are separated throughout the whole bulk of spatially homogeneous material and hence given the term (bulk). The driving mechanism of the charge separation in bulk PVs is the crystal asymmetry. Therefore, crystals lacking the center of symmetry are (natural) solar cells.

The general motivation behind this study is to understand better the photovoltaic mechanisms in vertical ferroelectric heterostructures. That is, the photovoltaic cell consisting of ferroelectric layer sandwiched between two metallic electrodes. For this, the prototypical photoferroelectric, bismuth ferrite ($BiFeO_3$), is adopted in this work due to its unique combined ferroelectric and optical properties over the classical ferroelectrics such as $LiNbO_3$[16], $BaTiO_3$[17] and $Pb(Zr,Ti)O_3$[18].

1.2 Problem Statement and hypothesis

Despite the bright potential of the ferroelectric photovoltaic effect, they still suffer from issues that prevent their application. Photovoltaic effect exhibits three consecutive fundamental processes, i.e., light absorption, electron-hole separation and charge carriers transport. Broadly, ferroelectrics, as wide bandgap insulators, suffer from low light absorption and poor charge transport. Further, the driving mechanism of the photovoltaic response is still unclear. The former problems are beyond the scope of this dissertation whereas attention is focused on the origination of the charge carrier separation in ferroelectrics.

The origin of the ferroelectric photovoltaic effect in $BiFeO_3$ has been under a contentious debate since the discovery of switchable behavior in 2009[19]. Several mechanisms have been proposed based on both experimental and theoretical investigations to explain such intriguing behavior. One side supports the idea that the ferroelectric polarization in the homogeneous bulk of the crystal gives rise to bulk photovoltaic effects. The opposing side admits that the interface band-bending at the ferroelectric/metal interface dominates the overall photovoltaic response. Indeed, it is usually challenging to deduce which of the stimuli is actually contributing more/less to the total measured PV behavior.

However, building a ferroelectric PV device with lateral configuration would exclude the interface-driven mechanism. In contrary, the photovoltaic effects in thin films sandwiched between two electrodes is more complicated since the aforementioned proposed mechanisms can be strongly interlaced. Consequently, it is of high importance to disentangle these photovoltaic mechanisms to unlock the full potential of the ferroelectric photovoltaic effect.

The central question in this dissertation is to test whether or not the bulk and interface ferroelectric photovoltaic mechanisms coexist in vertical $BiFeO_3$ thin film heterostructures. This leads to the question that whether, if any, they cooperate, compete or even dominate the overall photovoltaic response. Both qualitative and quantitative approaches are used in

this dissertation to investigate the impact and relative contributions of the different mechanisms. Addressing such research question could assist in exploiting the full potential of bulk photovoltaic cells.

1.3 Objectives and Scope

The main objective of this dissertation is to develop an understanding of the ferroelectric photovoltaic mechanism in bismuth ferrite $BiFeO_3$ thin films. The focus is paid to the vertical capacitors comprising thin active layer and small sizes. Consequently, different experimental strategies concerning both the exciting radiation and the construction of the devices under test are designed to identify the factors deciding the total photovoltaic behavior in the cell.

In this regard, solar cells based on high quality single crystalline $BiFeO_3$ are prepared by means of physical vapor deposition methods. White light and monochromatic laser sources exhibiting either unpolarized or linearly polarized nature are adopted to excite the heterostructures. On the other hand, the thickness of the active layer, electrodes and device sizes are systematically tuned. Also, the ferroelectric structure of $BiFeO_3$ thin films is tailored through the rare-earth element (Lanthanum) doping with the aim to investigate the ferroelectric photovoltaic output.

1.4 Dissertation Overview

This dissertation is composed of six chapters including this introductory chapter. The detailed scheme is presented as follows.

In this chapter, *Chapter 1*, begins with the motivation behind this research. Also, the rationale for the research, the goals and scope are provided.

The Second Chapter entitled the literature review recalls the basics and history of the photoferroelectrics and ferroelectric photovoltaic effect. A special attention is given to the

ferroelectric and optical properties of bismuth ferrite as the photoactive layer exploited throughout this work. This is followed by giving an overview of the literature concerning the ferroelectric photovoltaic effects.

Chapter 3 is concerned with the methodology used for this study. For this, the principles underlying the material synthesis device fabrication techniques employed are detailed. Afterwards, the structural, ferroelectric and photovoltaic characterization of the prepared devices are elaborated.

Chapter 4 investigates the photovoltaic effects in devices based on thickness variable $BiFeO_3$ layers. Additionally, the top electrode material is tuned to elaborate the role of Schottky interface on the overall photovoltaic response.

Chapter 5 utilize a different strategy to further explore and analyze the origin of the photovoltaic response in $BiFeO_3$ heterostructures. In this chapter, linearly polarized light sources are exploited to characterize the devices while maintaining the film thickness and top electrode fixed.

In *Chapter 6*, a summary of this research is provided. Eventually, a different perspective on how to improve the ferroelectric photovoltaic effects in ferroelectric-based solar cells are laid out.

1.5 Findings and Outcomes/Originality

In this doctoral dissertation, the origin of ferroelectric photovoltaic effects in vertical stacked configurations based on the prototypical ferroelectric $BiFeO_3$ is explored. This research led to several novel outcomes as follows:

1. Endorsement of the interface band-bending as a platform for the separation of the charge carriers upon white light illumination.
2. Linearly polarized undergoes anisotropic absorption when light incident on (001)-

oriented monodomain $BiFeO_3$.

3. By adopting linearly polarized lights, the bulk and interface photovoltaic mechanisms can be distinguished leading to:
    - Illuminated by above-bandgap light, 3.1 eV laser, bulk photovoltaic mechanism dominates the overall output. A theoretical model is introduced to explain the experimental results. However, the interface band bending mechanism still exists.
    - The interface band-bending-driven photovoltaic effects dominates if the device shined by in-gap (2.4 eV) laser or white light. In this case, the anisotropic absorption was taken as a reference to distinguish Schottky photovoltaic effects.

References

1. Crabtree, G. W. & Lewis, N. S. Solar energy conversion. *Physics Today* **60**, 37-42, doi:10.1063/1.2718755 (2007).

2. Neville, R. *Solar Energy Conversion*. (ELSEVIER, 1995).

3. Yuan, Y., Xiao, Z., Yang, B. & Huang, J. Arising applications of ferroelectric materials in photovoltaic devices. *J. Mater. Chem. A* **2**, 6027-6041, doi:10.1039/c3ta14188h (2014).

4. Chapin, D. M., Fuller, C. & Pearson, G. A new silicon p-n junction photocell for converting solar radiation into electrical power. *Journal of Applied Physics* **25**, 676-677 (1954).

5. Würfel, P., ; Würfel, U. *Physics of Solar Cells: From Basic Principles to Advanced Concepts*. 3rd edn, (2016).

6. Mathers, C. D. Upper limit of efficiency for photovoltaic solar cells. *Journal of Applied Physics* **48**, 3181-3182, doi:10.1063/1.324059 (1977).

7. Shockley, W. & Queisser, H. J. Detailed Balance Limit of Efficiency of p-n Junction Solar Cells. *Journal of Applied Physics* **32**, 510-519, doi:10.1063/1.1736034 (1961).

8. Fridkin, V. *Photoferroelectrics*. (Springer-Verlag Berlin Heidelberg New York, 1979).

9. Kim, D. J. & Alexe, M. Bulk photovoltaic effect in monodomain $BiFeO_3$ thin films. *Applied Physics Letters* **110**, doi:10.1063/1.4983032 (2017).

10. Bhatnagar, A., Roy Chaudhuri, A., Heon Kim, Y., Hesse, D. & Alexe, M. Role of domain walls in the abnormal photovoltaic effect in $BiFeO_3$. *Nature Communications* **4**, doi:10.1038/ncomms3835 (2013).

11. Matsuo, H. *et al.* Bulk and domain-wall effects in ferroelectric photovoltaics. *Physical Review B* **94**, doi:10.1103/PhysRevB.94.214111 (2016).

12. Matsuo, H., Noguchi, Y. & Miyayama, M. Gap-state engineering of visible-light-active ferroelectrics for photovoltaic applications. *Nat Commun* **8**, 207, doi:10.1038/s41467-017-00245-9 (2017).

13. Blom, P. W., Wolf, R. M., Cillessen, J. F. & Krijn, M. P. Ferroelectric Schottky diode. *Phys Rev Lett* **73**, 2107-2110, doi:10.1103/PhysRevLett.73.2107 (1994).

14. Pintilie, L. & Alexe, M. Metal-ferroelectric-metal heterostructures with Schottky contacts. I. Influence of the ferroelectric properties. *Journal of Applied Physics* **98**, doi:10.1063/1.2148622 (2005).

15. Pintilie, L. *et al.* Metal-ferroelectric-metal structures with Schottky contacts. II. Analysis of the experimental current-voltage and capacitance-voltage characteristics of $Pb(Zr,Ti)O_3$ thin films. *Journal of Applied Physics* **98**, doi:10.1063/1.2148623 (2005).

16. Redfield, D. & Burke, W. J. Optical absorption edge of LiNbO3. *Journal of Applied Physics* **45**, 4566-4571, doi:10.1063/1.1663089 (1974).

17. Wemple, S. H. Polarization Fluctuations and the Optical-Absorption Edge in $BaTiO_3$. *Physical Review B* **2**, 2679-2689, doi:10.1103/PhysRevB.2.2679 (1970).

18. Kholkin, A., Boiarkine, O. & Setter, N. Transient photocurrents in lead zirconate titanate thin films. *Applied Physics Letters* **72**, 130-132, doi:10.1063/1.120663 (1998).

19. Choi, T., Lee, S., Choi, Y. J., Kiryukhin, V. & Cheong, S.-W. Switchable Ferroelectric Diode and Photovoltaic Effect in $BiFeO_3$. *Science* **324**, 63-66, doi:10.1126/science.1168636 (2009).

Chapter 2

Literature Review

This chapter introduces the theoretical background and synopsis of the literature of the phenomenon researched in this work, the ferroelectric photovoltaic effect. It starts with giving an overview of the physics of the ferroelectricity. The material system investigated here, $BiFeO_3$, is detailed by describing its crystal structure, ferroelectricity and optical properties. This is accompanied by the comparison between the ferroelectric photovoltaic effect to the conventional solar cells. Finally, a brief history and the literature review regarding the photovoltaic effects in ferroelectrics is comprehensively introduced.

2.1 Ferroelectricity

2.1.1 History and definition

Ferroelectricity was discovered by Valasek in 1920[1] in rochelle salt while studying its dielectric properties. He found that the material exhibits bi-stable dielectric states by applying an electric field in two opposite directions similar to the loop shown in Figure 2.1. Consequently, a resemblance between this behavior and the hysteretic behavior of the ferromagnetism in iron was concluded (and hence the name "*ferro*" although rochelle salt does not contain iron). The field of ferroelectricity was flourished after the discovery of the ferroelectric perovskite with ABO_3 chemical formula, $BaTiO_3$, in 1944[2]. This marked the emergence of the perovskite era with robust and strong ferroelectricity such as $Pb(Ti,Zr)O_3$[3], $LiTiO_3$[4], $LiNbO_3$[4] and eventually $BiFeO_3$[5]. This also opened the door to use ferroelectric materials for diverse applications such as actuators, non-volatile memories and energy harvesting devices.[6]

Ferroelectrics are those materials that possess spontaneous polarization driven by a relative displacement of the charged ions. The *spontaneous polarization*, defined as the sum of the dipole moments per unit volume (C/cm^2), can be manipulated in to at least two stable states by external electric field. Most importantly, ferroelectrics must be insulators so that the manipulating electric field is applied solely to the lattice ions (unlike the free charges in case of metals or semiconductors). Furthermore, and at ground state, ferroelectric material can break into small regions with different polarization orientations called ferroelectric *domains*. Another important property of ferroelectrics is the ferroelectric-paraelectric phase transition. Accordingly, there exists a critical temperature, *Curie point* Θ_c, below which the material stays in ferroelectric state. Above Θ_c, the crystal is in a non-polarized state called *paraelectric* phase.[7-9]

Figure 2.1 depicts a typical polarization (P)-electric field (E) hysteresis loop of $BaTiO_3$ ceramic. Upon exceeding a certain value, called *coercive electric field* E_c, the material's polarization is to align itself parallel to the electric field before reaching a *saturation* value

called P_s. Applying electric field in opposite direction above -E_c reverses the polarization. As the plot indicates, even at null electric field, the material is still in polarized state.

Crystal structure-wise, ferroelectric materials are characterized by the lack of center of

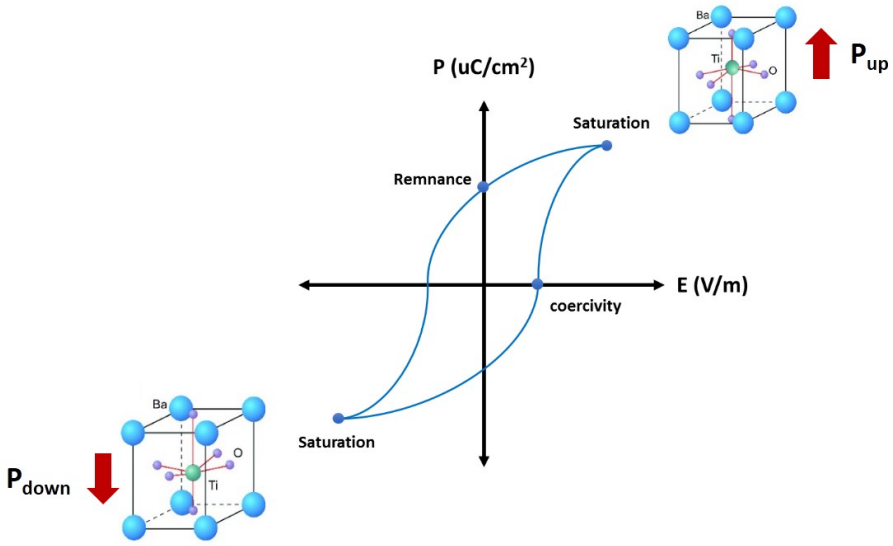

Figure 2.1: Typical polarization-electric field loop of the $BaTiO_3$ ceramic. Ferroelectricity stems from the relative shift of the Ti^{3+} ion in the oxygen octahedron to either up or down with respect to the initial position in perfect perovskites. However, applying an electric field above the coercive field $\mp E_c$ can switch the Ti cation between the two positions.

symmetry (inversion center). Noncentrosymmetric crystals comprise 21 crystallographic point groups out of 32 in total. All the noncentrosymmetric point groups exhibit *piezoelectric effect*, or the accumulation of surface charges upon applying mechanical stresses, except the 432 point group. More specifically, 10 point groups are *pyroelectrics* - those substances possessing non-switchable polar axis (in variance with ferroelectrics). Clearly, ferroelectrics are subgroup of pyroelectrics. In other words, ferroelectric materials respond to external stimuli such as electric fields, stresses, heating and light allowing a wide spectrum of functionalities.[10,11] Piezoelectric effect can be represented by the equation[12,13]:

$$D = dX \tag{2.1}$$

where D is the charge density, X is the applied mechanical stress and d is piezoelectric coefficient which is material-characteristic. However, a more proper way to express the

physical properties of crystals is by using the tensor notation to formulate the linear relationships. Accordingly, equation (2.1) can be reformulated as[12,13]:

$$D_i = d_{ijk} X_{jk} \tag{2.2}$$

Where d_{ijk} is third-rank tensor and depends on the crystal symmetry following Neumann's principle. The general rule here is simple, since the displacement is a vector (or a first rank tensor) and the stress is a second-rank tensor, hence the piezoelectric coefficient is of 3rd rank.[13]

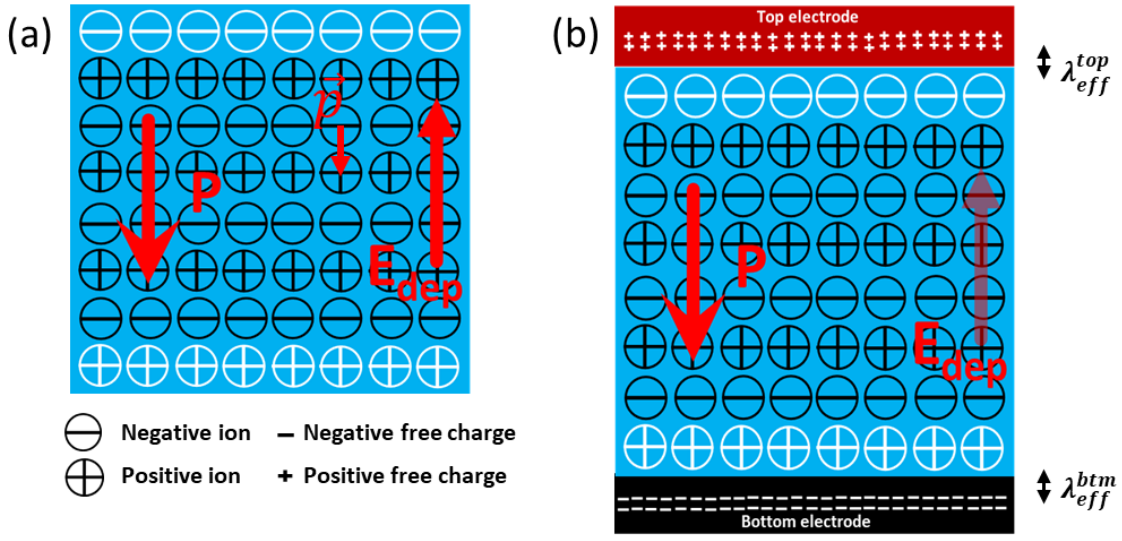

Figure 2.2: Electrostatic description of ferroelectrics. **(a)** Freestanding ferroelectric layer with a developed depolarization field E_{dep} opposite to the polarization direction P. **(b)** The polarization is screened by the free charges in metallic electrodes in contact with it leading to a weakened E_{dep}.

Ferroelectric materials can be modelled by the simplified picture of a typical ferroelectric capacitor in Figure 2.2. As the plots demonstrate, the electric dipole moments are oriented in direction yielding a resultant macroscopic polarization (pointing from negatively charged ions to the positive ones). Consequently, an opposing *depolarization field* E_{dep} is necessary to maintain the crystal in an equipotential state. For the purpose of electrical measurements, metallic electrodes are brought in contact with the ferroelectric layer. This allows *screening* of the polarization charges at both surfaces and hence a weakened depolarization field, although not totally suppressed. However, thinning the ferroelectric layer re-enhances the depolarization field and might suppresses the ferroelectricity in

ultrathin films. The screening efficiency depends on how far the compensating charges are located from the ferroelectric/metal interface, or the *screening length* given by[7]:

$$E_{dep} = -2\frac{\lambda_{eff}}{d\epsilon_o}P \quad (2.3)$$

where λ_{eff} is the effective screening length, d is the ferroelectric layer thickness and ϵ_o is the free space permittivity.

2.1.2 Ferroelectric Schottky diodes

Semiconductors in contact with metallic electrodes form potential barrier which is usually of rectifying-, called *Schottky barrier,* or ohmic characteristics.[14] Depending on electron affinity of the semiconductor layer with respect to the work function of the metal, electrons jump from one side to the other to flatten the vacuum levels. As a consequence, the surface region becomes depleted (accumulated) leading to a bent band edge upward (downward) at the interface.

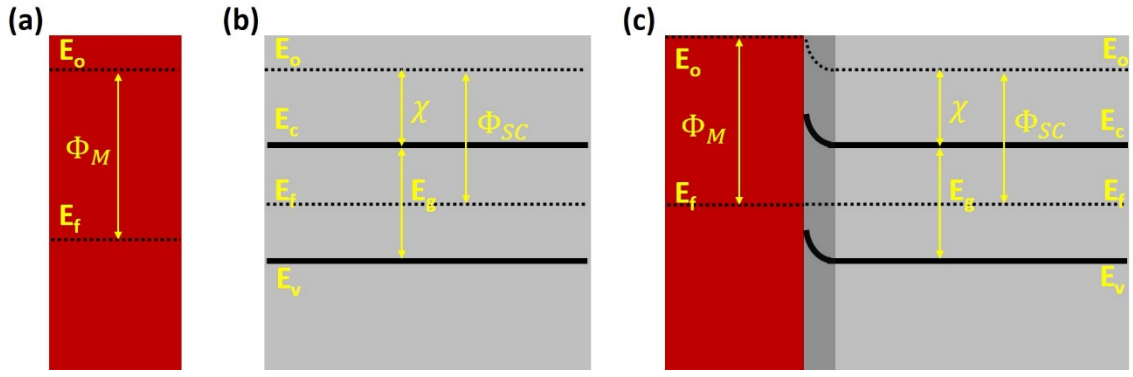

Figure 2.3: Schottky barrier at metal/semiconductor interface. The band diagram of free-standing metal **(a)** and intrinsic semiconductor **(b)**. **(c)** Band bending at the metal-semiconductor after charge reorganization. Inspired by (Ref. 15).

Figure 2.3 schematically presents an example of an ideal semiconductor/metal junction giving rise to Schottky barrier height (SBH) of[16]:

$$\Phi_{SBH} = \phi_M - \chi \quad (2.4)$$

where ϕ_M is the metal work function and χ is the semiconductor electron affinity. However, in reality, the doping level $|E_c - E_f|$ of the semiconducting material must be taken into consideration. This modifies equation (2.4) to[16]:

$$q\Phi_{SBH} = q(\phi_M - \chi) - |E_c - E_f| \quad (2.5)$$

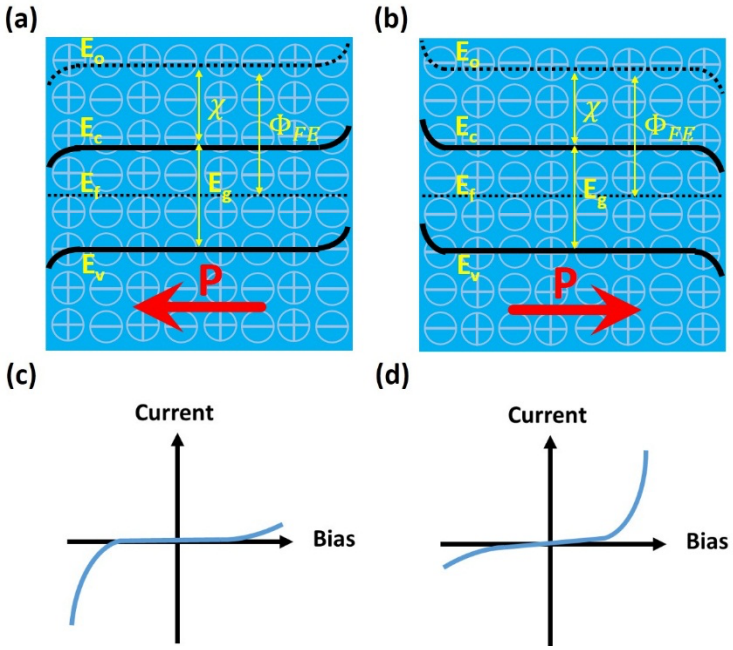

Figure 2.4: Band diagram representation of ferroelectric material in two possible polarization states. **(a)** and **(b)** The band edge curves down and up at the head and tail, respectively. Switchable conduction behavior of ferroelectrics in **(c)** and **(d)**. In fact, sandwiching a ferroelectric layer between two metal electrodes gives rise to back-to-back diode effects, or switchable diode effects.

On the other hand, free charges are pushed to the surfaces of free-standing ferroelectrics driven by the depolarization field. Figure 2.4 (a) shows the band structure of the ferroelectric material without applying metal electrodes. The band edge at the polarization tail (head) is curved up (down) in response to the charge carriers depletion (accumulation). Consequently, flipping the polarization alters the band bending to the opposite situation as depicted in Figure 2.4 (b). In this case, equation (2.5) to be modified to take into account the surface polarization charges. After introducing metal of work function ϕ_M to the ferroelectric surface, equation (2.5) can be written as[17]:

$$q\Phi_{SBH} = q(\phi_M - \phi_{FE}) \mp q\frac{P}{\varepsilon_o \varepsilon_r}\delta \quad (2.6)$$

Where P is the ferroelectric polarization, ϕ_{FE} is the work function of the ferroelectric layer and ε_r is its dielectric constant. δ is the distance between the surface charges and electrode. It is obvious from equation (2.6) that the ferroelectric polarization induced a polarization-modulated Schottky barrier height at the interface. In other words, the polarization modulates Schottky barriers from depletion to accumulation states yielding a switchable diode effect as shown in Figure 2.4 (c) and (d).

It is worth to mention that Schottky barrier plays an important role in determining the properties of the ferroelectric-related behaviors. For instance, existence of a rectifying Schottky barrier at the interface introduces an additional voltage which affects the coercive field. Ferroelectrics with ohmic junctions show reduced coercive fields and improved retentions than that with Schottky interfaces.[18] More intriguingly, it is believed that Schottky barriers contributes to the photoinduced effects in ferroelectrics as will be discussed later.

2.2 Introduction to Bismuth Ferrite ($BiFeO_3$)

Bismuth ferrite, or *$BiFeO_3$*, is almost certainly the only room-temperature *multiferroic* single phase material. In other words, it exhibits a simultaneous ferroelectricity, antiferromagnetism and ferroelasticity and hence described by the term "multiferroic". Intriguingly, the three orders are coupled in $BiFeO_3$ due to its distinct crystal structure. Alongside with the multiferroicity, BFO exhibits complex photoinduced phenomena such as photovoltaic effect[19] and photostriction[20] that reflects its interesting optical-ferroelectric coupling. Consequently, $BiFeO_3$ has become an interesting playground to study the fundamental aspects of the ferroic orders and the interplay among them.[21-24] The goal of this section is to introduce the different physical properties of $BiFeO_3$ with special focus on the ferroelectric and optical aspects.

2.2.1 Crystal structure

Bismuth ferrite belongs to the family of perovskite oxides. Figure 2.5 depicts the crystallographic unit cell of the bulk $BiFeO_3$ as determined in 1971[25] after its discovery in late 1950s by Royan and Swars.[26] $BiFeO_3$ unit cell is characterized by two distorted perovskite units forming a rhombohedral block (black frame). The two blocks are connected along their diagonal, i.e. $[111]_{pc}$. Moreover, one oxygen octahedron is rotated clockwise while the other one is tilted anticlockwise around the $[111]_{pc}$ direction by an angle of 13.8° with the Fe^{3+} ion shifted by 0.135 Å along the same axis.[27] This displaces the Bi^{3+} ion from its position giving rise to the rhombohedral distortion with angle of 89.45°. The lattice parameters of the rhombohedral unit cell of $BiFeO_3$ were calculated to be a_{pc} = 3.965 Å where (pc) refers to the pseudocubic notation.[25] In terms of crystal symmetry, bulk $BiFeO_3$ crystallizes in the rhombohedral space group R3c.

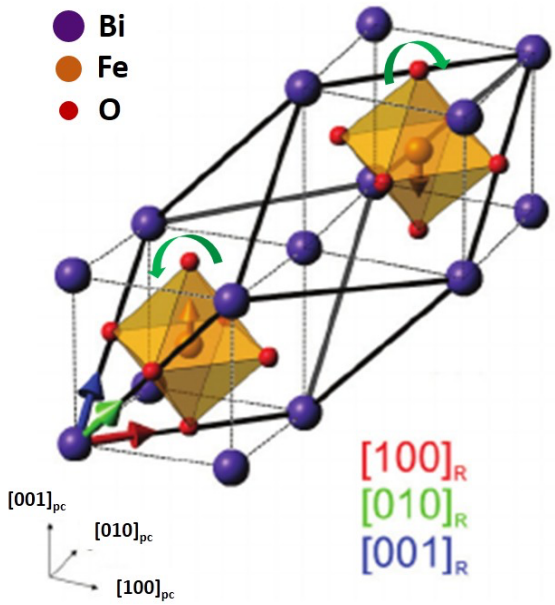

Figure 2.5: Depiction illustrates the construction of the unit cell of $BiFeO_3$ crystal. It is characterized by two distorted perovskite unit cells leading to a rhombohedral unit. However, the structure can be simplified by describing it in terms of pseudocubic (pc) notation. In pseudocubic notation, the two oxygen octahedra are tilted in opposite directions with respect to $[111]_{pc}$ direction. In addition, the spins at the Fe^{3+} sites couple antiferromagnetically. The pseudocubic and rhombohedral axes are given in the inset images. Adapted from ref. 28.

However, $BiFeO_3$ crystal structure can be controlled through epitaxial strain induced by a single crystal substrate (this contrasts with $BiFeO_3$ single crystals that show rhombohedral structure). In other words, $BiFeO_3$ exhibits various crystal structures spanning from orthorhombic[29,30], rhombohedral[31-33] to tetragonal[34-36] phases. For example, bismuth ferrite films grown on the perovskite $LaAlO_3$ substrate either show a tetragonal phase or mixed tetragonal and rhombohedral phases depending on the film thickness.[36] $NdScO_3$ substrates possess orthorhombic phase with in-plane lattice parameters comparable to that of $BiFeO_3$ if grown on $(110)_{pc}$ orientation. Interestingly, the former substrate can be used to obtain orthorhombic structure with the total polarization along $[110]_{pc}$ direction.[29] Also, rhombohedral $BiFeO_3$ phase is stabilized when thin film is grown coherently and after relaxation.

2.2.2 Ferroelectric property and domain structure

Unlike the conventional ferroelectrics such as $BaTiO_3$ and $PbTiO_3$, ferroelectricity in bismuth ferrite is caused by the relative displacement of the Bi^{3+} ions along $[111]_{pc}$ axis.[37] The ferroelectric mechanism explained a follows. The Bi^{3+} cation in $BiFeO_3$ possesses lone pair in its 6s orbital which is (stereo)chemically active[38] in which they do not participate in in any chemical bonding.[39] Further, the lone pair electrons hybridize with the 2p orbital in the O^{2-} anion shifting Bi^{3+} cations off center and stabilizing the rhombohedral phase. The movement of the Bi^{3+}, and accordingly Fe^{3+}, in either positive or negative directions lead to two possible polarization states which can be controlled via external electric field.[37]

In 2003[40], $BiFeO_3$ was rediscovered when Wang *et al.* have grown a high quality epitaxial thin films with unexpectedly large remnant polarization of 60 $\mu C/cm^2$ along $[001]_{pc}$ direction. This is around one order of magnitude larger than what has been reported[5] in first study of polarization hysteresis loop of $BiFeO_3$ (6.1 $\mu C/cm^2$). Since then, much interest in the field of ferroelectrics has been renewed yielding growth of high-quality $BiFeO_3$ in all its forms, i.e., thin film, single crystal and ceramic. Figure 2.6 (a) and (b) present the PE hysteresis loops of $BiFeO_3$ in epitaxial thin film and single crystal forms, respectively.

When strain-free $BiFeO_3$ is epitaxially grown, eight structural variants are likely to exist in the film to release their electrostatic energy.[41] Since the total polarization points towards $<111>_{pc}$, three types of domain boundaries are predicted to exist in $BiFeO_3$, namely, 71°, 109° and 180°, separating the adjacent structural variants. These numbers refer to the domain walls and imply the magnitude of the angles between the neighboring polarizations.[42,43] As shown in figure, the different domains are notated by ($\pm r_1$-$\pm r_4$) where ± indicates whether the polarization is up or down. However, the domain architecture of $BiFeO_3$ can be engineered via controlling the mechanical and/or electrostatic boundary conditions. For instance, it is reliably established in the literature that $BiFeO_3$ grown on $SrRuO_3$[44] and $La_{0.7}Sr_{0.3}MnO_3$[31,33,45] develop downward and upward as-grown polarization states, respectively. This elucidates the role played by the type of conductivity of the bottom metallic electrode, i.e. *n- or p-type*.

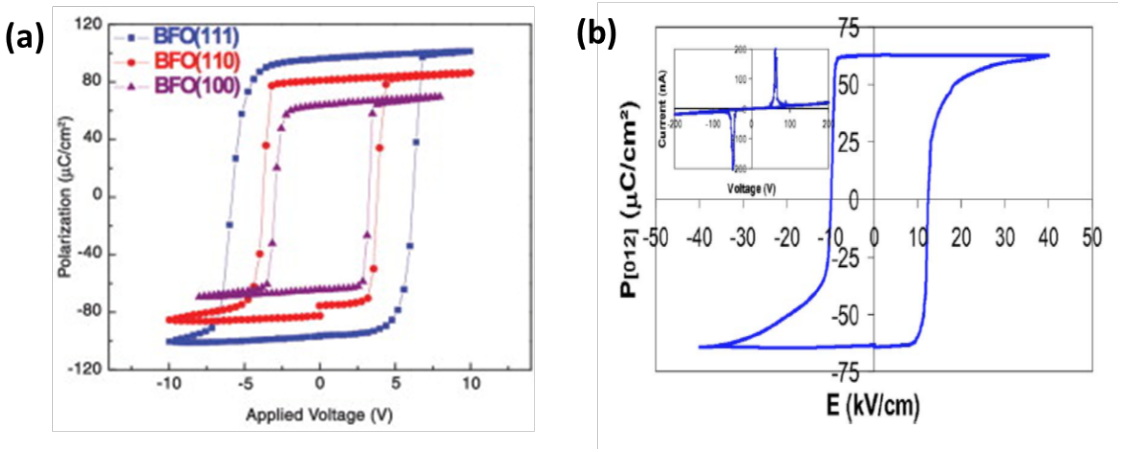

Figure 2.6: Polarization-electric field (PE) hysteresis loop of $BiFeO_3$. **(a)** PE loops of $BiFeO_3$ epitaxial films measured along three different orientations. Crystal orientation-dependent remnant polarization show evolution from 60 $\mu C/cm^2$ along $[001]_{pc}$ to 100 $\mu C/cm^2$ towards $[111]_{pc}$. **(b)** PE loop of single $BiFeO_3$ crystal demonstrating a rectangular loop. Taken from ref. 47.

Selective control of the domain configuration in $BiFeO_3$ is sometimes desirable in order to tailor its physical properties.[48] In $BiFeO_3$, the aforementioned domain walls are electrically conductive compared to the bulk of ferroelectric material. The origin of this behavior is attributed to the formed electrostatic potential step and reduction of the local bandgap at the domain walls.[49-51] Furthermore, the structural symmetry breaking in the domain wall

differs from the material's crystal structure offering more complexity to the fundamental aspects of $BiFeO_3$.[52]

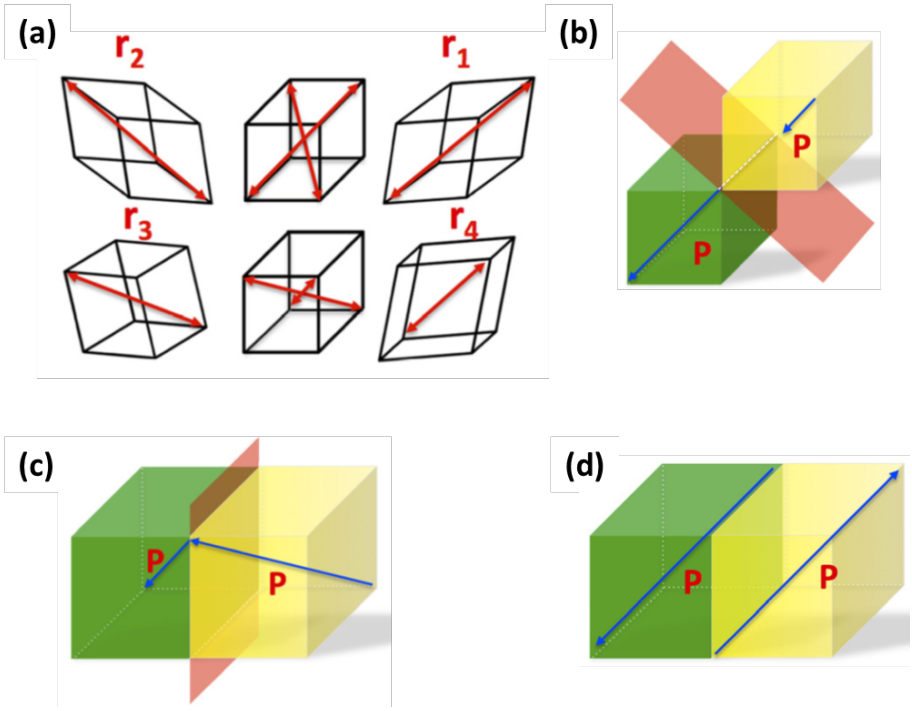

Figure 2.7: Ferroelectric domain structure of $BiFeO_3$. **(a)** Eight possible orientations of total polarization. Schematic of two-adjacent-domain configurations of $BiFeO_3$ leading to formation of **(b)** 71°, **(c)** 109° and **(d)** 180° domain walls. Taken from ref. 53.

2.2.3 Magnetic structure

In addition to the ferroelectricity, $BiFeO_3$ exhibits Fe^{3+} spin ordering creating G-type antiferromagnetism below T_N of 370 °C. In other words, Fe^{3+} ions can be thought as two sublattices that are coupled antiferromagnetically. Additionally, the spins at the Fe^{3+} ions are slightly canted due to the antiphase tilting of the oxygen octahedra demonstrated by the green arrows in Figure 2.5. This emerges a weak ferromagnetic ordering throughout the crystal with magnetization vector normal to the antiferromagnetic spin axis as plotted in Figure 2.8 (a).[54-56] Despite the fact that the ferroelectricity and antiferromagnetism in $BiFeO_3$ vanish at different temperature, and hence different origins, they are coupled

making $BiFeO_3$ such a promising material for magnetoelectric applications at room temperature.

Indeed, the macroscopic magnetization and the magnetoelectric coupling are cancelled. The reason is that the net moments induced by the spins canting form cycloidal waves with wavelength ~62 nm as measured by the neutron scattering experiments.[57-59] However, the cycloid can be suppressed by external knobs such as high magnetic fields[60,61]. Also, epitaxial strain is another way to kill the unfavorable cycloid in $BiFeO_3$[62-64] unlocking its potential for spintronics. For instance, Ching *et al.*[65] obtained a sizable magnetization in $BiFeO_3$ grown on $LaAlO_3$ substrates. The authors employed a thickness-dependent approach which led to a suppressed cycloid in the thinnest film (38 nm) highlighting the role of epitaxial strain.

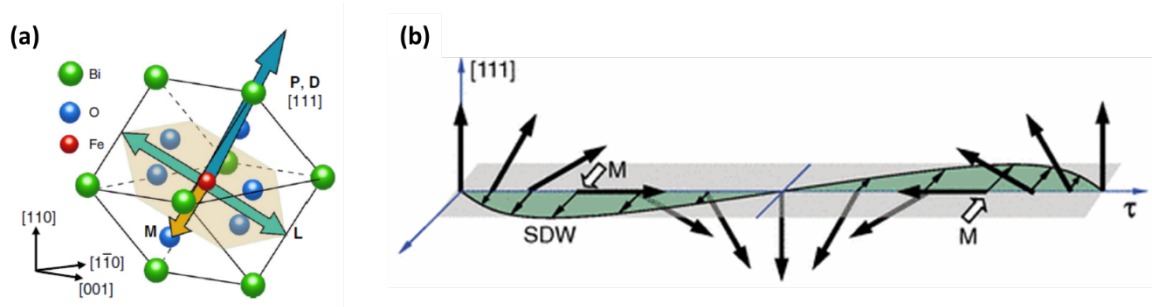

Figure 2.8: Magnetic structure of $BiFeO_3$. **(a)** Unit cell of $BiFeO_3$ with the antiferromagnetic axis L normal to the canted local moment M within the same plane and total ferroelectric polarization P perpendicular to the AFM plane.[67] **(b)** The spin cycloid forming sinusoidal wave propagating along $<110>_{pc}$ with wavelength ~62 nm.[66]

2.2.4 Electronic structure and optical properties

Bismuth ferrite belongs to the complex iron oxides in which Fe^{3+} is octahedrally surrounded by O^{2-} ions. In iron oxides, the valance band is constructed by the hybridized oxygen 2*p* and iron 3*d* states. On the other hand, the bottom of the conduction band is dominated by the Fe 3*d* states. The experimental bandgap values of the rhombohedral phase was determined to be from 2.6 to 2.8 eV[68-70] which are in good agreement with the theoretical calculations[71,72].

It is reliably established that $BiFeO_3$ is a charge transfer insulator (CT). Hence, explaining the optical structure of $BiFeO_3$ in terms of charge transfer transitions (CT) is more precise than the band picture. Focusing on the optical spectrum, the rhombohedral $BiFeO_3$ exhibits CT from oxygen 2*p* to iron 3*d* as well as *d-d* transitions between Fe 3*d* valence and conduction bands. The most noticeable transition features are the weak dipole-forbidden *p-d* CT (2.5 eV) and dipole-allowed *p-d* CT at 3 eV.[70,73]

$BiFeO_3$ has a uniaxial optical anisotropy which coincides on its polar axis, i.e., along $[111]_{pc}$. Consequently, high *birefringence* (that is, the difference in refractive indices of two different axes) was reported in BFO crystals.[74,75] Moreover, *linear dichroism* (or the anisotropic absorption under two different light polarizations) was also qualitatively determined in BFO films and crystals.[70,76,77] For $(001)_{pc}$-oriented crystal under linearly-polarized light, the absorbance is minimal along the in-plane polarization $[110]_{pc}$ and maximized along $[-110]_{pc}$ as determined by the ellipsometric measurements. However, no detailed quantitative study describing the linear dichroism in thin films was reported.

2.3 Photovoltaic effect

Photovoltaic effect is the generation of an electric current in semiconducting materials upon illuminating the material with a uniform light intensity. The illumination light with energy larger than the material bandgap promotes the charge carriers from the valence band (VB) to the conduction band (CB). Consequently, photovoltaic current is generated in short-circuit conditions I_{sc}. Moreover, a photovoltage V_{oc} is produced across the circuit in open-circuit conditions.[78-80]

Generally speaking, the photovoltaic effect involves three processes: (1) absorption of light and creation of photo-excited charge carriers, i.e., electrons-hole pairs, (2) separation of the charge carriers by some built-in electric field and finally (3) transport of the photocharges towards the metal electrodes and eventually to the external circuit. Conventionally, semiconducting materials are exploited to produce photovoltaic responses. Indeed, the semiconducting property not only helps to absorb most of the sunlight spectrum,

but also allows charge carriers transport. Despite the fact that $BiFeO_3$ is electrically insulating, it exhibits a relatively narrow bandgap compared to the other classical ferroelectrics as described in previous section. This motivated researchers to exploit it an absorbing dye in the mesoporous all-oxide solar cells. The $TiO_2/BiFeO_3/NiO$ cell demonstrated an enhanced fill factor (55%).[81] Photovoltaic effect can be classified - based on the type of built-in electric field in the photoactive layer - into two types: *barrier* and *bulk photovoltaic effects* as explained in next section.

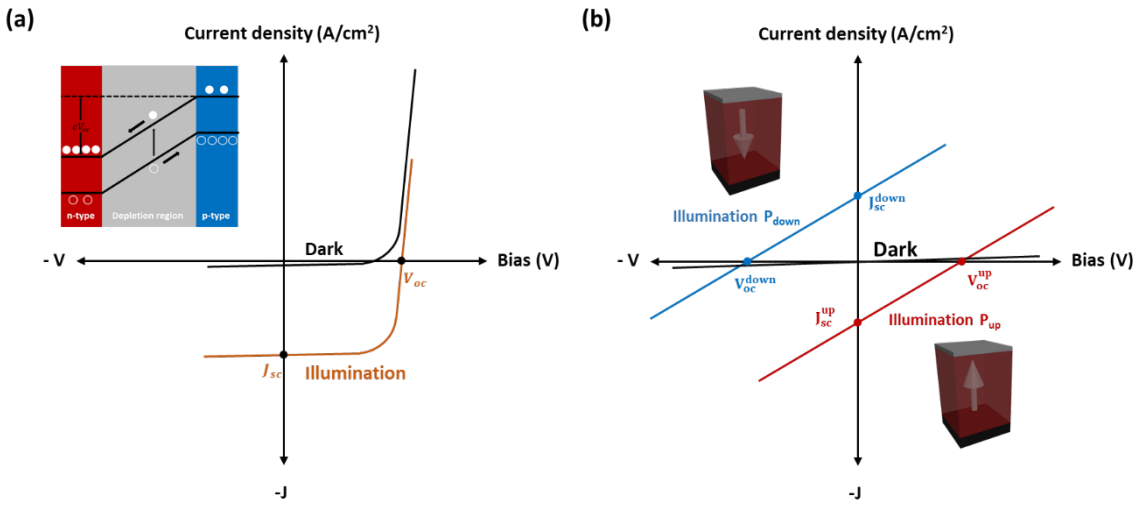

Figure 2.9: Classification of photovoltaic effects based on the mechanism of the separation of photoexcited charges. **(a)** Barrier photovoltaic effect produced in junction-based cells such as doped silicon *pn*-junctions (inset). The current-voltage characteristics are governed by the ideal diode giving rise to the IV curve assigned as "Dark". The curve is shifted to "Illumination" upon illuminating the cell by light of energy larger than the material's bandgap. **(b)** Bulk photovoltaic effect (BPVE) in homogeneous materials lacking center of symmetry. The electrical conduction is characterized by linear behavior since the material is uniform as plotted by the black line. The advantage of BPVE is the switchability following the reversal of the center of symmetry yielding a bipolar photovoltaic response (blue and red lines).

2.3.1 Barrier photovoltaic cell

Traditionally, the separation of the electron-hole pairs is handled by *pn* junctions. That is, the electrochemical asymmetry at the p-n interface gives rise to a built-in electric field that assists in separating the charge carries. As inset plot in Figure 2.9 (a) shows, in a typical

pn-junction, electrons and holes move in opposite directions under the effect of the built-in electric field towards electrodes.[79] The current-voltage equation under illumination is given by the summation of the dark current and the photocurrent of an ideal diode[82]:

$$J_{Barrier} = J_s \left[e^{\left(\frac{eV}{K_B T}\right)} - 1 \right] - J_{ph} \tag{2.7}$$

where J_s and J_{ph} are the saturation and photo-current, respectively. From equation (2.7), the open-circuit voltage is obtained by substituting J_{light} by zero[82]:

$$V_{oc} = \frac{K_B T}{e} \ln \left(\frac{J_{ph}}{J_s} + 1 \right) \sim \frac{K_B T}{e} \ln \left(\frac{J_{ph}}{J_s} \right) \tag{2.8}$$

which indicates that V_{oc} can be enlarged by decreasing the saturation current. To emphasize, the open-circuit voltage is limited by the bandgap of the semiconducting active layer since the maximum is the built-in electric field, i.e., the difference between the Fermi levels.

Also, Schottky barriers manifest themselves as barrier photovoltaic cell and hence light-to-electricity conversion is also possible. The depletion region at the semiconductor/metal interface develops electric field due to the band-bending that can act as solar cell. In this case, the metallic electrode in contact with the semiconductor must permit a considerable transparency to the light. What characterizes Schottky barrier solar cell is the higher photocurrent since the depletion region is located at the semiconductor surface although the neutral region still contributes to the total photocurrent. On the other hand, open-circuit voltages at Schottky barriers are lower than that is produced across the *pn*-junction since the maximum barrier height is around $\frac{2}{3} E_g$.[79]

2.3.2 Bulk photovoltaic effect

Noncentrosymmetric crystals generate photocurrents upon being illuminated by uniform light intensities in an unconventional way. Without the need of crystal inhomogeneities, or *pn*-junction, the absorbed light is converted into steady-state current and hence a photovoltage develops across the crystal. Additionally, the reversal of the crystal asymmetry, for instance by an external electric field in case of ferroelectric crystals, switches the photocurrent polarity as schematically plotted in Figure 2.9 (b).[83] Chynoweth[84] reported the first observation of the photovoltaic current in a ferroelectric material in 1956 (Figure 2.10 (a)). In this paper, a steady photocurrent was measured in $BaTiO_3$ single crystal in which the surface space-charge layers are claimed to be the source of the phenomenon. Similarly, Chen[85] found out, while measuring the photorefractive properties of the $LiNbO_3$ and $LiTaO_3$ single crystals, that a photocurrent flows along c-axis and opposite to the polarization of the crystals. Figure 2.10 presents the time-dependent photovoltaic current collected from $LiNbO_3$ crystal. These studies highlighted the existence of photocurrent in ferroelectric materials but unfortunately, failed to explain the origin of the photovoltaic effect.

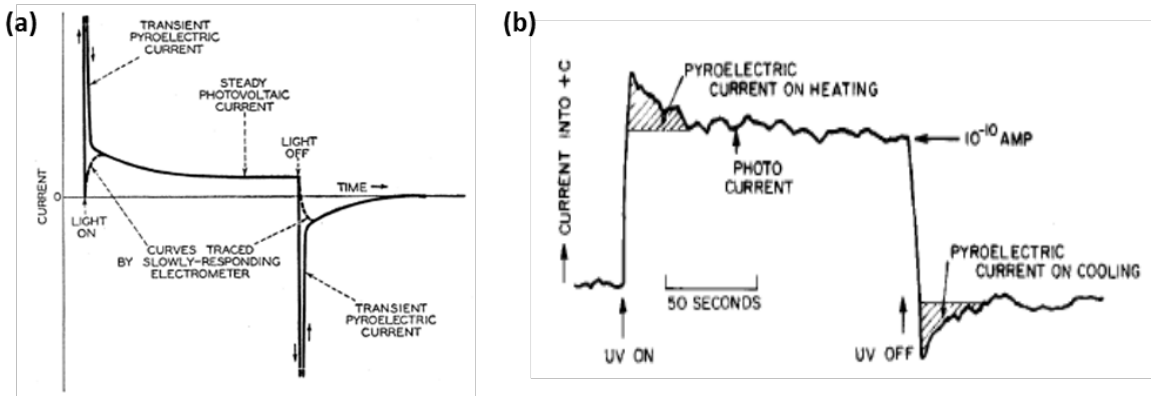

Figure 2.10: Early photovoltaic current measured in ferroelectric single crystals. **(a)** Steady-state photocurrent measured in $BaTiO_3$ single crystal while studying the pyroelectric effect.[84] **(b)** Photovoltaic current along negative direction of polarization axis in $LiNbO_3$. [85]

Various theories have been hypothesized to interpret the microscopic origin of the photovoltaic effect in noncentrosymmetric crystals. The term "Bulk photovoltaic effect" was coined in 1974 by the pioneering work done by Glass and co-workers on iron- and copper-doped $LiNbO_3$ single crystals.[83] In variance with the first observed photovoltaic effect in $BaTiO_3$[84], the photocurrent is accounted for the bulk of the material. In this work, the phenomenon was explained by an asymmetry in the charges transfer introduced by the copper and iron impurities to the lattice. A more comprehensive model was followed by Glass[86] to analyze the anomalous photovoltaic effect in doped ferroelectrics. As shown in Figure 2.11 (a), an asymmetric rectangular potential well is introduced at the impurity center, which gives rise to asymmetric charge transport due to the different probabilities of the charges scattering and recombination. Consequently, a steady photocurrent is generated throughout the bulk of the material which is given by[86]:

$$J_{ph} = k\alpha I_{opt} \tag{2.9}$$

where I is the light intensity, α is the absorption coefficient of the material and k is Glass coefficient and written as[86]:

$$k = \frac{e < \ell > P_s}{\hbar\omega} \tag{2.10}$$

With $< \ell >$ being the mean free path of the photoexcited charge carriers before scattering. This mechanism was later termed *ballistic BPVE* since it originates from the non-thermalized (or hot) carriers in momentum space. As explained in Figure 2.11 (b) and (c). Recently, the experimental measurements of the mean free path of the charge carriers revealed to be 10-100 nm.[87]

Another proposed mechanism is the *shift current* bulk PV which is of quantum mechanical origin in non-centrosymmetric crystals. It occurs when the photogenerated carriers are separated in the bulk of the crystal due to shifts in the position of their wave functions in real space.[19,88,89] In 1981, an interest in the shift current theory began when Baltz and Kraut were attempting to explain the origin of the BPVE in $BaTiO_3$.[90] It is worth noting that both shift and ballistic mechanisms coexist in noncentrosymmetric crystals with the same order of magnitude.[91] Despite the fact that shift current has not been realized experimentally, one can distinguish the ballistic mechanism through photo- Hall measurement.[87,92]

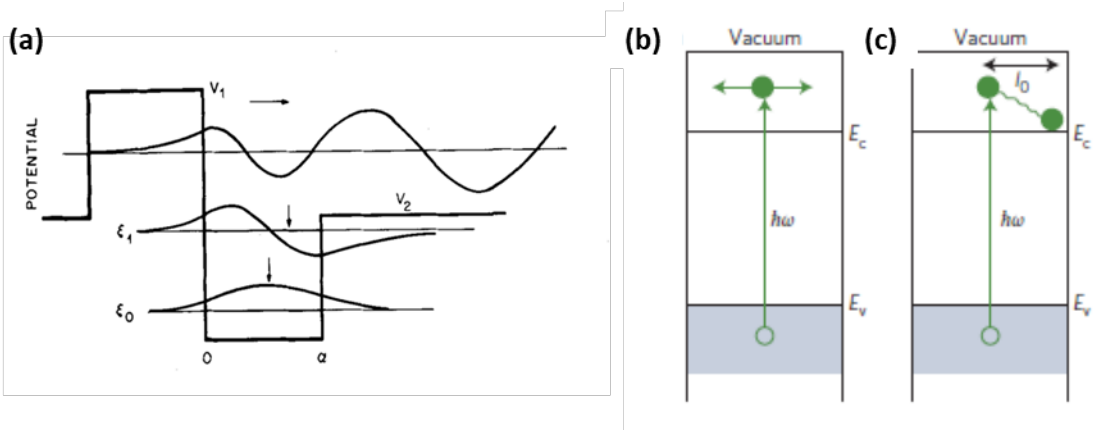

Figure 2.11: Ballistic mechanism of bulk photovoltaic effect. **(a)** Asymmetric potential barrier at the impurity center as proposed by Glass to explain the bulk photovoltaic effect in iron-doped lithium niobate Fe:$LiNbO_3$.[86] Effect of the symmetry of the crystal on the photo-excited charge carriers in **(b)** Centrosymmetric and **(c)** Non-centrosymmetric crystals.[87] Normally, the charge carriers are thermalized to the bottom of the conduction band in centrosymmetric crystals owing to the inelastic scattering. In contrast, noncentrosymmetry can shift the carriers in conduction band resulting in sizable photocurrents.

Regardless of the microscopic mechanism, bulk photovoltaic effect is a linear phenomenon. Figure 2.9 (b) depicts the structure of a typical ferroelectric photovoltaic device. Simply, it consists of ferroelectric layer sandwiched between two metal electrodes. Upon light illumination, electron-hole pairs are created and being separated by internal fields leading to photocurrent throughout the whole bulk of the crystal. Assuming the current flows parallel to the polarization, the current-voltage equation can be written as[93]:

$$J_{Bulk} = J_{sc} - (\sigma_d + \sigma_{ph})\frac{V}{d} \quad (2.11)$$

where σ_d and σ_{ph} are, respectively, the dark and photoconductivity. J_{sc} is the short-circuit current and d is the separation between the electrodes. It is clear that equation (2.11) represents a linear behavior which is different from the barrier photovoltaic effect described in equation (2.7). Hence, the developed voltage in open-circuit conditions is given by[93]:

$$V_{oc} = \frac{d}{(\sigma_d + \sigma_{ph})}.J_{sc} \quad (2.12)$$

which indicates that V_{oc} does not depend on the bandgap of the active layer but scales up with the distance between the electrodes at constant temperature.[94,95] Moreover, sufficiently low photoconductivity is necessary to obtain large photovoltages which allowed photovoltages up to 1000 V in $LiNbO_3$[83] crystals.

2.3.2.1 Crystal symmetry aspects of BPVE

Phenomenologically, bulk photovoltaic effect can be described in terms of tensors of third order. When a noncentrosymmetric crystal is illuminated by a linearly polarized monochromatic light of intensity I_{opt}, the photogenerated current is given by[95]:

$$J_{bulk} = \beta_{ijk} e_j e_k^* I_{opt} \quad (2.13)$$

where β_{ijk} is called the bulk photovoltaic tensor, which resembles the piezoelectric tensor and e is the light polarization. In other words, the structure of β_{ijk} follows the crystal symmetry.

The symmetry dependence of the photovoltaic effect given in equation (2.13) has some important physical considerations as follows. First, it turns out that lack of inversion symmetry is a requirement for the crystal to generate photocurrent with the obligation to change sign upon symmetry inversion (since J_{bulk} and e are polar vectors). Second, the magnitude (and the direction in some cases) of the photocurrent is modulated by varying the angle of the light polarization which implies the independence of the photocurrent direction on the polar axis. Third, the phenomenological theory cannot quantitatively predict the components. Finally, the photocurrent is directly proportional to the illumination

light intensity. Furthermore, the phenomenological model could not explain the origin of the bulk photovoltaic effect nor the temperature dependence.[94,95]

In literature, there is a large volume of papers reporting the modulation of the photovoltaic output by varying the illumination light linear polarization angle. In 1976, Koch et al.[96] published a paper in which they demonstrated the independence of the photocurrent

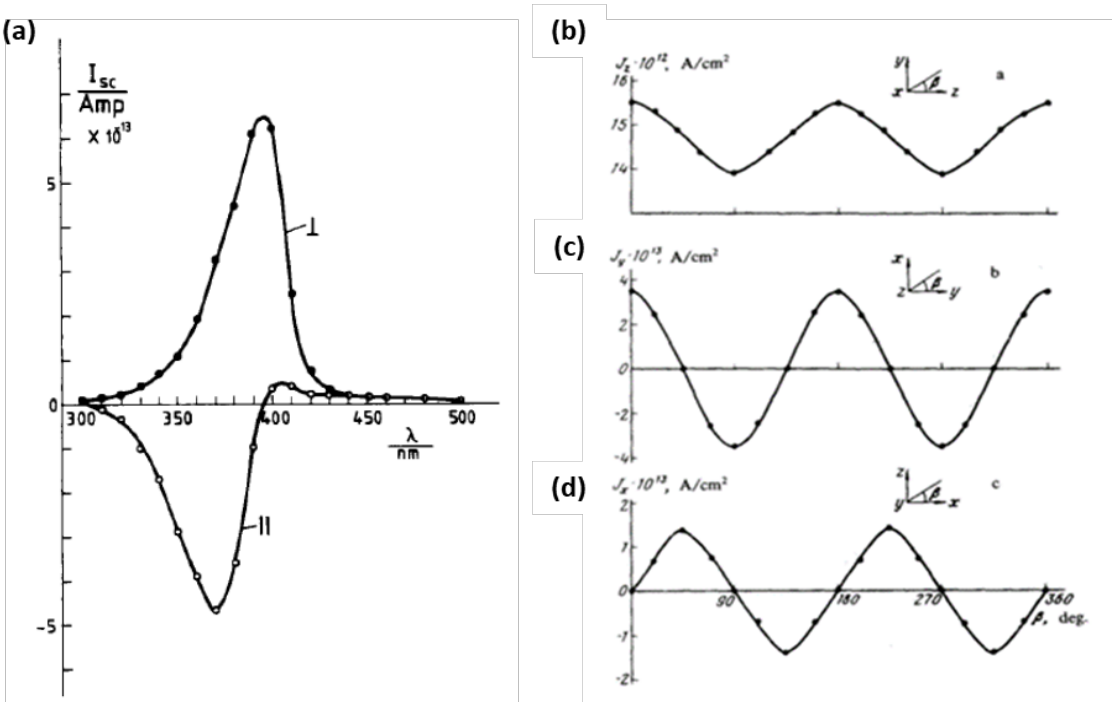

Figure 2.12: Angular dependence of the bulk photocurrent. **(a)** First observation of the dependence of the photocurrent on the light polarization in $BaTiO_3$ crystals.[96] Perpendicular light polarizations gave rise to currents of opposite directions. Sinusoidal behavior of the photocurrent in linearly polarized light illuminated Fe-doped $LiNbO_3$ crystal along z-direction **(b)**, y-direction **(c)** and x-direction **(d)**.[97]

direction on the polar axis in $BaTiO_3$. The behavior was explained by the dependence of the charge excitation on the light polarization as shown in Figure 2.12 (a). Three years later, a complete picture of the tensorial nature of the bulk photocurrent was reported for the first time in 1979 by Fridkin *et al.*[97] in iron-doped $LiNbO_3$ crystal. The same behavior was further confirmed in Cu:$LiNbO_3$ later by Festl and coauthors[98]. More recently, the same

behavior was measured in $BiFeO_3$ crystals[99] and thin films[100-103] approving the current modulation as a global feature of the bulk photovoltaic effect.

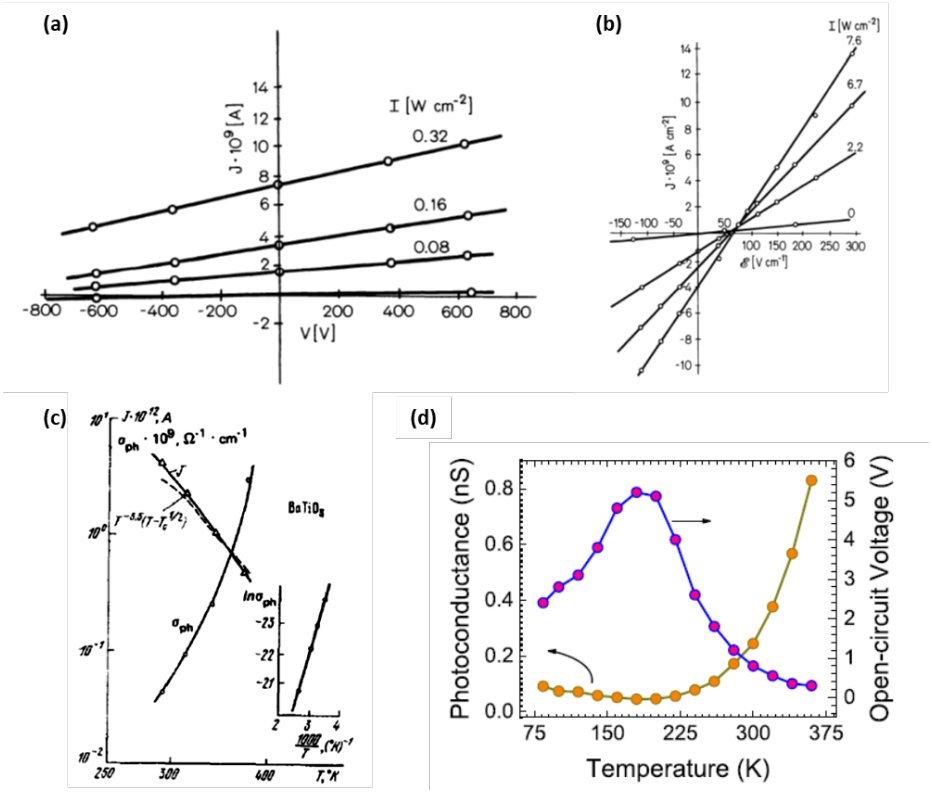

Figure 2.13: Dependence of bulk photovoltaic response on the light intensity and temperature. Light intensity dependence of the IV curves of low photoconductivity ferroelectric in **(a)** Fe:$LaNiO_3$[83] under 473 nm laser and high photoconductivity in **(b)** Fe:$KNbO_3$[104] under 488 nm illumination. Temperature-dependence of the photovoltaic behavior in **(c)** $BaTiO_3$ crystal[105] and **(d)** $BiFeO_3$ thin films[103].

2.3.2.2 Experimental aspects of bulk J_{sc} and V_{oc}

For a given separation between the electrodes, the relationship between the open-circuit voltage and short-circuit current is not straightforward. In case of highly insulating crystal ($\sigma_{ph} < \sigma_d$), V_{oc} is expected to scale up with light intensity (I_{opt}). For instance, by studying the photovoltaic behavior under different intensities of the Fe-doped $LiNbO_3$[86] crystal, V_{oc} was found to be linearly proportional to the light intensity and J_{sc} satisfies the equation ($J_{sc} \propto 10^{-8} I_{opt}$). In contrary, for $\sigma_{ph} \gg \sigma_d$, the open-circuit voltage shows

constant behavior while J_{sc} changes monotonically with the light intensity. This behavior was experimentally confirmed in several crystals with high photoconductivity such as Fe-doped $KNbO_3$[104], $BaTiO_3$[92,105] and $Ba_{0.25}Sr_{0.75}Nb_2O_6$[105]. Figure 2.13 (a) and (b) compare the J-V curves under different intensities of Fe: $LiNbO_3$ and Fe: $KNbO_3$.

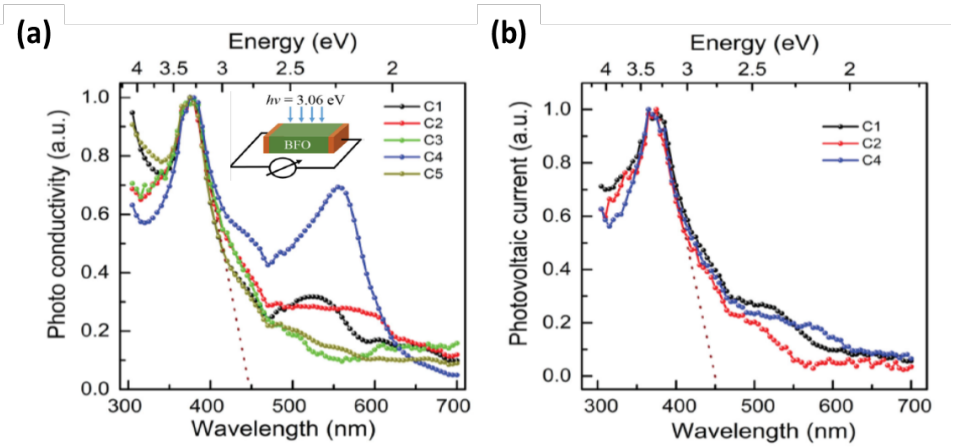

Figure 2.14: Role of defects in bulk photovoltaic effects in $BiFeO_3$ single crystal. Defects are intentionally introduced to the crystal via controlling the Bi content. **(a)** Crystal with minimal Bi ions exhibits highest photoconductivity at wavelengths below bandgap which indicates the activity of the induced gap states by Bi vacancies. **(b)** No photocurrent is detected at the corresponding wavelengths.[108]

It has been demonstrated that the mobility μ is a major contributing factor to the temperature-dependent photovoltaic behavior in ferroelectrics. In this regard, and as the temperature increases, the photoconductivity grows exponentially, and the photocurrent decreases since the carrier scattering is lowered as the crystal cooled down leading to a decaying V_{oc}. As shown in Figure 2.13 (c), the photocurrent measured in $BaTiO_3$[105] satisfied the relation $T^{-3.5}(T - T_c)^{0.5}$ which fits the temperature dependence of the mobility. Furthermore, close dependence was measured for other ferroelectrics such as $LiNbO_3$ and SbSI.[106] Recently, a correlation between the photoconductivity and the open-circuit voltage dependence on temperature was found in monodomain $BiFeO_3$ films as the temperature varies[103].

Defects in pyroelectrics are widely believed to play a major role in the bulk photovoltaic output. An asymmetric potential similar to the one introduced in Figure 2.11 (a) can exist at the impurity site which leads to asymmetry in the excitation and recombination processes and hence a dc current. This proposed mechanism was introduced to account for the PV response due to the Fe^{3+} centers in Fe:$LiNbO_3$. On the other hand, Ruppel and coworkers[107], who employed Boltzmann transport equations, concluded that defects are required to generate photocurrent in ferroelectrics. In other words, the gap states introduce an alternative recombination path which is believed to be the origin of the substantial enhancement of PV behavior in nonstoichiometric $BiFeO_3$ crystals.[103,108] As sown in Figure 2.14, a considerable photoconductivity emerges in $BiFeO_3$ crystals at below-bandgap wavelengths as the Bi vacancies are introduced to the crystal increasing the PV in crystal (C1), i.e., with the highest defects density. More interestingly, Matsuo *et al.* attributed the PV enhancement in (ref.100) to an additional PV mechanism due to two-absorption through the sub-band levels through Mn doping.

When it comes to the charge collection, device size matters. Pyroelectrics are characterized by their wide bandgap and poor charge transport leading to high recombination rates. Downscaling of the device size that can be manipulated by small electrodes represents a promising way to enhance the charge collection efficiency. It was 2011 when Alexe and Hesse[109] employed nanoscale top electrodes that colossally enhanced the external quantum efficiency by 10^7-fold under 405 nm light. Moreover, by using the same approach, Spanier *et al.*[92] could obtain PCE efficiency of 4.8% which is beyond the Shockley-Queisser limit of $BaTiO_3$ single crystals.

2.3.3 Photovoltaic in ferroelectric thin films: Understanding the controversy

The origin of the photovoltaic response in ferroelectric thin films has been a controversial and disputed subject in the scientific community. In their seminal article, Choi and coworkers[99] reported a switchable photovoltaic effect in $BiFeO_3$ single crystals. In this work, the bulk mechanism was claimed to be the origin of this behavior since a sinusoidal modulation of the photocurrent was revealed. Since then, a large body of literature has

investigated the photovoltaic effect in ferroelectric thin films suggesting the band-bending at the ferroelectric/metal interface, the depolarization field or even the ferroelectric domain walls are behind the PV effect as summarized in table (2.1). This section sheds the light on the controversies of the possible mechanism(s) of the photovoltaic effect in ferroelectric thin film with the photocurrent measured along and normal to the illumination direction.

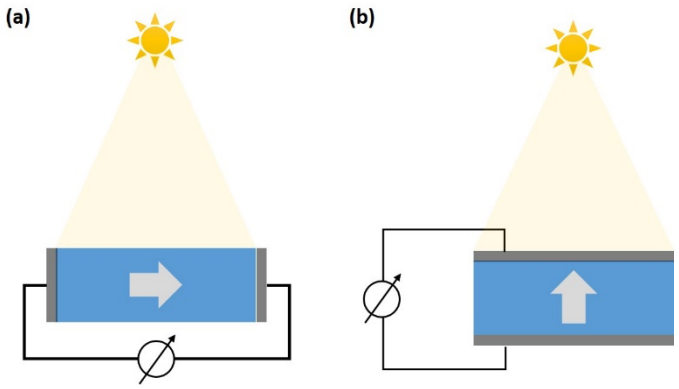

Figure 2.15: Ferroelectric photovoltaic device configurations. **(a)** Planar configuration where the active layer is directly illuminated while the current is measured along the in-plane direction. **(b)** Vertical configuration with the current is collected parallel to the illumination direction.

2.3.3.1 Planar configuration

In co-planar electrode configuration as depicted in Figure 2.15 (a), the interface and depolarization field effects are eliminated, and the illumination is provided perpendicular to the active layer. At a glance, this geometry seems to offer an ideal platform to explore the bulk photovoltaic mechanism with deeper insight. This is clear in monodomain thin films with in-plane ferroelectric polarization component such as $BiFeO_3$. For instance, in references (100 and 103), the researchers exploited the aforementioned sample which enabled them to explore the role of the defect states in the bulk photovoltaic output as explained in the previous section. However, introducing periodic domain walls to the ferroelectric films promoted heated debate in the oxides community.

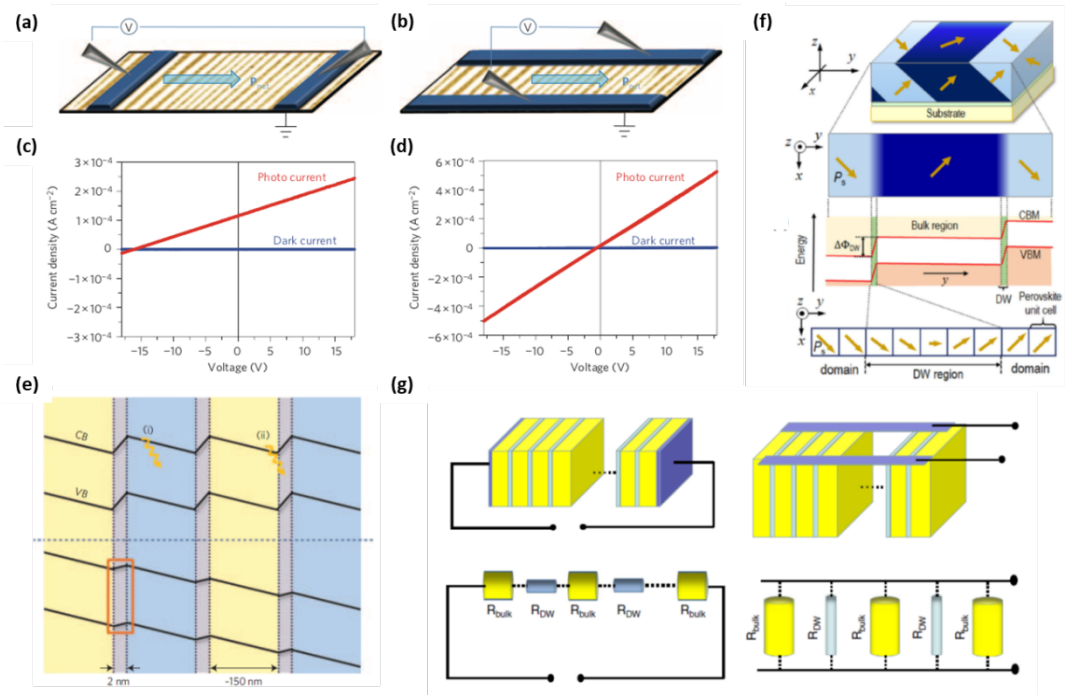

Figure 2.16: Impact of domain walls on the photovoltaic output in $BiFeO_3$ films with periodic 71° DWs. Devices under test shined by unpolarized white light with co-planar electrodes parallel **(a)** and perpendicular **(b)** to the domain walls generating photovoltaic response **(c)** and photoconductivity **(d)**, respectively.[110, 112] **(e)** The behavior was explained solely by electrostatic potential step at the DWs. Employing linearly polarized 405 nm laser source, a sizable PV output measured in both directions which is explained by contributions from the local noncentrosymmetry as well as the band-bending at the DWs **(f)**.[52] On contrary, the measured effect was interpreted by the bulk PV mechanism in which the DWs controlling the overall photoconductivity **(g)**.[102] Hence, the device was modeled as resistors connected in either series or parallel giving rise to anisotropic PV response.

$BiFeO_3$ films grown with anisotropic in-plane strain induced by orthorhombic substrates exhibit periodic DWs, namely 71° and/or 109°.[102,110,111] The impact of the domain walls (DWs) on the overall photovoltaic response in ferroelectrics has divided opinion. In the first report published in 2010, the potential steps at the 71° DWs were thought as photo-electromotive sources that assist in e-h dissociation yielding 10% internal quantum efficiency the wall.[110,112] On the other hand, and by systematically studying the temperature dependence behavior of the PV, the role of the DWs was confined to the variation of the photoconductivity of the film. The photovoltaic response stemmed from purely bulk PV

mechanism similar to the monodomain films.[102,113,114] This interpretation was further confirmed by the first principles calculations claiming that the PV response in such sample is dominated by the shift current mechanism.[19] More third-party involvement by Matsuo *et al.*[52] who emphasized that the structural symmetry breaking and the electrostatic potentials at the DWs add up to the bulk PV mechanism. Figure 2.16 presents the dispute in the field on the role of the domain walls in the photovoltaic effect in ferroelectric thin films.

2.3.3.2 Vertical configuration

In vertical capacitors, the photovoltaic response is measured by illuminating the device through the top electrode as shown in Figure 2.15 (b). In variance with the planar structure, Schottky barrier and depolarization field may play a dominating role since the active layer is very thin. Moreover, the aforementioned PV mechanisms have much in common such as the switchability making it challenging to separate the different mechanisms. Thus,

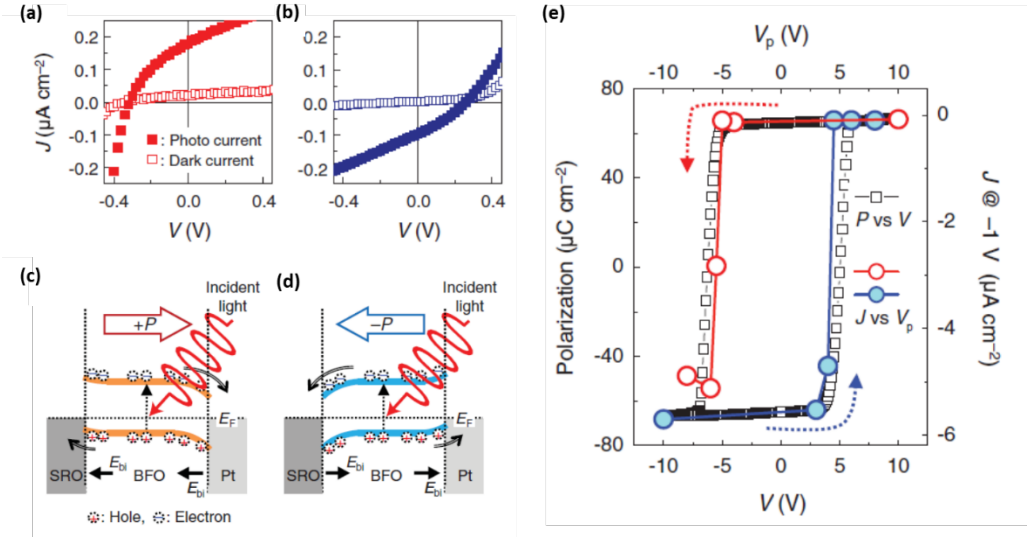

Figure 2.17: Ferroelectric polarization-modulated Schottky barrier photovoltaic effect in $Pt/BiFeO_3/SrRuO_3$ heterostructure. Current density-voltage curves in dark and light conditions associated with the ferroelectric polarization in up- **(a)** and down- **(b)** states. The switchable behavior was explained by the modulation of Schottky barrier from up **(c)** to down **(d)** states. Also, monitoring the photocurrent evolution with the applied voltage pulses led to a hysteretic behavior superimposed on the polarization-electric field loops **(e)**. Taken from Ref. 32.

scattered opinion in literature on the dominated mechanism in ferroelectric thin films as follows.

It has been argued that band-bending PV dominates the overall FePV in vertical capacitors. As discussed in section 2.1.2, Schottky barrier forms at the ferroelectric/metal interfaces which allows a polarization-modulated PV response. For example, hysteretic photocurrent were measured in $Pb(Zr, Ti)O_3$[115,116] and $BiFeO_3$[32] that is superimposed on the polarization-electric field loops as demonstrated in Figure 2.17. These studies indicate the modulation of the Schottky barrier by the ferroelectric polarization ignoring the impact of the symmetry breaking. Interestingly, Guo *et al.*[45] successfully used this property to nondestructively read out the polarization state for memories applications. Furthermore, high PCE efficiency (2.49%) was obtained in ultrathin PZT films elucidating the major role played by Schottky barrier in determining the PV output.[117] Unfortunately, this device design lacks one of the advantages of FePV, i.e., the switchability, since the active layer is too thin leading to a depletion layer spreading through the whole thickness. Further research that supports this argument was published by You *et al.* where the photocurrent was greatly enhanced in La-doped $BiFeO_3$ epitaxial films compared to the stoichiometric one. In this work, the crystal symmetry of $BiFeO_3$ was tailored to the morphotropic phase boundary, i.e., a mixture of non- and centrosymmetric rhombohedral and orthorhombic phases. At this composition, the ferroelectric polarization is destabilized prolonging the carriers lifetimes in the bulk of the $BiFeO_3$ film.[31]

A different perspective, however, suggests that the depolarization field is associated with separation of the photoexcited charges. This argument is based on the existing remnant E_{dep} which is switchable upon reversing the polarization as well. This is exemplified in the research on the epitaxial $(Pb_{0.97}La_{0.03})(Zr_{0.52}Ti_{0.48})O_3$ films of 68 nm thickness in which 0.28% efficiency was achieved. The enhancement of the PV behavior was achieved by downscaling the thickness and attributed to the stronger depolarizing field.[118] In a subsequent theoretical paper[119], the depolarizing field was further emphasized as a major PV mechanism in ferroelectric thin film. The study predicted PCE up to 19.5% in ferroelectrics with strong depolarization field, i.e., in ultrathin films in contact with high

dielectric constant metallic electrodes. Practically, poling such ultrathin ferroelectric films is a big challenge.

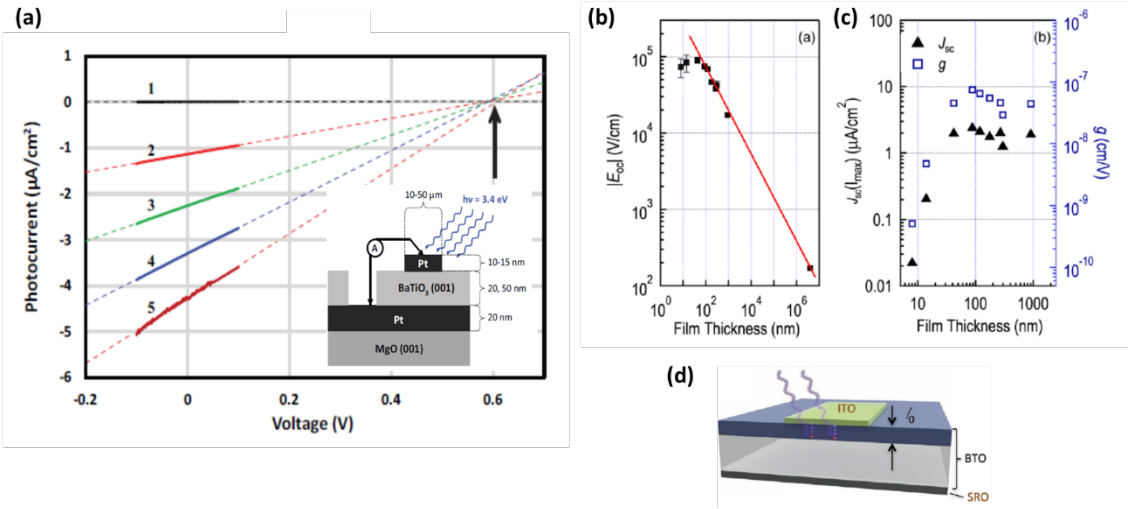

Figure 2.18: Ballistic current mechanism measured in $BaTiO_3$ thin films. **(a)** IV curves measured in Pt/(20 nm)$BaTiO_3$/Pt stack under different light intensities revealing ~1% efficiency. The $BaTiO_3$ thickness scaling of the V_{oc} **(b)** and photocurrent **(c)** demonstrate the PV enhancement after exceeding the mean free path of the nonthermalized charge carriers **(d)**.[87,122, 123]

Imprint fields, or the internal fields built up by charged defects and dipoles, are known in ferroelectrics to hinder its operation. Hence, it is expected that these fields may affect the ferroelectric PV response or even dominate it. Building on this idea, Gao *et al.*[120] explored the impact of the oxygen vacancies formed in $Bi_{0.9}La_{0.1}FeO_3$ films on ferroelectric PV illuminated by a below-bandgap laser source ($\lambda = 532$ nm). By applying voltage pulses below the coercive voltage could switch the photocurrent indicating that its origin is correlated with the internal fields stemming from $V_o^{\cdot\cdot}$ layers accumulated at either interface. Similarly, Matsuo and co-workers agreed with Gao's findings using different approach to manipulate the oxygen vacancies in $BiFeO_3$ films. In their article, the samples are annealed to form positively charged layer at one of the two interfaces and found to cooperate with band-bending to determine the PV output.[121] It is worth noting that the bulk PV was excluded in these reports.

Another angle on this debate suggests the bulk photovoltaic effect dominated the PV output if measured in the ballistic regime. It was 2014 when researchers could realize the ballistic photocurrents in $BaTiO_3$ thin films for the first time as shown in figure 2.18. The PV measurements revealed ~1% efficiency in 20 nm thin films under UV illumination which is around 4 orders-of-magnitude larger than the single crystals.[122] In a subsequent article, the systematic tuning of the active layer thickness unraveled a mean free path of ~100 nm of the photogenerated charges.[87] It should be noted that in these studies the ballistic nature of the photoexcited charges is confirmed through photo-Hall effect[123] measured in $BaTiO_3$ single crystals. More importantly, the authors did not exclude the shift current as a contributor to the total current. Shift current has not been realized experimentally in ferroelectric thin films yet.

On the other hand, these investigations lack a number of unaddressed questions. Firstly, the switchability property of the photovoltaic behavior which is predicted by equation (2.13) hasn't been studied. Secondly, the authors did not report the tensorial behavior of the ballistic current which would further. It is well known that photocurrent modulation with relative angle of the light polarization is characteristic to the BPV. Thirdly, the role of size of top electrodes in the output was not highlighted although it was demonstrated that in single crystal $BaTiO_3$ the size effect does not matter.[92] Addressing these issues would assist in pushing the limits of the bulk photovoltaic effect towards real life applications.

Table 2.1: Summary of the scattered opinion on the possible origin(s) of ferroelectric photovoltaic effects in literature.

Heterostructure	Device configuration	Lightening	Proposed dominating PV mechanism	Strategy/Evidence	Year
Pt/PZT/Pt[115]	Vertical	365 nm	Interface band-bending	- Hysteretic photocurrents resembling PE loop - First time to demonstrate the polarization-dependent modulated Schottky interfaces	2000
LSMO/(001)-PLZT/Nb:STO[118]	Vertical	365 nm (up to 15 mW/cm^2)	Depolarization field	- 0.28% efficiency in 68 nm thin film - Simulations predicts higher efficiencies in thinner films since the depolarization field is stronger.	2008
ITO/BFO/SRO[124]	Vertical	Unpolarized white light (AM 1.5)	Interface band-bending	- V_{OC} increases linearly with BFO thickness before saturating at 200 nm (0.8-0.9 V) - This is attributed to the interface depletion layer which is estimated to be ~300 nm in width	2009

(001)-BFO/DSO[110]	Lateral	Unpolarized white light (285 mW/cm^2)	Electrostatic potential at domain walls	- Above-bandgap V_{OC} (16 V) produced when current is measured normal to the 71º DWs in contrary to the parallel current which showed photoconductivity	2010
Au/(001)-BFO/SRO[125]	Vertical	435 nm laser (20 mW/cm^2)	Bulk PV	- Schottky barrier contribution to the PV is excluded since symmetric Schottky barriers measured at both interfaces	2010
(111)-BFO/STO[126]	Lateral	Linearly polarized 435 nm laser (20 mW/cm^2)	Bulk PV	- Evidenced by the tensorial behavior for the first time in monodomain BFO films - Band-bending and depolarization field don't contribute the PV in this case	2011
(001)-BFO/DSO[127]	Lateral	Unpolarized white light	Electrostatic potential steps at 109º domain walls	- Modulated in-plane photocurrent from negative to positive upon switching the 109º domains	2011
Pt/(001)-BFO/SRO[128]	Vertical	Unpolarized white light (10 mW/cm^2)	Interface band-bending	- The photocurrent was found to follow the PE loop in BFO indicating the modulation of the Schottky barrier by the bulk polarization.	2011
Fe/(001)-BFO/LSMO[45]	Vertical	Unpolarized White light (5-20 mW/cm^2)	Interface band-bending	- Emphasized the role played by the polarization to modulate the Schottky barrier - PV exploited to read polarization states (0 and 1)	2013
(001)-BFO/TSO[102]	Lateral	Linearly-polarized 405 nm laser (max power 80 mW)	Bulk PV	- V_{OC} = 50V - Temperature-dependent PV measurements proved the BPV nature of the PV response - DW are highly conductive preventing them from contributing much to overall PV response	2013
Ag/(001)-BLFO/LSMO[120]	Vertical	532 nm laser (100 mW/cm^2)	Internal defect-induced fields	- The sign of photocurrent is independent of the direction of polarization	2014
Pt/(001)-BFO/LSMO[129]	Vertical	Unpolarized white light (20 mW/cm^2)	Interface-induced	- Conductive domain walls contribute to the total photocurrent but don't affect the open-circuit voltage	2014
ITO/(001)-BFCO/STO[130]	Vertical	Unpolarized white light	Interface band-bending	- Switchable PV behavior in the double perovskite Bi_2FeCrO_6 with diode-like IV curves. - Substantial efficiency of 8% was achieved in tandem cell of 3 layers with different bandgaps	2014
Pt/(001)-BTO/Pt[122]	Vertical	360 nm (500 mW/cm^2)	Bulk PV – Ballistic mechanism	- 4 order-of-magnitude enhancement in efficiency in 20 nm thin films compared to bulky BTO	2014
(001)-BFO/BST/STO[52] ***(Stripe DWs)***	Lateral	Linearly-polarized 405 nm laser (2.5 W/cm^2)	Bulk PV as well as the noncentrosymmetry and electrostatic potential at 71º DW	- Proved through the tensorial nature of the bulk PV - The modulated current could only fitted by using function composed of BPV + the noncentrosymmetry + Electrostatic potential step	2016
SRO/(001)-BFMO/SRO[121]	Vertical	405 nm laser (500 mW/cm^2)	Cooperative interface band-bending and built-in defect fields ($V_O^{\cdot\cdot}$)	- The Schottky barrier heights were modulated by annealing the device giving rise to modulated photovoltaic effects	2016
Pt/(001)-BTO/SRO[87]	Vertical	405 nm laser (182 mW/cm^2)	Bulk PV - Ballistic mechanism	- Photocurrent scales down with the thickness indicating a large mean free path	2017
(001)-BFO/STO[131]	Lateral	Linearly-polarized 405 nm laser	Bulk PV	- Tensorial behavior in monodomain films	2017
(001)-BFMO/STO[132]	Lateral	Linearly-polarized 405, 520 and 630 nm lasers	Bulk PV	- Tensorial behavior in monodomain films. Inserting half-filled gap states enhanced the PV behavior (PV response emerges at 630 nm)	2017

Pt/(001)BLFO/LSMO[24]	Vertical	Unpolarized white light (20 mW/cm^2)	Interface band-bending	- One order-of-magnitude enhancement in photocurrent at morphotropic phase boundary although symmetry is lowered - Enhances the idea that the interface mechanism dominates the PV response in vertical cells.	2018
Pt/(001)-PZT/STO[117]	Vertical	365 nm	Interface band-bending	- Up to 2.49% efficiency in 12 nm film with 5 um top electrode enhances the concept of interface band-bending as a dominating PV mechanism in ferroelectric thin films and the role of the charge collection efficiency	2019
ITO/(112)-$Bi_4V_2O_{11}$@$BiVO_4$/LNO[133]	Vertical	Unpolarized white light (AM 1.5 G)	Bulk PV stemmed from the polar $Bi_4V_2O_{11}$ regions in the $BiVO_4$ matrix	- The device could generate PV only when the active layer thickness (10 nm) is comparable to the size of the $Bi_4V_2O_{11}$ poled regions	2020

References

1. Valasek, J. *Piezo-electric and allied phenomena in rochelle salt* Master of Science thesis, University of Minnesota, (1920).

2. Cross, L. E. N., R. E. . History of Ferroelectrics *Conference proceedings* (1986).

3. Sawaguchi, E. Ferroelectricity versus antiferroelectricity in the solid solutions of $PbZrO_3$ and $PbTiO_3$. *Journal of the physical society of Japan* **8**, 615-629 (1953).

4. Inbar, I. & Cohen, R. E. Origin of ferroelectricity in $LiNbO_3$ and $LiTaO_3$. *Ferroelectrics* **194**, 83-95, doi:10.1080/00150199708016084 (1997).

5. Teague, J. R., Gerson, R. & James, W. J. Dielectric hysteresis in single crystal $BiFeO_3$. *Solid State Communications* **8**, 1073-1074, doi:https://doi.org/10.1016/0038-1098(70)90262-0 (1970).

6. Lines, M. E. & Glass, A. M. *Principles and applications of ferroelectrics and related materials*. (Oxford university press, 2001).

7. Rabe, K. M. A., C. H.; Triscone, J. *Physics of Ferroelectrics*. (2007).

8. Xu, Y. *Ferroelectric Materials and their Applications*. (1991).

9. Guyonnet, J. in *Ferroelectric Domain Walls Springer Theses* Ch. Chapter 2, 7-24 (2014).

10. Damjanovic, D. Ferroelectric, dielectric and piezoelectric properties of ferroelectric thin films and ceramics. *Reports on Progress in Physics* **61**, 1267-1324, doi:10.1088/0034-4885/61/9/002 (1998).

11. Kepler, R. G. Piezoelectricity, pyroelectricity, and ferroelectricity in organic materials. *Annual Review Physical Chemistry*, 497-518 (1987).

12. Nye, J. F. *Physical properties of crystals: their representation by tensors and matrices*. (Oxford university press, 1985).

13. Newnham, R. E. *Properties of Materials: Anisotropy, Symmetry, Structure*. (OUP Oxford, 2005).

14. Schottky, W. Halbleitertheorie der Sperrschicht. *Naturwissenschaften* **26**, 843-843, doi:10.1007/BF01774216 (1938).

15. Manzo, M. *Engineering ferroelectric domains and charge transport by proton exchange in lithium niobate* 2015:15 thesis, KTH Royal Institute of Technology, (2015).

16. Würfel, P. & Würfel, U. *Physics of solar cells: from basic principles to advanced concepts*. (John Wiley & Sons, 2016).

17. Pintilie, L. & Alexe, M. Metal-ferroelectric-metal heterostructures with Schottky contacts. I. Influence of the ferroelectric properties. *Journal of applied physics* **98**, 124103 (2005).

18. Ramesh, R. *et al.* Fatigue and retention in ferroelectric Y-Ba-Cu-O/Pb-Zr-Ti-O/Y-Ba-Cu-O heterostructures. *Applied physics letters* **61**, 1537-1539 (1992).

19. Young, S. M., Zheng, F. & Rappe, A. M. First-principles calculation of the bulk photovoltaic effect in bismuth ferrite. *Phys Rev Lett* **109**, 236601, doi:10.1103/PhysRevLett.109.236601 (2012).

20. Paillard, C., Xu, B., Dkhil, B., Geneste, G. & Bellaiche, L. Photostriction in Ferroelectrics from Density Functional Theory. *Physical Review Letters* **116**, 247401, doi:10.1103/PhysRevLett.116.247401 (2016).

21. Spaldin, N. A. & Fiebig, M. The Renaissance of Magnetoelectric Multiferroics. *Science* **309**, 391-392, doi:10.1126/science.1113357 (2005).

22. Sando, D., Xu, B., Bellaiche, L. & Nagarajan, V. A multiferroic on the brink: Uncovering the nuances of strain-induced transitions in $BiFeO_3$. *Applied Physics Reviews* **3**, doi:10.1063/1.4944558 (2016).

23. Sando, D., Barthelemy, A. & Bibes, M. BiFeO3 epitaxial thin films and devices: past, present and future. *J Phys Condens Matter* **26**, 473201, doi:10.1088/0953-8984/26/47/473201 (2014).

24. Yi, J. & Li, S. *Functional Materials and Electronics*. (2018).

25. Moreau, J. M., Michel, C., Gerson, R. & James, W. J. Ferroelectric $BiFeO_3$ X-ray and neutron diffraction study. *Journal of Physics and Chemistry of Solids* **32**, 1315-1320, doi:https://doi.org/10.1016/S0022-3697(71)80189-0 (1971).

26. Royen, P. & Swars, K. Das System Wismutoxyd-Eisenoxyd im Bereich von 0 bis 55 Mol% Eisenoxyd. *Angewandte Chemie* **69**, 779-779 (1957).

27. Kubel, F. & Schmid, H. Structure of a ferroelectric and ferroelastic monodomain crystal of the perovskite BiFeO3. *Acta Crystallographica Section B* **46**, 698-702, doi:10.1107/s0108768190006887 (1990).

28. Baek, S.-H., Choi, S., Kim, T. L. & Jang, H. W. Domain engineering in $BiFeO_3$ thin films. *Current Applied Physics* **17**, 688-703, doi:https://doi.org/10.1016/j.cap.2017.02.016 (2017).

29. Yang, J.-C. *et al.* Orthorhombic $BiFeO_3$. *Physical review letters* **109**, 247606 (2012).

30. Folkman, C. M. *et al.* Stripe domain structure in epitaxial (001) $BiFeO_3$ thin films on orthorhombic $TbScO_3$ substrate. *Applied Physics Letters* **94**, 251911, doi:10.1063/1.3152009 (2009).

31. You, L. *et al.* Enhancing ferroelectric photovoltaic effect by polar order engineering. *Science advances* **4**, eaat3438 (2018).

32. Lee, D. *et al.* Polarity control of carrier injection at ferroelectric/metal interfaces for electrically switchable diode and photovoltaic effects. *Physical Review B* **84**, 125305, doi:10.1103/PhysRevB.84.125305 (2011).

33. Zhou, Y. *et al.* Photovoltaic property of domain engineered epitaxial BiFeO3 films. *Applied Physics Letters* **105**, 252903, doi:10.1063/1.4905000 (2014).

34. Damodaran, A. R. *et al.* Nanoscale structure and mechanism for enhanced electromechanical response of highly strained $BiFeO_3$ thin films. *Advanced Materials* **23**, 3170-3175 (2011).

35. Liu, H. *et al.* Origin of a tetragonal BiFeO3 phase with a giant c/a ratio on SrTiO3 substrates. *Advanced Functional Materials* **22**, 937-942 (2012).

36. Zeches, R. *et al.* A strain-driven morphotropic phase boundary in $BiFeO_3$. *science* **326**, 977-980 (2009).

37. Neaton, J. B., Ederer, C., Waghmare, U. V., Spaldin, N. A. & Rabe, K. M. First-principles study of spontaneous polarization in multiferroic $BiFeO_3$. *Physical Review B* **71**, 014113, doi:10.1103/PhysRevB.71.014113 (2005).

38. Seshadri, R. & Hill, N. A. Visualizing the Role of Bi 6s “Lone Pairs” in the Off-Center Distortion in Ferromagnetic $BiMnO_3$. *Chemistry of Materials* **13**, 2892-2899, doi:10.1021/cm010090m (2001).

39. Ravindran, P., Vidya, R., Kjekshus, A., Fjellvåg, H. & Eriksson, O. Theoretical investigation of magnetoelectric behavior in $BiFeO_3$. *Physical Review B* **74**, 224412, doi:10.1103/PhysRevB.74.224412 (2006).

40. Wang, J. *et al.* Epitaxial $BiFeO_3$ multiferroic thin film heterostructures. *science* **299**, 1719-1722 (2003).

41. Fousek, J. & Janovec, V. The Orientation of Domain Walls in Twinned Ferroelectric Crystals. *Journal of Applied Physics* **40**, 135-142, doi:10.1063/1.1657018 (1969).

42. Romanov, A. E. *et al.* Domain pattern formation in epitaxial rhombohedral ferroelectric films. II. Interfacial defects and energetics. *Journal of Applied Physics* **83**, 2754-2765, doi:10.1063/1.366636 (1998).

43. Streiffer, S. *et al.* Domain patterns in epitaxial rhombohedral ferroelectric films. I. Geometry and experiments. *Journal of applied physics* **83**, 2742-2753 (1998).

44. Baek, S. H. *et al.* Ferroelastic switching for nanoscale non-volatile magnetoelectric devices. *Nat Mater* **9**, 309-314, doi:10.1038/nmat2703 (2010).

45. Guo, R. *et al.* Non-volatile memory based on the ferroelectric photovoltaic effect. *Nat Commun* **4**, 1990, doi:10.1038/ncomms2990 (2013).

46. Chu, Y.-H., Martin, L. W., Holcomb, M. B. & Ramesh, R. Controlling magnetism with multiferroics. *Materials Today* **10**, 16-23 (2007).

47. Lebeugle, D., Colson, D., Forget, A. & Viret, M. Very large spontaneous electric polarization in $BiFeO_3$ single crystals at room temperature and its evolution under cycling fields. *Applied Physics Letters* **91**, 022907, doi:10.1063/1.2753390 (2007).

48. Chu, Y.-H. *et al.* Nanoscale control of domain architectures in $BiFeO_3$ thin films. *Nano letters* **9**, 1726-1730 (2009).

49. Seidel, J. *et al.* Conduction at domain walls in oxide multiferroics. *Nature Materials* **8**, 229-234, doi:10.1038/nmat2373 (2009).

50. Lubk, A., Gemming, S. & Spaldin, N. A. First-principles study of ferroelectric domain walls in multiferroic bismuth ferrite. *Physical Review B* **80**, 104110, doi:10.1103/PhysRevB.80.104110 (2009).

51. Farokhipoor, S. & Noheda, B. Conduction through 71 degrees domain walls in $BiFeO_3$ thin films. *Phys Rev Lett* **107**, 127601, doi:10.1103/PhysRevLett.107.127601 (2011).

52. Matsuo, H. *et al.* Bulk and domain-wall effects in ferroelectric photovoltaics. *Physical Review B* **94**, doi:10.1103/PhysRevB.94.214111 (2016).

53. Yang, J. C., Huang, Y. L., He, Q. & Chu, Y. H. Multifunctionalities driven by ferroic domains. *Journal of Applied Physics* **116**, 066801, doi:10.1063/1.4891632 (2014).

54. Fischer, P., Polomska, M., Sosnowska, I. & Szymanski, M. Temperature dependence of the crystal and magnetic structures of $BiFeO_3$. *Journal of Physics C: Solid State Physics* **13**, 1931-1940, doi:10.1088/0022-3719/13/10/012 (1980).

55. Ramazanoglu, M. *et al.* Local Weak Ferromagnetism in Single-Crystalline Ferroelectric $BiFeO_3$. *Physical Review Letters* **107**, 207206, doi:10.1103/PhysRevLett.107.207206 (2011).

56. Chen, Z. *et al.* Complex strain evolution of polar and magnetic order in multiferroic $BiFeO_3$ thin films. *Nat Commun* **9**, 3764, doi:10.1038/s41467-018-06190-5 (2018).

57. Sosnowska, I., Neumaier, T. P. & Steichele, E. Spiral magnetic ordering in bismuth ferrite. *Journal of Physics C: Solid State Physics* **15**, 4835-4846, doi:10.1088/0022-3719/15/23/020 (1982).

58. Lebeugle, D. *et al.* Electric-Field-Induced Spin Flop in $BiFeO_3$ Single Crystals at Room Temperature. *Physical Review Letters* **100**, 227602, doi:10.1103/PhysRevLett.100.227602 (2008).

59. Herrero-Albillos, J. *et al.* Neutron diffraction study of the $BiFeO_3$ spin cycloid at low temperature. *Journal of Physics: Condensed Matter* **22**, 256001, doi:10.1088/0953-8984/22/25/256001 (2010).

60. Ruette, B. *et al.* Magnetic-field-induced phase transition in $BiFeO_3$ observed by high-field electron spin resonance: Cycloidal to homogeneous spin order. *Physical Review B* **69**, 064114, doi:10.1103/PhysRevB.69.064114 (2004).

61. Wardecki, D., Przeniosło, R., Sosnowska, I., Skourski, Y. & Loewenhaupt, M. Magnetization of Polycrystalline $BiFeO_3$ in High Magnetic Fields. *Journal of the Physical Society of Japan* **77**, 103709, doi:10.1143/JPSJ.77.103709 (2008).

62. Kuo, C. Y. *et al.* Single-domain multiferroic $BiFeO_3$ films. *Nature Communications* **7**, 12712, doi:10.1038/ncomms12712 (2016).

63. Bai, F. *et al.* Destruction of spin cycloid in $(111)_c$-oriented $BiFeO_3$ thin films by epitiaxial constraint: Enhanced polarization and release of latent magnetization. *Applied Physics Letters* **86**, 032511, doi:10.1063/1.1851612 (2005).

64. Béa, H., Bibes, M., Petit, S., Kreisel, J. & Barthélémy, A. Structural distortion and magnetism of $BiFeO_3$ epitaxial thin films: A Raman spectroscopy and neutron diffraction

study. *Philosophical Magazine Letters* **87**, 165-174, doi:10.1080/09500830701235802 (2007).

65. Cheng, C.-J. *et al.* Thickness-dependent magnetism and spin-glass behaviors in compressively strained $BiFeO_3$ thin films. *Applied Physics Letters* **98**, 242502, doi:10.1063/1.3600064 (2011).

66. Ramazanoglu, M. *et al.* Local Weak Ferromagnetism in Single-Crystalline Ferroelectric $BiFeO_3$. *Physical Review Letters* **107**, 207206, doi:10.1103/PhysRevLett.107.207206 (2011).

67. Chen, Z. *et al.* Complex strain evolution of polar and magnetic order in multiferroic $BiFeO_3$ thin films. *Nature Communications* **9**, 3764, doi:10.1038/s41467-018-06190-5 (2018).

68. Gujar, T. P., Shinde, V. R. & Lokhande, C. D. Nanocrystalline and highly resistive bismuth ferric oxide thin films by a simple chemical method. *Materials Chemistry and Physics* **103**, 142-146, doi:https://doi.org/10.1016/j.matchemphys.2007.02.003 (2007).

69. Ihlefeld, J. F. *et al.* Optical band gap of $BiFeO_3$ grown by molecular-beam epitaxy. *Applied Physics Letters* **92**, 142908, doi:10.1063/1.2901160 (2008).

70. Schmidt, D., You, L., Chi, X., Wang, J. & Rusydi, A. Anisotropic optical properties of rhombohedral and tetragonal thin film $BiFeO_3$ phases. *Physical Review B* **92**, doi:10.1103/PhysRevB.92.075310 (2015).

71. Clark, S. & Robertson, J. Band gap and Schottky barrier heights of multiferroic $BiFeO_3$. *Applied physics letters* **90**, 132903 (2007).

72. Palai, R. *et al.* βphase andγ−βmetal-insulator transition in multiferroic$BiFeO_3$. *Physical Review B* **77**, 014110, doi:10.1103/PhysRevB.77.014110 (2008).

73. Pisarev, R. V., Moskvin, A. S., Kalashnikova, A. M. & Rasing, T. Charge transfer transitions in multiferroic $BiFeO_3$ and related ferrite insulators. *Physical Review B* **79**, doi:10.1103/PhysRevB.79.235128 (2009).

74. Rivera, J.-P. & Schmid, H. On the birefringence of magnetoelectric $BiFeO_3$. *Ferroelectrics* **204**, 23-33 (1997).

75. Tabares-muñoz, C., Rivera, J.-P. & Schmid, H. Ferroelectric domains, birefringence and absorption of single crystals of $BiFeO_3$. *Ferroelectrics* **55**, 235-238 (1984).

76. Choi, S. G. *et al.* Optical anisotropy and charge-transfer transition energies in $BiFeO_3$ from 1.0 to 5.5 eV. *Physical Review B* **83**, doi:10.1103/PhysRevB.83.100101 (2011).

77. Dong, H., Liu, H. & Wang, S. Optical anisotropy and blue-shift phenomenon in tetragonal $BiFeO_3$. *Journal of Physics D: Applied Physics* **46**, doi:10.1088/0022-3727/46/13/135102 (2013).

78. Würfel, P. W., U. *Physics of Solar Cells From Basic Principles to Advanced Concepts*. (Wiley-VCH, 2016).

79. Böer, K. W. *Handbook of the Physics of Thin-Film Solar Cells*. (2013).

80. Sze, S. & Ng, K. *Physics of semiconductor devices*. (John Wiley & Sons, Inc., Hoboken, New Jersey, 2006).

81. Wang, L. *et al.* Ferroelectric $BiFeO_3$ as an Oxide Dye in Highly Tunable Mesoporous All-Oxide Photovoltaic Heterojunctions. *Small* **13**, 1602355, doi:https://doi.org/10.1002/smll.201602355 (2017).

82. Sze, S. M., Li, Y. & Ng, K. K. *Physics of semiconductor devices*. (John wiley & sons, 2021).

83. Glass, A. M., Linde, D. v. d. & Negran, T. J. High-voltage bulk photovoltaic effect and the photorefractive process in $LiNbO_3$. *Applied Physics Letters* **25**, 233-235, doi:10.1063/1.1655453 (1974).

84. Chynoweth, A. Surface space-charge layers in barium titanate. *Physical Review* **102**, 705 (1956).

85. Chen, F. S. Optically Induced Change of Refractive Indices in $LiNbO_3$ and $LiTaO_3$. *Journal of Applied Physics* **40**, 3389-3396, doi:10.1063/1.1658195 (1969).

86. Glass, A. M., von der Linde, D., Auston, D. H. & Negran, T. J. Excited state polarization, bulk photovoltaic effect and the photorefractive effect in electrically polarized media. *Journal of Electronic Materials* **4**, 915-943, doi:10.1007/BF02660180 (1975).

87. Gu, Z. *et al.* Mesoscopic Free Path of Nonthermalized Photogenerated Carriers in a Ferroelectric Insulator. *Phys Rev Lett* **118**, 096601, doi:10.1103/PhysRevLett.118.096601 (2017).

88. Young, S. M., Zheng, F. & Rappe, A. M. First-principles calculation of the bulk photovoltaic effect in bismuth ferrite. *Physical review letters* **109**, 236601 (2012).

89. Tan, L. Z. *et al.* Shift current bulk photovoltaic effect in polar materials—hybrid and oxide perovskites and beyond. *Npj Computational Materials* **2**, 1-12 (2016).

90. von Baltz, R. & Kraut, W. Theory of the bulk photovoltaic effect in pure crystals. *Physical Review B* **23**, 5590 (1981).

91. Sturman, B. I. & Fridkin, V. M. *The photovoltaic and photorefractive effects in noncentrosymmetric materials*. (Gordon and Breach Science Publishers, 1992).

92. Spanier, J. E. *et al.* Power conversion efficiency exceeding the Shockley–Queisser limit in a ferroelectric insulator. *Nature Photonics* **10**, 611-616, doi:10.1038/nphoton.2016.143 (2016).

93. Yuan, Y., Xiao, Z., Yang, B. & Huang, J. Arising applications of ferroelectric materials in photovoltaic devices. *Journal of Materials chemistry A* **2**, 6027-6041 (2014).

94. Fridkin, V. M. & Popov, B. Anomalous photovoltaic effect in ferroelectrics. *Soviet Physics Uspekhi* **21**, 981 (1978).

95. Fridkin, V. M. *Photoferroelectrics*. (Springer Berlin Heidelberg, 2012).

96. Koch, W., Munser, R., Ruppel, W. & Würfel, P. Anomalous photovoltage in $BaTiO_3$. *Ferroelectrics* **13**, 305-307 (1976).

97. Fradkin, V. & Magomadov, R. Anomalous photovoltaic effect in $LiNbO_3$: Fe in polarized light. *JETP Letters* **30**, 686-688 (1979).

98. Festl, H., Hertel, P., Krätzig, E. & Von Baltz, R. Investigations of the photovoltaic tensor in doped $LiNbO_3$. *physica status solidi (b)* **113**, 157-164 (1982).

99. Choi, T., Lee, S., Choi, Y. J., Kiryukhin, V. & Cheong, S.-W. Switchable ferroelectric diode and photovoltaic effect in BiFeO3. *Science* **324**, 63-66 (2009).

100. Matsuo, H., Noguchi, Y. & Miyayama, M. Gap-state engineering of visible-light-active ferroelectrics for photovoltaic applications. *Nature communications* **8**, 1-8 (2017).

101. Ji, W., Yao, K. & Liang, Y. C. Evidence of bulk photovoltaic effect and large tensor coefficient in ferroelectric $BiFeO_3$ thin films. *Physical Review B* **84**, 094115 (2011).

102. Bhatnagar, A., Roy Chaudhuri, A., Heon Kim, Y., Hesse, D. & Alexe, M. Role of domain walls in the abnormal photovoltaic effect in $BiFeO_3$. *Nature Communications* **4**, doi:10.1038/ncomms3835 (2013).

103. Ming-MinYang, Zheng-DongLuo, Kim, D. J. & Alexe, M. Bulk photovoltaic effect in monodomain $BiFeO_3$ thin films. *Applied Physics Letters* **110**, 183902, doi:10.1063/1.4983032 (2017).

104. Gunter, P. & Micheron, F. Photorefractive effects and photocurrents in KNbO3: Fe. *Ferroelectrics* **18**, 27-38 (1978).

105. Fridkin, V., Popov, B. & Ionov, P. Temperature and spectral dependence of the photovoltaic current in ferroelectrics. *Ferroelectrics* **18**, 165-168 (1978).

106. Ohi, K., Takeda, I. & Ohata, Y. Photoconductivity of KTaO3 crystals. *Izvestiya Akademii Nauk SSSR, Seriya Fizicheskaya* **41**, 804-810 (1977).

107. Ruppel, W., Von Baltz, R. & Wurfel, P. The origin of the photo-emf in ferroelectric and non-ferroelectric materials. *Ferroelectrics* **43**, 109-123 (1982).

108. Yang, M., Bhatnagar, A. & Alexe, M. Electronic origin and tailoring of photovoltaic effect in $BiFeO_3$ single crystals. *Advanced Electronic Materials* **1**, 1500139 (2015).

109. Alexe, M. & Hesse, D. Tip-enhanced photovoltaic effects in bismuth ferrite. *Nature communications* **2**, 1-5 (2011).

110. Yang, S. Y. *et al.* Above-bandgap voltages from ferroelectric photovoltaic devices. *Nat Nanotechnol* **5**, 143-147, doi:10.1038/nnano.2009.451 (2010).

111. Johann, F., Morelli, A. & Vrejoiu, I. Stability of 71 stripe domains in epitaxial BiFeO3 films upon repeated electrical switching. *physica status solidi (b)* **249**, 2278-2286 (2012).

112. Seidel, J. *et al.* Efficient photovoltaic current generation at ferroelectric domain walls. *Phys Rev Lett* **107**, 126805, doi:10.1103/PhysRevLett.107.126805 (2011).

113. Alexe, M. Local mapping of generation and recombination lifetime in $BiFeO_3$ single crystals by scanning probe photoinduced transient spectroscopy. *Nano Lett* **12**, 2193-2198, doi:10.1021/nl300618e (2012).

114. Yang, M. M., Bhatnagar, A., Luo, Z. D. & Alexe, M. Enhancement of Local Photovoltaic Current at Ferroelectric Domain Walls in $BiFeO_3$. *Sci Rep* **7**, 43070, doi:10.1038/srep43070 (2017).

115. Yang, Y. S. *et al.* Schottky barrier effects in the photocurrent of sol–gel derived lead zirconate titanate thin film capacitors. *Applied Physics Letters* **76**, 774-776, doi:10.1063/1.125891 (2000).

116. Pintilie, L., Vrejoiu, I., Le Rhun, G. & Alexe, M. Short-circuit photocurrent in epitaxial lead zirconate-titanate thin films. *Journal of Applied Physics* **101**, doi:10.1063/1.2560217 (2007).

117. Tan, Z. *et al.* Thinning ferroelectric films for high-efficiency photovoltaics based on the Schottky barrier effect. *NPG Asia Materials* **11**, doi:10.1038/s41427-019-0120-3 (2019).

118. Qin, M., Yao, K. & Liang, Y. C. High efficient photovoltaics in nanoscaled ferroelectric thin films. *Applied Physics Letters* **93**, doi:10.1063/1.2990754 (2008).

119. Qin, M., Yao, K. & Liang, Y. C. Photovoltaic mechanisms in ferroelectric thin films with the effects of the electrodes and interfaces. *Applied Physics Letters* **95**, doi:10.1063/1.3182824 (2009).

120. Gao, R. L. *et al.* Oxygen vacancies induced switchable and nonswitchable photovoltaic effects in $Ag/Bi_{0.9}La_{0.1}FeO_3/La_{0.7}Sr_{0.3}MnO_3$ sandwiched capacitors. *Applied Physics Letters* **104**, doi:10.1063/1.4862793 (2014).

121. Matsuo, H., Kitanaka, Y., Inoue, R., Noguchi, Y. & Miyayama, M. Cooperative effect of oxygen-vacancy-rich layer and ferroelectric polarization on photovoltaic properties in $BiFeO_3$ thin film capacitors. *Applied Physics Letters* **108**, doi:10.1063/1.4940374 (2016).

122. Zenkevich, A. *et al.* Giant bulk photovoltaic effect in thin ferroelectric $BaTiO_3$ films. *Physical Review B* **90**, doi:10.1103/PhysRevB.90.161409 (2014).

123. Astafiev, S. B., Fridkin, V. M. & Lazarev, V. G. The influence of the magnetic field on the linear bulk photovoltaic current in piezoelectric semiconductor GaP. *Ferroelectrics* **80**, 251-254, doi:10.1080/00150198808223306 (1988).

124. Yang, S. Y. *et al.* Photovoltaic effects in $BiFeO_3$. *Applied Physics Letters* **95**, doi:10.1063/1.3204695 (2009).

125. Ji, W., Yao, K. & Liang, Y. C. Bulk photovoltaic effect at visible wavelength in epitaxial ferroelectric $BiFeO_3$ thin films. *Adv Mater* **22**, 1763-1766, doi:10.1002/adma.200902985 (2010).

126. Ji, W., Yao, K. & Liang, Y. C. Evidence of bulk photovoltaic effect and large tensor coefficient in ferroelectric $BiFeO_3$ thin films. *Physical Review B* **84**, doi:10.1103/PhysRevB.84.094115 (2011).

127. Guo, R., You, L., Chen, L., Wu, D. & Wang, J. Photovoltaic property of $BiFeO_3$ thin films with 109° domains. *Applied Physics Letters* **99**, doi:10.1063/1.3641905 (2011).

128. Lee, D. *et al.* Polarity control of carrier injection at ferroelectric/metal interfaces for electrically switchable diode and photovoltaic effects. *Physical Review B* **84**, doi:10.1103/PhysRevB.84.125305 (2011).

129. Zhou, Y. *et al.* Photovoltaic property of domain engineered epitaxial $BiFeO_3$ films. *Applied Physics Letters* **105**, doi:10.1063/1.4905000 (2014).

130. Nechache, R. *et al.* Bandgap tuning of multiferroic oxide solar cells. *Nature Photonics* **9**, 61-67, doi:10.1038/nphoton.2014.255 (2014).

131. Kim, D. J. & Alexe, M. Bulk photovoltaic effect in monodomain $BiFeO_3$ thin films. *Applied Physics Letters* **110**, doi:10.1063/1.4983032 (2017).

132. Matsuo, H., Noguchi, Y. & Miyayama, M. Gap-state engineering of visible-light-active ferroelectrics for photovoltaic applications. *Nat Commun* **8**, 207, doi:10.1038/s41467-017-00245-9 (2017).

133. Mai, H. *et al.* High performance bulk photovoltaics in narrow-bandgap centrosymmetric ultrathin films. *Materials Horizons* **7**, 898-904, doi:10.1039/c9mh01744e (2020).

Chapter 3

Experimental Methodology

The working principles of the experimental techniques used to accomplish this dissertation are discussed in this chapter. Firstly, the rationale of selecting the fabrication and characterization methods is elucidated. Second, an overview of pulsed laser deposition technique as the main thin film deposition technique exploited here is presented. This is followed by the description of the structural and functional characterization methods to probe the devices under test.

3.1 Rationale for selection of materials and techniques

Ferroelectric materials hold a great promise for the solar cell applications. They are a class of materials that possesses a spontaneous electric polarization originating from the distortion of its crystal lattice in a specific fashion. In addition to the ferroelectric property, ferroelectrics exhibit piezoelectricity and pyroelectricity which make them interesting from the fundamental and application perspectives.[1-3] More intriguingly, ferroelectrics manifest themselves as a noncentrosymmetric crystals by exhibiting photovoltaic effects. Indeed, the origin of such photovoltaic behavior is still under debate. In other words, opinion on the origin is divided between whether the phenomenon stems from the crystal bulk or interface effects.[4-7]

In this work, the origin of the photovoltaic effect in ferroelectric thin films is investigated. Therefore, high quality thin films in terms of ferroelectric and optical properties are of great importance for this research. For these reasons, the prototypical ferroelectric bismuth ferrite ($BiFeO_3$) is chosen as a photoactive material to test our hypothesis. $BiFeO_3$ crystallizes in the rhombohedral space group R3c which develops a strong ferroelectric polarization (of 100 C/cm^2) towards $<111>_{pc}$.[8-10] On the other hand, it is well-stablished that $BiFeO_3$ optical structure is characterized by a relatively small bandgap (<2.75 eV).[11-13] Thus and owing to its unique combined ferroelectric and optical properties, $BiFeO_3$ is richer material system over the other ferroelectrics (e.g. $LiNbO_3$[14], $BaTiO_3$[15] and $Pb(Zr,Ti)O_3$[16]) to study the ferroelectric photovoltaic effect.

Leakage current is the enemy of ferroelectricity and should be avoided in order to saturate the ferroelectric P-E loops. Leakage current is associated with the material defects or the fair interfaces which might also limit the ferroelectric photovoltaic effects. Hence, *pulsed laser deposition* (PLD) technique is adopted in this dissertation in order to grow *epitaxial* heterostructures with high quality bulk and interfaces. This involves the growth of single crystalline thin films that resembles the substrate's crystal lattice. Also, PLD is advantageous over the other oxide growth techniques such as sputtering in that it exhibits higher deposition rates with improved crystal quality.[17] Following the material preparation,

they are characterized for their crystal structure, morphology, ferroelectric property and photovoltaic performance.

Prior to the functional characterization, the grown films must be ensured they are in the right crystal phase and possesses smooth morphology. Thus, x-ray diffraction method is employed to examine the crystal phase and quality. More particularly, the high-resolution X-ray diffraction, or HRXRD, is used in this dissertation which not only probes the crystal phase and quality but also can determine the structural domains comprising the thin film. Subsequently, the atomic force microscopy (AFM) is used to image the film surface on microscale.

Testing the ferroelectric property is meant to ensure that the thin films exhibit a reversible spontaneous polarization. Locally, the piezoresponse force microscopy (PFM) is used to map the ferroelectric domain structure as well as test the polarization flipping on a microscopic scale. A macroscopic characterization technique, namely the polarization-electric field loop tester, is also needed. In fact, a combined micro- and macroscopic characterization of the ferroelectricity of the grown thin films provides a picture.

Ultimately, measuring the photovoltaic property of the $BiFeO_3$ thin films is the main objective of this work. For this, sourcemeter are exploited to probe the electrical properties of the devices in dark and under illumination. In this work, white light and monochromatic laser sources are employed to measure the devices under test.

3.2 Device preparation

Photovoltaic cells based on the single-crystalline $BiFeO_3$ thin films are synthesized by means of pulsed laser deposition technique. In order to measure out-of-plane photovoltaic responses, $BiFeO_3$ layer is sandwiched between bottom and top electrodes. Hence, the device is prepared by the following sequence; initially, a metallic complex oxide is grown on top of a single crystal substrate to serve as a bottom electrode. Secondly, $BiFeO_3$ film is being deposited on the bottom electrode. At last, an array of elemental electrodes is on $BiFeO_3$ film sputtered at room temperature. This section introduces the working principles

of the deposition techniques used in this dissertation, i.e., pulsed laser deposition and DC sputtering techniques.

3.2.1 Pulsed laser deposition (PLD)

Pulsed laser deposition is a tool which is used broadly in materials science to grow wide range of materials, particularly complex oxides. It was developed during the 1980s which efficiently produced high quality cuprate thin films that is high-T_c superconductor.[18] It is listed under the physical vapor deposition methods which relies on the evaporation of a condensed phase material source. In PLD, a strong laser source is employed for the vaporization of the solid material. Subsequently, the evaporated material travels towards a substrate surface before being condensed and nucleating in the form of a solid coating the substrate.[17,19,20]

3.2.1.1 Working principle

In typical PLD process, as depicted in Figure 3.1, a high-power UV pulsed laser hits the surface of a bulky ceramic material - called *target* - in vacuum or oxidizing environment. When the laser energy is of enough energy density, or *fluence*, the energy transfers to the target surface causing surface boiling and hence vaporizing the surface material. The ionized material comes out in the form of a luminous *plume*. For inorganic materials, the laser is chosen such that its wavelength lies in the UV region and has pulsed nature to be strongly absorbed in small volume of the target. It is worth noting that the pulsed mode induces the so-called “congruent” evaporation which assists to preserve the stoichiometry of the target to large extent. The parameters of the laser source used in the ablation process affect the formation of the plasma plume emitted from the surface of the target. This includes the energy density F, pulse width τ, wavelength λ, and laser repetition rate R.[21,22]

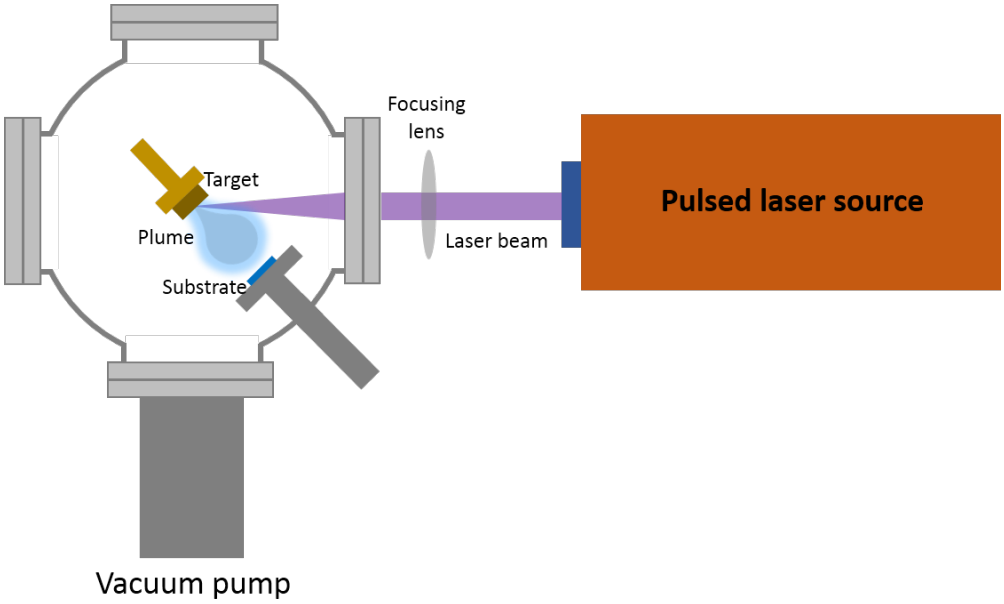

Figure 3.1: The operating principle of the pulsed laser deposition (PLD). The laser beam (yellowish) impinges the rotating target ablating ions from its surface. The ablated material (Purple) is released towards the substrate surface. Finally, the thin film is formed on top of the substrate.

The emitted plasma from the ablation process consists of atomic, diatomic and other species. Interestingly, the constituents of the plasma plume have energy as high as 100 eV which are being attenuated by the reactive background gas.[21] Such reactive gas is introduced in the growth environment to compensate for the loss of anions during the deposition, e.g. O_2 for oxides and N_2 for nitrides. The attenuated species have energies ranging from 1 eV to 5 eV depending on the background pressure. Finally, the energetic atoms and ions arrive a heated substrate surface before exhibiting a number of complicated processes following the mass transport laws.[21,22]

Once the plume species reach the substrate, several kinetic processes occur, namely, the *adsorption* of the particles (called adatom) on the substrate surface which in turn diffuse to other locations. Afterwards, they might be incorporated into the crystal lattice of the substrate or the growing layer and subsequently begin to *nucleate* (to nucleus). There are unwanted processes that may occur such as the implantation of highly energetic ions into the substrate. Moreover, when the grown material includes volatile species, it is most probable to evaporate from the substrate surface deviating the film from the correct

stoichiometry.[23] This is exemplified by the Bi ion in $BiFeO_3$ which is grown in this thesis which delayed its renaissance for several decades before being stabilized during PLD process in 2003.[24] The different possible processes are schematically illustrated in Figure 3.2.

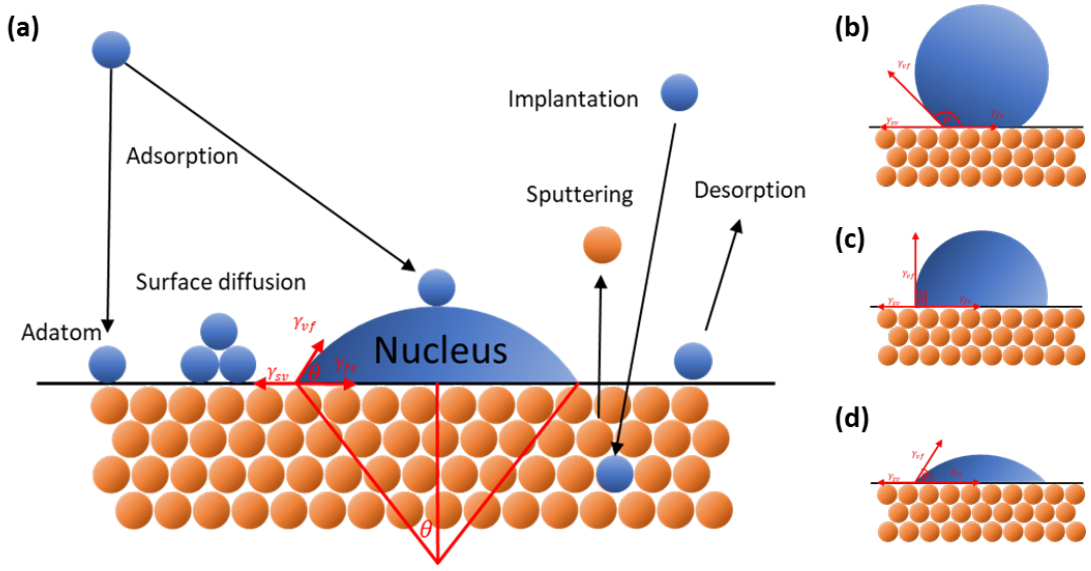

Figure 3.2: Nucleation of vapor species on single crystal substrate. **(a)** Schematic representation of the atomic processes involved in the film growth. Orange circles array represents the substrate while the blue color indicates foreigner species. However, the nucleus shape depends on the contact angle with the substrate material resulting in **(b)** Non-wetting, **(c)** incomplete wetting and **(d)** Good wetting phenomena. Inspired by Ref. 26.

The diffusion rate of an adatom on the surface of substrate is given by the equation[19]:

$$D_s = v\alpha^2 e^{-\frac{E_A}{KT}} \tag{3.14}$$

Where D_s is the surface diffusion coefficient, E_A is the activation energy, T is the temperature, and α is characteristic jump distance. Moreover, the distance in which the adatoms diffuse on the surface is determined by the surface diffusion distance l_d and is given by[19]:

$$l_d = \sqrt{D_s \tau_a} \tag{3.15}$$

where τ_a is the mean time of the adatom before it becomes trapped at a step or edge. In pulsed laser deposition experiment, controlling the two kinetic parameters given by equations (3.1) and (3.2) is handled by a combination of growth conditions altogether, i.e.,

laser energy density, the background gas pressure and the substrate temperature. Other parameters such as the target-substrate distance and laser repetition rate also. However, different elements exhibit different diffusion lengths and hence defect formation is of high possibility to occur when growing multicomponent substances.[25] Eventually, the deposited species proceed to build up to form thin film in an "epitaxial" fashion.

3.2.1.2 Concept of epitaxy

Epitaxy refers to the growth of single crystalline thin films, or epilayer, on top of crystalline substrates. The grown epitaxial film imitates the crystal structure of the substrate. The origin of the word "Epitaxy" is the Greek syllables; "epi" and "taxis" that mean "in ordered manner". As plotted in Figure 3.3, there are two types of epitaxy: *homoepitaxy* and *heteroepitaxy.* Homoepitaxy refers to the growth of thin films of chemical composition identical to that of the substrates such as the growth of Si on top of single crystal Si wafer.

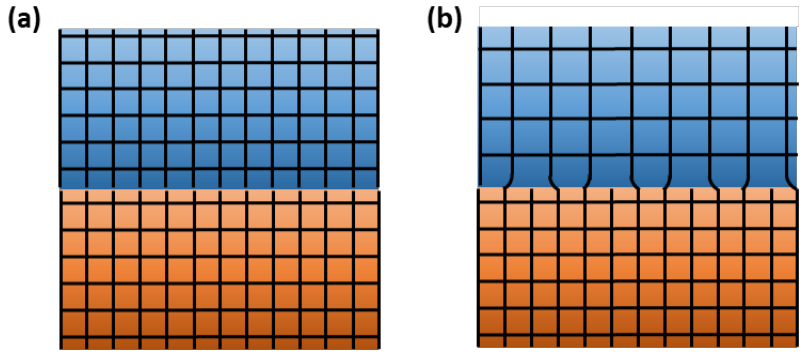

Figure 3.3: Types of growth of epitaxial thin films (blue layer) on bulky substrate (orange colored base). **(a)** Homoepitaxy where the grown thin film is identical to the substrate material yielding a coherent growth. **(b)** Heteroepitaxy. In this kind of growth, the film chemical composition differs from the substrate. The mismatch in crystal lattice parameters between the film and substrate substances induces strain effects at the film side.

Furthermore, homoepitaxial film is grown via the homogeneous nucleation, i.e., direct condensation of the vapor and depends only on the interfacial energy between the nucleus and the substrate. However, heteroepitaxy corresponds to the growth of a thin film that is dissimilar to the substrate in terms of chemistry.[26]

On the other hand, heterogeneous nucleation initiates the heteroepitaxy process. Here, the nucleation depends on the constituents of the vapor in addition to the interface energy. More importantly, the defects on the substrate surface plays a critical role in the nucleation rate. In fact, nucleation favors atomic defect sites where building maximum number of chemical bonds is guaranteed. There are three fundamental heteroepitaxial growth modes which are determined by the thermodynamic and kinetic aspects of the growth process. These are the Volmer-Weber (VW), Frank-van der Merwe (FM) and Stranski-Krastanove (SK) growth modes. However, growth mechanisms can be explained by simply considering the surface and interfacial energies of the substrate and epitaxial layer.

Modes of heteroepitaxial growth

The epitaxial growth modes can be described in terms of Young's equation[27]:

$$\gamma_s = \gamma_i + \gamma_e cos\theta \tag{3.16}$$

Where γ_s and γ_e are the substrate and epitaxial material surface energies, respectively. Additionally, γ_i is interfacial energy between substrate and epitaxial layer while θ refers to the contact angle between them. According to equation (3.3), for $\gamma_e > \gamma_s$, the deposited material partially wets the substrate surface resulting in a 3D growth (or island mode) as plotted in Figure 3.4 (a). This growth mode is observed when metals are grown on oxide substrates and is called Volmer-Veber mode. On the other hand, if $\gamma_e < \gamma_s$, the deposit wets the substrate, and a layer-by-layer growth will be achieved such as the situation depicted in Figure 3.4 (b). An important example of this is the semiconductors heteroepitaxy. However, if a relatively large lattice mismatch exists between the epitaxial film and the substrate while $\gamma_e < \gamma_s$ is still fulfilled, the growth may switch to island mode after growing several layers. This is to release the strain energy by relaxation as demonstrated in Figure 3.4 (c). This type of growth is observed in several metal-metal and metal-semiconductor heterostructures.[27]

Moreover, in case of the substrate morphology has terraces or steps, additional growth mode comes to the picture, the step-flow growth mode as depicted in figure 3.4 (d). In this mode, and when the atoms have large diffusion length, they diffuse along the steps until

they begin to nucleate at the step edge. In fact, the step-like morphology of the substrate is still visible after the nucleation as illustrated in figure 3.4 (d). An example demonstrating such growth mode is the heteroepitaxial growth $BiFeO_3$ on $SrRuO_3$. $BiFeO_3$ species tend to diffuse faster on the SrO termination layers which can be achieved by growing $SrRuO_3$ on $SrTiO_3$ in which Ru evaporates from the outermost layer leaving SrO sheets behind.[20] The result is a smooth $BiFeO_3$ morphology imitating the surface of $SrRuO_3$ film.[28,29]

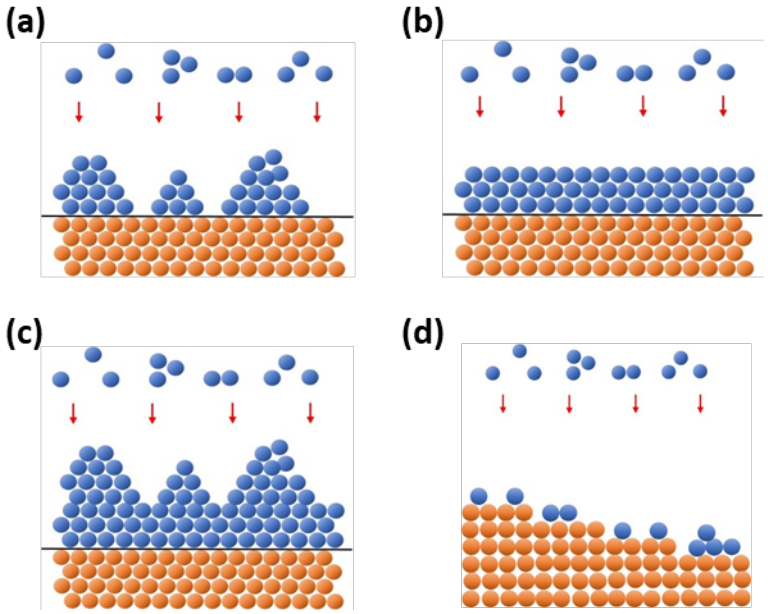

Figure 3.4: Basic modes of epitaxial thin films growth. **(a)** Volmer-Veber or the island mode. **(b)** Frank-Van der Merwe or the layer-by-layer mode. **(c)** Stranski-Krastanov or the layer plus island mode. **(d)** Step-flow growth mode. Inspired by Ref. 26.

In this research work, epitaxial bismuth ferrite (lattice constant a_{pc}=3.96 Å) films are grown on single crystal strontium titanate (a= 3.905 Å) substrates. $SrTiO_3$ is selected because its lattice parameter fits that of $BiFeO_3$ (though a small in-plane compressive strain is induced). Also, it is a wide band insulator exhibiting bandgap of 3.1 eV.[30,31] More specifically, (001)-oriented $SrTiO_3$ single crystal with 4° miscut towards $[110]_{pc}$ are exploited in this dissertation to promote single ferroelectric domain structure in the $BiFeO_3$ film.[32]

3.2.1.3 Experimental procedure

In this dissertation, the pulsed laser deposition (PLD-450) from SKY Technology Development Co., Ltd. is used to grow epitaxial films. In this setup, a spherical vacuum sputtering chamber is connected to external pumping system to assist reaching low pressures. The pumping system is composed of two mechanical and turbo molecular pumps connected in series. Inside the chamber, there exist rotatable target and sample holders, pressure gauges. To ablate the target, a KrF excimer laser source (COMPex 205) is employed. It emits UV pulsed laser of wavelength of 248 nm (~ 5 eV) and pulse width of 20 ns. The laser beam is focused by means of a lens to focal point laying on the target surface. Hence, one can tailor the laser energy density by adjusting the focal point. A typical PLD experiment is performed in the following sequence.

First of all, the substrates are cleaned prior to the film growth by pulsed laser deposition (PLD). The substrates are immersed in ethanol, acetone and finally ethanol (each for 5 min) before being sonicated. Afterwards, the substrate is blown by clean nitrogen gas to remove any residual and dry the surface. It should be noted that the polished surface has to face up to avoid scratching by the beaker's bottom. Then, the substrate is attached to a metallic sample holder by means of silver paste. Heating of the substrate is executed by a resistive coil placed underneath the sample holder while its temperature is measured by a thermocouple.

On the other hand, a dense ceramic $Bi_{1.2}FeO_3$ target is exploited in this dissertation. The reason a Bi-excess target is used is to compensate for the Bi loss during the laser ablation process. The target surface is polished prior to mounting to the PLD chamber. The target-to-sample distance is kept at 5 cm. Subsequently, the growth chamber is pumped out to pressure ~ 10^{-5} Pa. Afterwards, a dynamic O_2 gas is inserted into the chamber which is controlled through the mass flow controllers. Alongside with this, the substrate is gradually heated up to the growth temperature.

Finally, the laser hits the target surface producing the plume. The growth is optimized by tuning the deposition conditions such as the substrate temperature T_s, O_2 pressure P_{O2}, laser fluence F and repetition rate R. The growth conditions used in this thesis is presented in table 3.1.

Table 3.2: Growth parameters adopted in this dissertation.

	Substrate temperature [°C]	Oxygen pressure [mtorr]	Repetition rate [Hz]	Fluence [J/cm^2]	Thickness [nm]
$BiFeO_3$	630-650[a)]	50	10	1.2	38-500
$Bi_{1-x}La_xFeO_3$	640	50	10	1.2	120
$La_{0.7}Sr_{0.3}MnO_3$	800	200	3	2	10

a) depending on the film thickness.

3.3 Structural characterization

The functional properties of the epitaxial thin films are correlated to its structural properties. This implies that probing the crystallography and surface morphology of the epitaxial films is of high importance prior to integrating them into testing devices. Crystal structural properties of $BiFeO_3$ thin films in this dissertation are revealed by high-resolution x-ray diffraction. On the other hand, atomic force and piezoresponse microscopy are employed to image surface and ferroelectric domain structure of the films. In this section, the working principles of high-resolution x-ray diffraction (HRXRD), atomic force microscope (AFM) and piezoresponse microscopy (PFM) are described.

3.3.1 X-ray diffraction: high-resolution geometry

X-rays are those radiation lying within the wavelength range of 0.01 - 10 nm in the electromagnetic spectrum. Consequently, x-rays with photon energies ranging from 3 to 8

KeV are comparable to the crystal lattice parameters. Hence, x-ray is a powerful probe to characterize the crystallinity and the chemical composition of materials. This subsection briefly introduces the high-resolution x-ray diffraction (HRXRD) which is used to probe the crystallographic properties of epitaxial thin films.

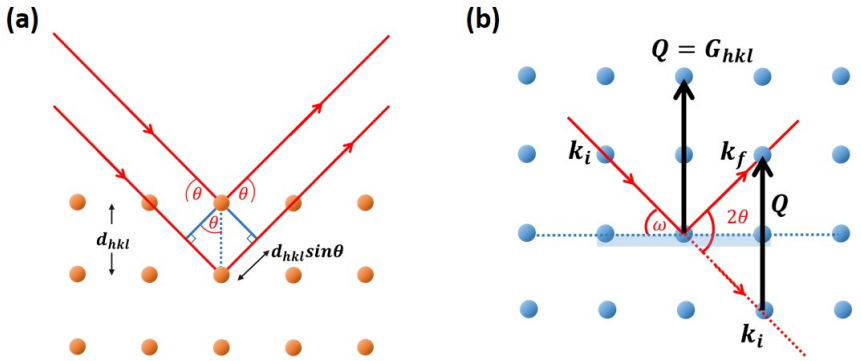

Figure 3.5: Concept of x-ray diffraction (XRD). **(a)** XRD in real space where the real crystal exists and d_{hkl} is the separation between the planes. Bragg's law is fulfilled when the path difference between the incident and scattered beams ($2d_{hkl}sin\theta$) is an integral number of the x-rays wavelength. **(b)** XRD in reciprocal space in which each blue ball corresponds to family of parallel crystallographic planes. Here, G_{hkl} is the reciprocal lattice vector and is defined by ($|G_{hkl}| = 2\pi/d_{hkl}$).

When x-rays are incident on an ordered array of atoms, they scatter coherently and elastically, or diffract. *X-ray diffraction* (XRD) involves the interference of the scattered monochromatic X-rays from crystalline materials giving rise to dark and bright fringes (or intensity peaks). The orange balls in Figure 3.5 (a) represent the crystal atoms with spacing between the atomic planes d_{hkl}. The x-ray diffraction condition is defined by Bragg's law stating that[33]:

$$2d_{hkl}sin\theta = n\lambda \qquad (3.17)$$

With λ is the x-ray wavelength, θ is incidence angle and n is the diffraction order. Hence, the crystal structure of the material can be analyzed. The mathematical equation states that a constructive interference occurs when the path difference between the incident and reflected beams equals to multiple number of the X-ray wavelength.[33]

However, describing x-ray diffraction in terms of scattering vector coordinates plotted in reciprocal space is more convenient. In reciprocal space, every point represents a family of crystallographic planes, e.g., <001>. Figure 3.5 (b) depicts the scattering triangle where k_i represents the incident beam wave vector, k_f is the diffracted wave and Q is the scattering vector and given by[33]:

$$\vec{Q} = \vec{k}_i - \vec{k}_f \tag{3.18}$$

Herein, ω represents the incidence angle while 2θ is the angle between the incident and diffracted beams. In this, the diffraction takes place if Laue's condition is fulfilled, i.e., whenever the scattering vector coincides on the reciprocal lattice vector.[33]

Epitaxial thin films are defined as the single crystalline thin films grown on single crystal substrates. Hence, and due to the large penetration depth of x-rays, substrates usually contribute to the XRD pattern in addition to the thin film. Consequently, both thin film and substrate peaks overlap since they are of close lattice parameters. Therefore, a high-resolution x-ray diffractometer is required for the epitaxial films in order to resolve the superimposed peaks. In this setup, monochromators and analyzers are placed in the beam path which excludes the non-diffracted x-rays. This can be interpreted by differentiating Bragg equation yielding[34]:

$$\frac{\Delta d}{d} = \frac{\Delta \lambda}{\lambda} + \frac{\Delta \theta}{tan\theta} \tag{3.19}$$

Which implies that in order to obtain d_{hkl} precisely, a highly monochromatic beam ($\Delta\lambda/\lambda$ is minimized) and high-resolution detector (small $\Delta\theta$) are exploited. At the end, HRXRD probes the crystal quality of the epilayer compared to the substrate (Which is supposedly of perfect or close to perfect crystallinity).

In this research work, Bruker D8 Discover high-resolution x-ray diffraction technique is employed to characterize the epitaxial thin films. In this set-up, Cu-K_α x-ray radiation ($\lambda = 1.5406$ Å) hits the sample surface mounted on a goniometric stage. The stage is attached to Euler cradle and can be rotated, swung and moved in x-, y- and z-directions as shown in Figure 3.6 (a). Also, a 2-bounce Ge monochromator is sometimes used to improve the peaks resolution which unfortunately drops the intensity. The diffracted beam is then detected by LYNXEYE silicon strip detector. This detector can be switched between 1D and 0D modes according to the scan type.[34]

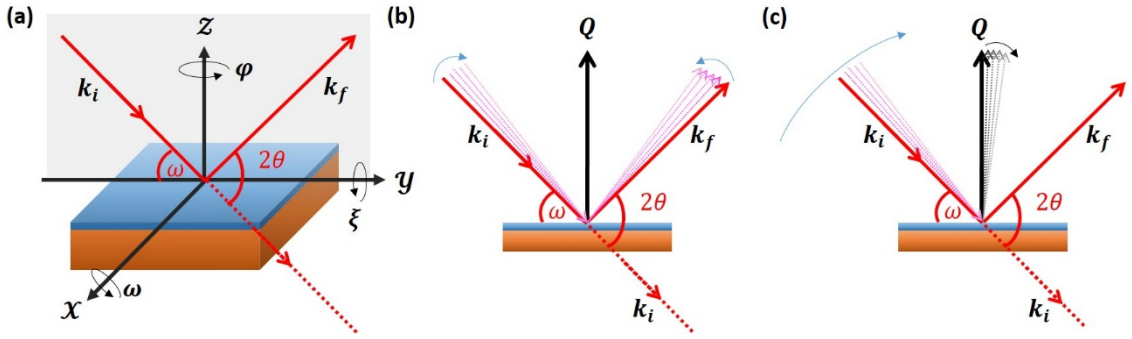

Figure 3.6: High-resolution x-ray diffraction on epilayer (blue)-substrate (orange). **(a)** Euler cradle. **(b)** Symmetric $2\theta - \omega$ scan. In this, the source and detector move simultaneously with $\omega = 2\theta/2$ maintaining the scattering vector Q direction fixed normal to the sample surface. Hence, structural information from the out-of-plane direction can be extracted. (c) Rocking curve scan. The source move while fixing the detector.

There are several types of scans that can be performed by HRXRD depending on the desired structural information. The symmetric 2θ-ω scan is meant to probe the structural information of out-of-plane direction, e.g. [001] in (001)-oriented films. In this scan, the scattering vector, Q, is kept normal to the surface plane during the measurement while the x-ray source and detector are simultaneously rotated. In addition, the diffraction angle 2θ is held double the incident angle ω while the detector and source move. Consequently, the out-of-plane parameter (c) of film can be calculated as well as the impurities if they have same orientation as the thin film. Also, the same scan configuration can be to measure asymmetric planes such as (113) planes in (001)-oriented thin films.[34]

In ω-scan, as shown in Figure 3.6 (c), the x-ray source moves while 2θ is maintained at constant value. Therefore, the scattering vector direction varies giving rise to rocking curve (Intensity versus θ). In this case, the symmetric rocking curve accounts for the lateral crystallite sizes, and thus the crystal quality. This can be evaluated by monitoring the broadening of the peak similar to the powder diffraction. Rocking curve is useful when it comes to the sample alignment prior to the actual measurements.[34]

To measure XRD, the sample is placed on the stage before aligned so that the desired crystallographic plane is normal to the Q vector to maximize the intensity. This can be handled by choosing the 2θ and ω corresponding to that plane. More importantly, $SrTiO_3$ substrates with 4° miscut along $[110]_{pc}$ direction are exploited here which are challenging to align. To handle this, miscut direction is first determined by AFM before going to XRD measurements.

3.3.2 Scanning probe microscopy

Scanning probe microscopy (SPM) refers to the powerful technique that employ a sharp tip attached to a soft cantilever to probe the surface of the materials. While the tip raster the material surface and interact with it, the cantilever responds by a bending or torsion. The reaction of the cantilever depends on the type of the interaction i.e., electrical, mechanical, chemical or magnetic. In this dissertation, the atomic force and piezoresponse force microscopes are used to characterize the topography and ferroelectric domain structure respectively.

3.3.2.1 Atomic force microscope (AFM)

The Atomic force microscope, or AFM, was first designed by Binning and coworkers in 1986.[10] Since then, it is widely used in the surface science fields. The concept of AFM is based on scanning a tip along the material surface while recording its interactions depending on the morphology. The interactions result in cantilever bending and torsions which is a measure of the artifacts of on the surface. The cantilever deflection is measured

by a laser beam reflected from the backside of the cantilever to a photodetector as shown in Figure 3.7 (a). Afterwards, the signal is sent to the feedback loop which in turn pass it to an actuator which keep the distance tip-surface distance constant.[35,36]

In order to detect the laser beam reflected from the cantilever backside, a four-segmented photodiode is used as depicted in Figure 3.7 (b) and (c). Any vertical deflections are measured by subtracting (C+D) from (A+B) voltages. On the other hand, the lateral deflections are detected as (A+C)-(B+D).

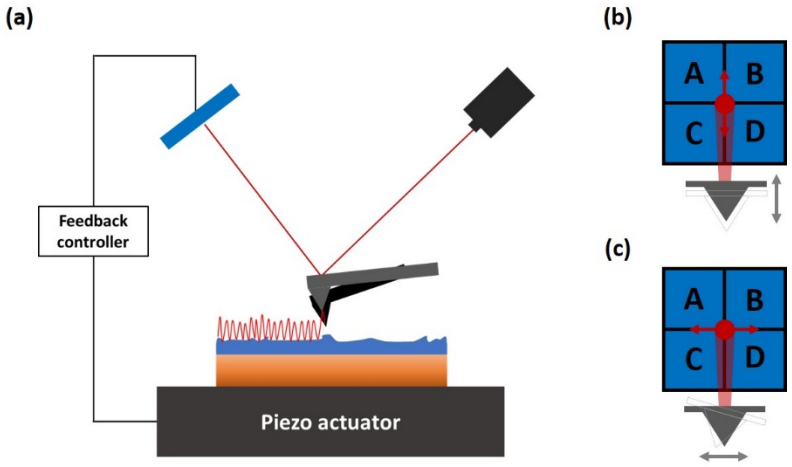

Figure 3.7: Working principle of atomic force microscope (AFM). **(a)** Setup of a typical AFM in the tapping mode. Tip attached to a vibrating cantilever that raster the surface of the sample. Cantilever deflections are detected by means of laser reflected off the back side of the cantilever to a 2D 4-segmented photodiode which are differentiated into vertical deflections **(b)** and lateral torsions **(c)**.

Atomic force microscope works in three different modes depending on the tip-surface distance. In *contact* mode, the tip is in physical contact with surface giving rise to repulsion force. If the tip is maintained far from the surface during the measurement leading to attractive force between them, it is called *non-contact* mode. The latter mode overcomes the possibility of tip spoiling in contact mode due to the physical contact with the surface. Lastly, the *tapping* mode in which the cantilever is set to oscillate with its resonance frequency. In this case, any oscillation damping due to either repulsive or attractive forces is measured and translated into topographical image.[35,36]

3.3.2.2 Piezoresponse force microscopy (PFM)

When it comes to the ferroelectric domain visualization and manipulation, a piezoresponse force microscope has to be employed. The converse piezoelectric effect in ferroelectrics is the basic principle of how piezoresponse force microscope (PFM) works. In this regard, an AC voltage $V_{ac}\cos(\omega t)$ is applied to the AFM tip in contact mode with ferroelectric material surface. Since the strain and applied electric field are coupled, the material responds by either contracting or expanding. These expansions and contractions are measured by the tip and converted into electrical signals to a lock-in amplifier. Consequently, the vertical and lateral responds from the sample can be acquired.

The sample surface deformation can thus be written as[37]:

$$d = d_o + Dcos(\omega t + \varphi)$$

where d_o is the equilibrium position, D is the amplitude, ω is signal frequency and φ is the phase difference. The amplitude of the signal reveals information about the piezoelectric coefficients of the sample. For instance, $\varphi = 180^o$ for domains with polarization component pointing upwards whereas downward-polarized areas result in $\varphi = 0^o$. This produces contrast in the PFM image as depicted in figure. It worth noting to mention that PFM can be used to measure either the out-of-plane (vertical PFM) or in-plane (lateral PFM) components of the polarization separately. Additionally, both measured images can be merged and reconstructed to produce a 3D PFM image.[37]

In $BiFeO_3$, the net polarization points towards the $[111]_{pc}$ direction with two components in $[001]_{pc}$ and $[110]_{pc}$ directions. As shown in figure, the out-of-plane PFM can detect the polarization component in $[001]_{pc}$ direction. To measure the in-plane PFM, one has to be careful with the cantilever direction. In case of cantilever aligned along $[010]_{pc}$, only projections along $[100]_{pc}$ and $[100]_{pc}$ can be measured. Similarly, only projections of $[010]_{pc}$ and $[010]_{pc}$ can be revealed if the cantilever set parallel to $[100]_{pc}$ direction. This work mostly aims at single ferroelectric domain thin films grown on $SrTiO_3$ substrates with miscut towards $[110]_{pc}$ direction. In measuring the lateral PFM, the cantilever is set parallel to $[-110]_{pc}$.

In this project, the commercial AFM (Asylum Research MFP-3D) is employed to measure topography and ferroelectric domain pattern. The same set-up is used for the PFM measurements. In PFM mode, an external lock-in amplifier is used to detect the deflection signals. Furthermore, the cantilevers were carefully chosen depending on the desired scan type. For instance, Pt/Ir coated silicon tips of resonance frequency 160 KHz and 320 KHz were used during the lateral and vertical PFM measurements, respectively. Additionally, the cantilever is driven by 1V ac voltage to vibrate with 10 KHz frequency while the bottom electrode is grounded. The color code of the lateral and vertical PFMs used in this dissertation is illustrated in figure 3.8.

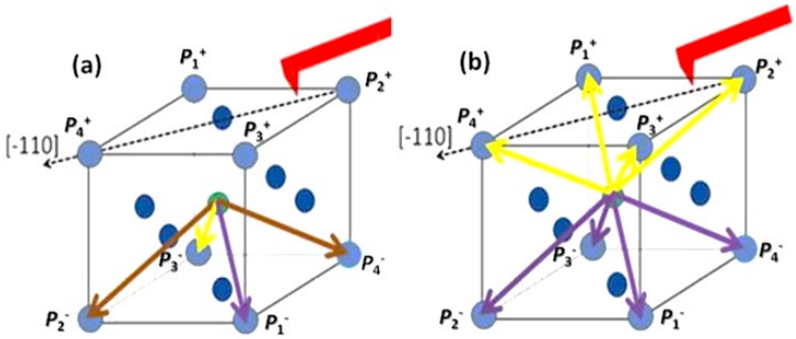

Figure 3.8: Color code of **(a)** IP PFM and **(b)** OOP PFM where the cantilever is set parallel to $[-110]_{pc}$ direction. Taken from Ref. 27.

3.4 Electrical characterization

The main aspect of this work is to measure the ferroelectric photovoltaic effect in $BiFeO_3$ thin films and its derivatives. This means that the ferroelectric properties of the films must be confirmed prior to measuring the photovoltaic properties. To handle this a ferroelectric tester and probe station are exploited to measure the polarization-electric field loops of the material. In addition, a source-meter is employed to measure the electrical and optoelectronic properties.

3.4.1 Ferroelectric measurements

Measuring the polarization-electric field hysteresis loop reveal the ferroelectric properties of ferroelectrics. These include the coercive field E_c and the remnant polarization P_r. Sawyer-Tower circuit is used to the ferroelectric properties of ferroelectrics.[38] In this circuit, a triangular wave voltage with frequency f is applied between the top and bottom electrodes of the sample. Simultaneously, the generated current due to charge motions is integrated over time. This current has contributions from charge displacement and leakage mechanisms. To reduce the leakage contribution, voltages at higher frequencies should be applied. In this work. PE hysteresis loops were measured by means of Precision LC, Radiant Technologies ferroelectric tester connected to a micromanipulator probe station.

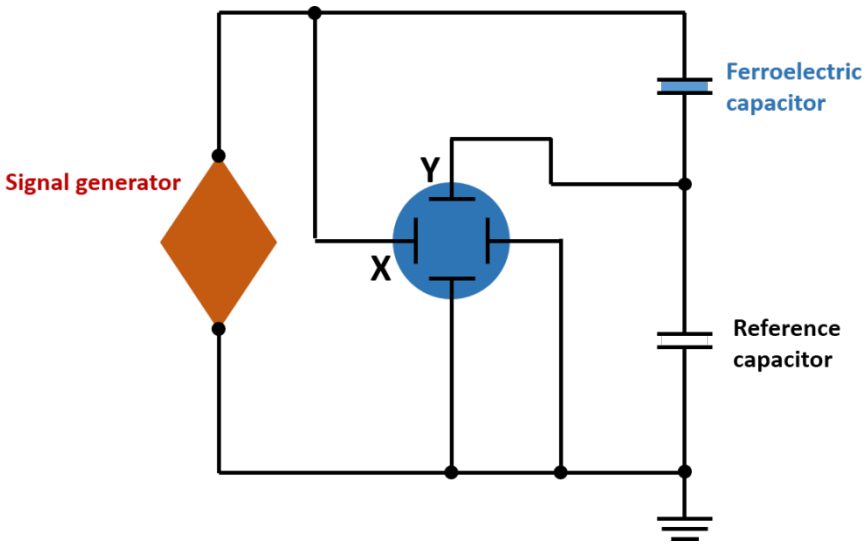

Figure 3.9: Sawyer-Tower circuit. It consists of two capacitors connected in series; the reference capacitor and the ferroelectric capacitor under test. A triangular wave voltage is applied to the sample. The total current due to charge motions is integrated over time. This current has contributions from charge displacement and leakage mechanisms. At the end, the remnant polarization and coercive field can be extracted.

3.4.2 Optoelectronic properties

This thesis is concerned with the understanding of the photovoltaic effects in vertical top electrode/$BiFeO_3$/bottom electrode heterostructures. For this purpose, the sample is connected out under optical microscope attached to the probe station. Further, the sample surface is illuminated by either white or monochromatic light sources. The white light is provided by a halogen lamp with spectrum shown in Figure 3.10 (a). Also, commercial monochromatic lasers of wavelengths 405 nm (purple) and 520 nm (green) are adopted. In order to study the interaction of polarized-light with $BiFeO_3$ samples, Glan-Laser calcite linear polarizer was placed in the optical path. The working wavelength spectrum of the polarizer is presented in Figure 3.10 (b). Photovoltaic responses were characterized by a 4140B, Hewlett Packard electrometer with white light illumination up to 100 mW/cm^2.

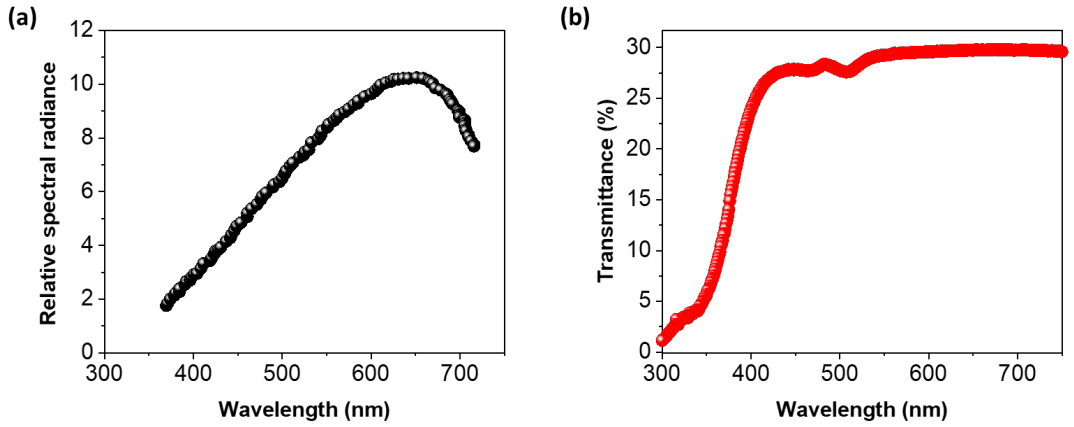

Figure 3.10: (a) Spectra of the halogen lamp used to provide white light to the sample surface. **(b)** Working wavelength range of the linear polarizer used in this thesis.

Reference

1. Uchino, K. *Ferroelectric Devices 2nd Edition*. (CRC Press, Inc., 2009).

2. Rabe, K. M. A., C. H.; Triscone, J. *Physics of Ferroelectrics*. (2007).

3. Lines, M. E. & Glass, A. M. *Principles and applications of ferroelectrics and related materials*. (Oxford university press, 2001).

4. Choi, T., Lee, S., Choi, Y. J., Kiryukhin, V. & Cheong, S.-W. Switchable ferroelectric diode and photovoltaic effect in $BiFeO_3$. *Science* **324**, 63-66 (2009).

5. Spanier, J. E. *et al.* Power conversion efficiency exceeding the Shockley–Queisser limit in a ferroelectric insulator. *Nature Photonics* **10**, 611-616, doi:10.1038/nphoton.2016.143 (2016).

6. Matsuo, H., Noguchi, Y. & Miyayama, M. Gap-state engineering of visible-light-active ferroelectrics for photovoltaic applications. *Nature communications* **8**, 1-8 (2017).

7. You, L. *et al.* Enhancing ferroelectric photovoltaic effect by polar order engineering. *Science advances* **4**, eaat3438 (2018).

8. Catalan, G. & Scott, J. F. Physics and Applications of Bismuth Ferrite. *Advanced Materials* **21**, 2463-2485, doi:10.1002/adma.200802849 (2009).

9. Zavaliche, F. *et al.* Multiferroic BiFeO3 films: domain structure and polarization dynamics. *Phase Transitions* **79**, 991-1017, doi:10.1080/01411590601067144 (2006).

10. Sando, D., Barthelemy, A. & Bibes, M. $BiFeO_3$ epitaxial thin films and devices: past, present and future. *J Phys Condens Matter* **26**, 473201, doi:10.1088/0953-8984/26/47/473201 (2014).

11. Clark, S. & Robertson, J. Band gap and Schottky barrier heights of multiferroic $BiFeO_3$. *Applied physics letters* **90**, 132903 (2007).

12. Ihlefeld, J. F. *et al.* Optical band gap of BiFeO3 grown by molecular-beam epitaxy. *Applied Physics Letters* **92**, 142908, doi:10.1063/1.2901160 (2008).

13. Pisarev, R. V., Moskvin, A. S., Kalashnikova, A. M. & Rasing, T. Charge transfer transitions in multiferroic $BiFeO_3$ and related ferrite insulators. *Physical Review B* **79**, doi:10.1103/PhysRevB.79.235128 (2009).

14. Chen, F. S. Optically Induced Change of Refractive Indices in $LiNbO_3$ and $LiTaO_3$. *Journal of Applied Physics* **40**, 3389-3396, doi:10.1063/1.1658195 (1969).

15. Koch, W., Munser, R., Ruppel, W. & Würfel, P. Anomalous photovoltage in $BaTiO_3$. *Ferroelectrics* **13**, 305-307 (1976).

16. Kholkin, A., Boiarkine, O. & Setter, N. Transient photocurrents in lead zirconate titanate thin films. *Applied Physics Letters* **72**, 130-132, doi:10.1063/1.120663 (1998).

17. STUART, R. *Vacuum Technology, Thin Films, and Sputtering*. (1983).

18. Dijkkamp, D. *et al.* Preparation of Y-Ba-Cu oxide superconductor thin films using pulsed laser evaporation from high Tc bulk material. *Applied Physics Letters* **51**, 619-621, doi:10.1063/1.98366 (1987).

19. Harsha, K. *Principles of Physical Vapor Deposition of Thin Films*. (2005).

20. in *Epitaxial Growth of Complex Metal Oxides* (eds G. Koster, M. Huijben, & G. Rijnders) xiii-xvii (Woodhead Publishing, 2015).

21. Singh, R. K. & Narayan, J. Pulsed-laser evaporation technique for deposition of thin films: Physics and theoretical model. *Phys Rev B Condens Matter* **41**, 8843-8859, doi:10.1103/physrevb.41.8843 (1990).

22. Aziz, M. J. Film growth mechanisms in pulsed laser deposition. *Applied Physics A* **93**, 579-587, doi:10.1007/s00339-008-4696-7 (2008).

23. Miller, J. C. *Laser ablation: principles and applications*. Vol. 28 (Springer Science & Business Media, 2013).

24. Wang, J. *et al.* Epitaxial $BiFeO_3$ multiferroic thin film heterostructures. *science* **299**, 1719-1722 (2003).

25. King, D. A. & Woodruff, D. *Growth and properties of ultrathin epitaxial layers*. (Elsevier, 1997).

26. Paufler, P. AA Chernov. Modern crystallography III. Crystal growth with contributions by EI Givargizov, KS Bagdasarov, VA Kuznetsov, LN Demianets, AN Lobachev. Springer-verlag Berlin, Heidelberg, New York, Tokyo 1984, 517 pages, 244 figs. Price: Cloth, DM 154.—. ISBN 3-540-11516-1. *Crystal Research and Technology* **20**, 274-274 (1985).

27. Ayers, J. E. *Heteroepitaxy of Semiconductors*. (2018).

28. Baek, S. H. *et al.* Ferroelastic switching for nanoscale non-volatile magnetoelectric devices. *Nature Materials* **9**, 309-314, doi:10.1038/nmat2703 (2010).

29. Das, R. R. *et al.* Synthesis and ferroelectric properties of epitaxial $BiFeO_3$ thin films grown by sputtering. *Applied Physics Letters* **88**, 242904, doi:10.1063/1.2213347 (2006).
30. Phoon, B. L., Lai, C. W., Juan, J. C., Show, P.-L. & Chen, W.-H. A review of synthesis and morphology of $SrTiO_3$ for energy and other applications. *International Journal of Energy Research* **43**, 5151-5174, doi:https://doi.org/10.1002/er.4505 (2019).
31. Pai, Y.-Y., Tylan-Tyler, A., Irvin, P. & Levy, J. Physics of $SrTiO_3$-based heterostructures and nanostructures: a review. *Reports on Progress in Physics* **81**, 036503, doi:10.1088/1361-6633/aa892d (2018).
32. Guo, R. *et al.* Non-volatile memory based on the ferroelectric photovoltaic effect. *Nat Commun* **4**, 1990, doi:10.1038/ncomms2990 (2013).
33. Waseda, Y., Matsubara, E. & Shinoda, K. *X-ray diffraction crystallography: introduction, examples and solved problems*. (Springer Science & Business Media, 2011).
34. Birkholz, M. & Fewster, P. F. in *Thin Film Analysis by X-Ray Scattering* 297-341 (2005).
35. Voigtländer, B. *Atomic Force Microscopy*. (Springer, 2019).
36. Bhushan, B. *Scanning probe microscopy in nanoscience and nanotechnology 2*. (Springer Science & Business Media, 2010).
37. Soergel, E. Piezoresponse force microscopy (PFM). *Journal of Physics D: Applied Physics* **44**, 464003, doi:10.1088/0022-3727/44/46/464003 (2011).
38. Sawyer, C. B. & Tower, C. H. Rochelle Salt as a Dielectric. *Physical Review* **35**, 269-273, doi:10.1103/PhysRev.35.269 (1930).

Chapter 4

Elucidating the role of Schottky barrier on the ferroelectric photovoltaic output

The story begins with the elaboration of the role of Schottky barrier on the overall ferroelectric photovoltaic effect. This chapter presents three experimental strategies to investigate the impact of the interface while illuminating the ferroelectric solar cell with white light. Firstly, $BiFeO_3$ thickness was systematically tuned over five decades. The second employed strategy was implemented by shinning the back of the sample. Lastly, the top electrode material is varied while $La_{0.7}Sr_{0.3}MnO_3$ was used for all the sample series. The results presented in this chapter emphasize the dominant role played by Schottky barriers built up at the ferroelectric/metal interfaces in generating photocurrents.

4.1 Introduction

Ferroelectric photovoltaic effect, or FePV, is the generation of photocurrents in spatially homogeneous polar crystals under uniform illumination. In ferroelectric-based photovoltaics, light is absorbed creating electron-hole pairs before being separated by the internal fields accompanying the spontaneous polarization.[1-3] The key aspects of the FePV are the reversible switchability and above-bandgap open-circuit voltages which make them interesting for optoelectronic applications. The switchability property is associated with the spontaneous polarization reversal between two stable states upon applying external electric field. On the other hand, classical solar cells require a spatial inhomogeneity at the semiconductor/semiconductor or semiconductor/metal in order to separate the photoexcited charges. In these solar cells, the photovoltage is limited by the semiconductor bandgap, and requires processing of complicated layers.[4] Instead, ferroelectrics may enable efficiencies beyond those in junction-based solar cells that can exceed Shockley-Queisser (SQ) limit.[5-8] Therefore, it is worthy to further investigate the ferroelectric photovoltaic effect in order to push the efficiency forward.

The ferroelectric photovoltaic response has been intensively explored in several classical ferroelectrics such as $BaTiO_3$[7,9], $Pb(Zr,Ti)O_3$[10-12], $LiNbO_3$[13,14] during the last century. Indeed, the development of the bismuth ferrite ($BiFeO_3$)[15] during the last decade led to a renewed attention in the ferroelectric photovoltaic effect[6,16]. Since then, the field has passed through several milestones on the pathway to enhance the FePV efficiencies. This encompasses the bandgap engineering[17], employing nanoscale electrodes[7,18], and the reduction of the active layer size[19]. More interestingly, the recent emergence of photovoltaic effects in artificially distorted crystals giving rise to flexophotovoltaic[20] and piezophotovoltaic[21] effects has further heightened the need to further explore the mechanism of FePV.

On the fundamental level, the origination of the driving mechanism of the ferroelectric photovoltaic effect is still unclear. However, a number of theoretical models have been proposed to explain the experimental results including the shift current[22-24], ballistic

mechanism[7,9,25] and depolarization field-induced PV[12,26]. These mechanisms are driven by the ferroelectric polarization in the homogeneous bulk of the crystal giving rise to bulk photovoltaic effects. Moreover, Schottky barrier formed at the ferroelectric/metal interface induces interface band-bending leading to local built-in field which drives additional PV effect. As a junction photovoltaic effect, the photovoltage is limited by the Schottky barrier height. Additionally, the ferroelectric polarization assists in manipulating the Schottky barrier height leading to switchable PV behavior.

In order to elucidate the role of Schottky barrier on the ferroelectric photovoltaic response in vertical $BiFeO_3$ heterostructures, several experimental strategies are designed in this chapter. Firstly, systematic investigation of the thickness-dependent photovoltaic output. In fact, tuning the thickness of the ferroelectric layer while measuring the photovoltaic response gives access to the different possible competitions, i.e., bulk effects versus interface band-bending and absorption gain against the short carrier diffusion lengths. An unpolarized white light source, a requirement for the outdoor applications, is employed to illuminate the sample on both sides. Furthermore, the top electrode metal is varied which allows to modulate the top interface properties giving deeper insights into the ferroelectric photovoltaic in vertical $BiFeO_3$-based devices.

4.2 Growth

In this work, $BiFeO_3$ (BFO) is deposited on top of $SrTiO_3$ (STO) single crystal substrates buffered by $La_{0.7}Sr_{0.3}MnO_3$ (LSMO) thin films. Epitaxial films are successfully grown via pulsed laser deposition (PLD) technique employing the conditions presented in table (3.1) of section (3.2.1). In this section, the growth and morphology results of the films are discussed.

The (001)-oriented STO substrate are exploited in this work since its lattice parameters are close to that of BFO. STO exhibits cubic structure with lattice constant a = 3.905 Å[27]. On the other hand, bulk BFO and LSMO possess rhombohedral crystal structures which can be converted into pseudocubic parameters into a_{pc} (BFO) = 3.96 Å and a_{pc} (LSMO) = 3.873

Å. This indicates that BFO and LSMO suffer from compressive (-1.4%) and tensile (+0.8%) strains, respectively, on STO. To emphasize, both films grow with a pseudocubic $(001)_{pc}$ orientation. The lattice misfit in BFO/LSMO/STO stack is explained in Figure 4.1.

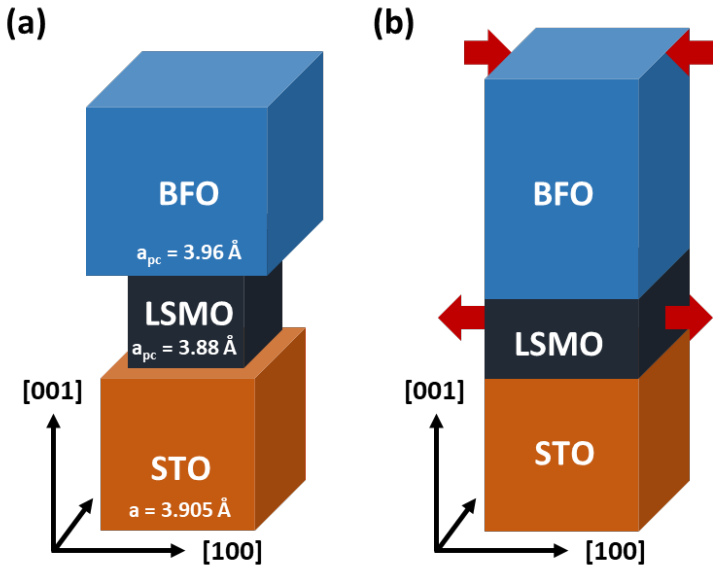

Figure 4.1: Lattice mismatch in BFO/LSMO/STO heterostructure. **(a)** Unit cells of bulk BFO, LSMO and STO before growth demonstrating compressive strain in BFO grown on STO in contrast to the tensile strain induced in LSMO/STO. **(b)** After growth, the mismatch is accommodated by distorting the crystal lattices to maintain the unit cell volume constant. LSMO unit cell is elongated in-plane while compressed along c-axis. The opposite for BFO case is true.

In this dissertation, monodomain BFO films are exploited for the photovoltaic measurements to rule out any contribution from the domain walls.[28,29] For this, STO substrate surface is cut off by an angle of 4° with respect to the $[001]_{pc}$ towards $[110]_{pc}$ (to be named 4STO) as presented in section (3.2.1.2).[30] The substrates are treated before the film growth by combined deionized water treatment and subsequent thermal annealing which was inspired by the method used for exact STO substrates reported in reference (31). In here, the substrates are annealed in air at 1000 ℃ for 120 min and subsequently sonicated in DI water for 30 min at 70 ℃. This way, the segregated SrO during the annealing step is leached out by the DI water leaving TiO_2-terminated 4STO substrates. Eventually, the substrates are washed in ethanol and acetone to remove any residual contaminants. As

shown in atomic force microscope (AFM) $4 \times 4\ \mu m^2$ image presented in Figure 4.2 (a), the as-received substrate exhibits root mean square (RMS) roughness of 0.3 nm. After treatment, step-terraced structure appeared on the substrate's surface which are smaller than those form on exact substrates owing to the large miscut angle. Further, 10 nm LSMO grown on the treated substrate imitated the step-terraced pattern as shown in Figure 4.2 (c). A series of BFO with varying thicknesses are grown on LSMO-buffered 4STO substrates. All the growth parameters (except the substrate temperature) were fixed for all films while the growth time is tuned to obtain the desired thickness. The temperature was slightly raised in case of the thicker films to compensate for the Bi excess owing to the prolonged growth time. The morphology of the BFO films with different thicknesses grown on LSMO/4STO

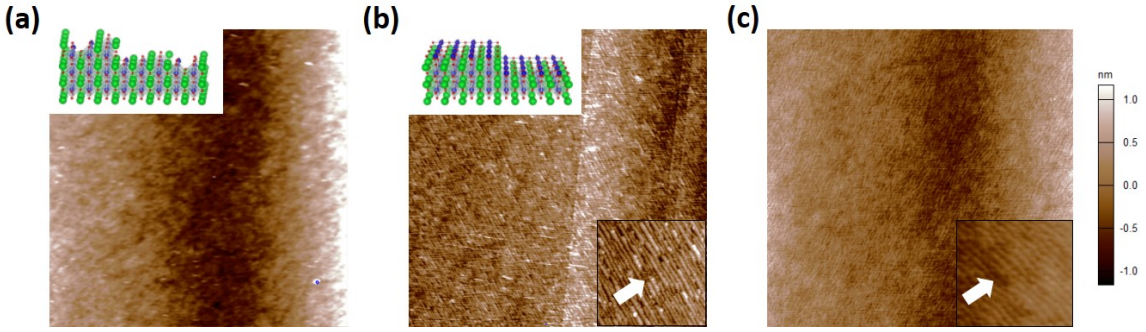

Figure 4.2: Atomic force microscope (AFM) images of the STO and LSMO. **(a)** As-received STO substrate with mixed SrO and TiO_2 terminations explained in the inset. **(b)** DI water leaching yields a step-terraced structure with the miscut direction pointed by the white arrow. **(c)** LSMO grown on top of the treated STO substrate copying its morphology.

are shown in Figure 4.3 (a). It is apparent from the topographic images that the surface is characterized by the saw teeth structure pointing to [110]. This is explained, as depicted in Figure 4.3 (b), by the growth of r_1 structural variant which involves the distortion of BFO unit cell to the free side while constrained at the step edge. More interestingly, the thicker

the BFO film, the finer the teeth pitch. Apparently, the step features of the substrate disappeared which indicates that the films tend to grow in 3D growth mode.

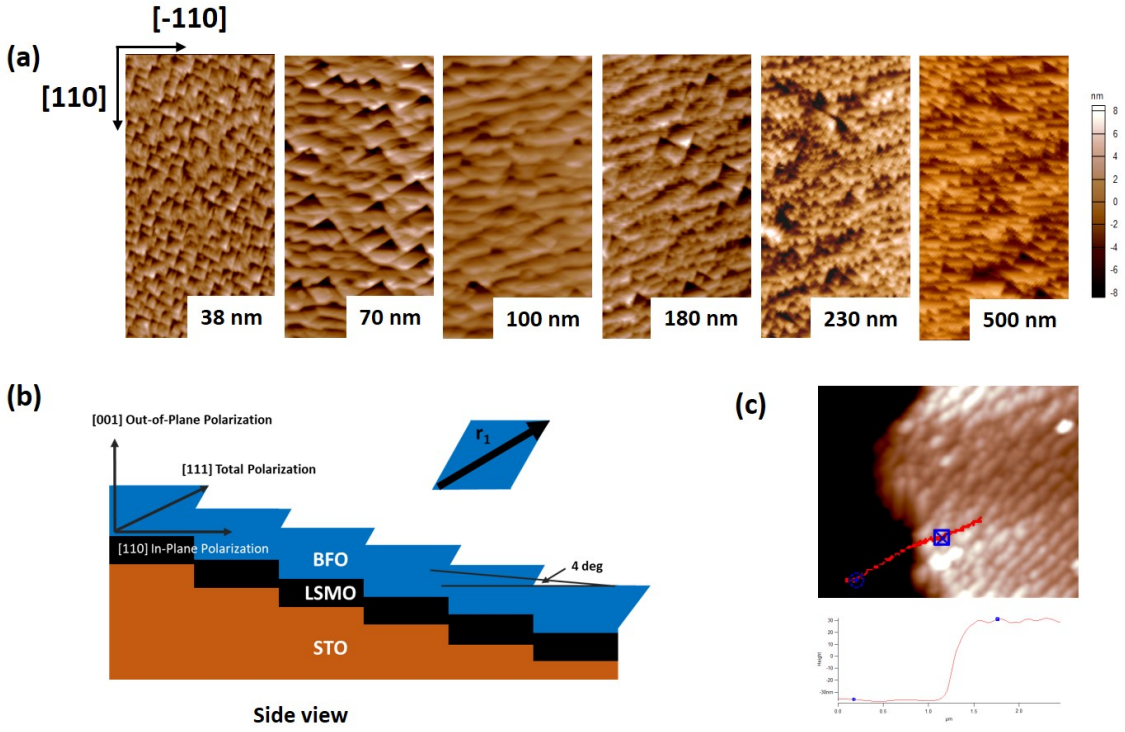

Figure 4.3: Topography of BFO thin films. **(a)** Atomic force microscope of thickness-variable BFO grown on LSMO/4STO. **(b)** Schematic demonstrating the emergence of saw teeth morphology on the BFO film due to the growth of single structural variant r_1 induced by the miscut in the STO substrate. **(c)** AFM image taken at the step between LSMO and BFO layers (top image). The profile curve revealed thickness of 70 nm is plotted in bottom image.

To measure the film thickness, a small portion at the edge of LSMO/4STO is covered during the deposition of BFO layer. This forms a step in which its height can be measured by AFM tip as exemplified by a (70 nm) BFO/LSMO/4STO heterostructure in Figure 4.3 (c). The nominal thicknesses of $BiFeO_3$ layers are 38 nm, 70 nm, 100 nm, 120 nm, 240 nm and 500 nm and shall be labelled by their thicknesses throughout this chapter, i.e., 38-BFO, 70-BFO, 100-BFO, 120-BFO, 240-BFO and 500-BFO, respectively.

4.3 Piezoresponse force microscopy (PFM) results

By means of piezoresponse force microscopy, or PFM, the mapping of the ferroelectric domains is enabled. In other words, PFM provides a microscopic picture of the polar domains by imaging several squared micrometers. In addition, it is possible to examine the most fundamental aspect of ferroelectric systems, i.e., the polarity switching, on the microscopic level. In this section the PFM studies of the 500-BFO thin film is presented. In this experiment, the reading voltage is applied to the AFM tip while the bottom electrode is grounded.

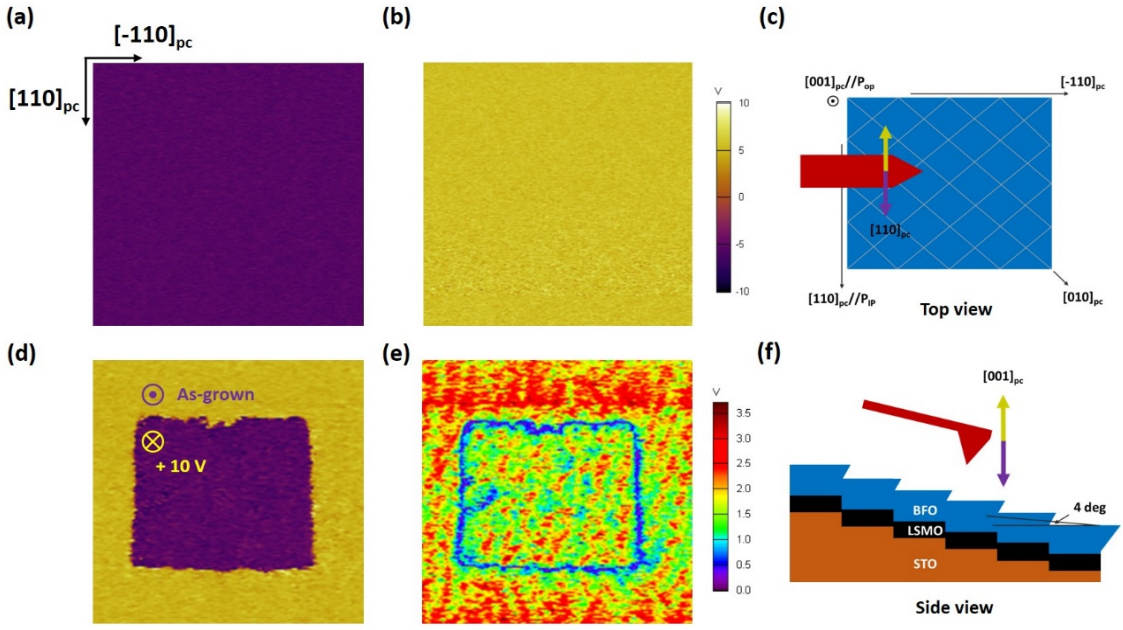

Figure 4.4: Piezoresponse force microscopy (PFM) studies exemplified by the 500 nm BFO/LSMO/4STO sample. **(a)** Lateral PFM phase image of size $4 \times 4\ \mu m^2$ showing the in-plane polarization pointing to $[110]_{pc}$ throughout the measured area. **(b)** Vertical PFM phase image of the same spot with upward out-of-plane polarization component **(c)** Illustration of the measurement set up where the cantilever is aligned along [-110]. Vertical polarization switching is implemented by applying +10 V to the tip yielding phase image **(d)** and amplitude image **(e)**. **(f)** Side view of the samples and the coloring code used in vertical PFM images.

As discussed in section (3.3.2.2), it is crucial to align the cantilever relative to the ferroelectric polarization of the thin film. Additionally, PFM images are acquired in two modes, namely, the lateral PFM and vertical PFM. Figure 4.4 (a) shows the lateral PFM

phase image which reveals uniform distribution of violet color. The yellowish image in Figure 4.4 (b) corresponds to the vertical PFM phase. Depictions in Figure 4.4 (c) and (f) illustrate these observations as follows. The cantilever is aligned parallel to the step edges identified from the topographic image presented in Figure 4.3 (a). In this case, the cantilever torsions along $[110]_{pc}$ are observed. Following the color coding in Figure 4.4 (f), BFO film solely exhibit r_1 variant with the in-plane component (P_{IP}) parallel to the miscut direction while the out-of-plane (P_{OP}) is aligned with $[001]_{pc}$. It is noteworthy to mention that the sample was rotated during the lateral PFM measurements to exclude the existence of other variants in the film. Therefore, 500 nm BFO is concluded to exhibit single ferroelectric domain structure.

In order to test the ferroelectric property of the BFO films, PFM is employed to perform local polarization switching on 500-BFO sample. The polarization reversal is performed in the vertical PFM mode. Prior to the polarization switching, the as-grown polarization state of a surface area of $5 \times 5\ \mu m^2$ was measured. Afterwards, the polarization is flipped by applying DC voltage +10 V to the AFM tip on $3 \times 3\ \mu m^2$ square. Eventually, the $5 \times 5\ \mu m^2$ area is mapped again giving rise to the contrasted phase image in Figure 4.4 (d). The image reveals switched square (of violet color) with downward polarization as well as the as grown upward state in yellow. Also, the amplitude image in Figure 4.4 (e) shows the same signal magnitude inside and outside the written box except the edges. The results presented in this section demonstrate the ferroelectric nature of the film since the film can maintain two opposite polarization states.

4.4 Crystal structure

The crystal structure, phase purity and the strain effect on the crystallinity of the BFO film series are investigated by means of high-resolution XRD technique. In this regard, symmetric 2θ-ω scan were performed on thickness-varying BFO grown on LSMO-buffered 4STO substrates. The STO [001] is aligned parallel to the scattering vector prior to the 2θ-ω scan through a combination of omega-, phi-, chi- and 2θ-ω scans. It is worth noting that the offcut angle of 4° between the substrate surface and (001) plane has to be

taken into account during the pre-alignment step. Therefore, the sample was aligned such that STO [110] is either parallel or perpendicular to the x-ray optical path. Simultaneously, chi or ω is corrected by 4° depending on the sample orientation.

Figure 4.5 (a) presents the 2θ-ω diffraction patterns of BFO/LSMO/4STO heterostructures. The diffraction peaks stemming from (00l) (l=1, 2) reflections of BFO, LSMO and STO indicating successful epitaxial growth. Besides, it shows no additional peaks originating from the parasites originating from the excessive or deficient Bi implying phase-pure BFO films. In fact, absence of impurities in BFO is of great importance which otherwise leads to suppression of the ferroelectric properties.[32] Furthermore, BFO peaks are shifted to the left side of STO while peaks from LSMO are on the right side signifying compressive and tensile strains with STO, respectively.

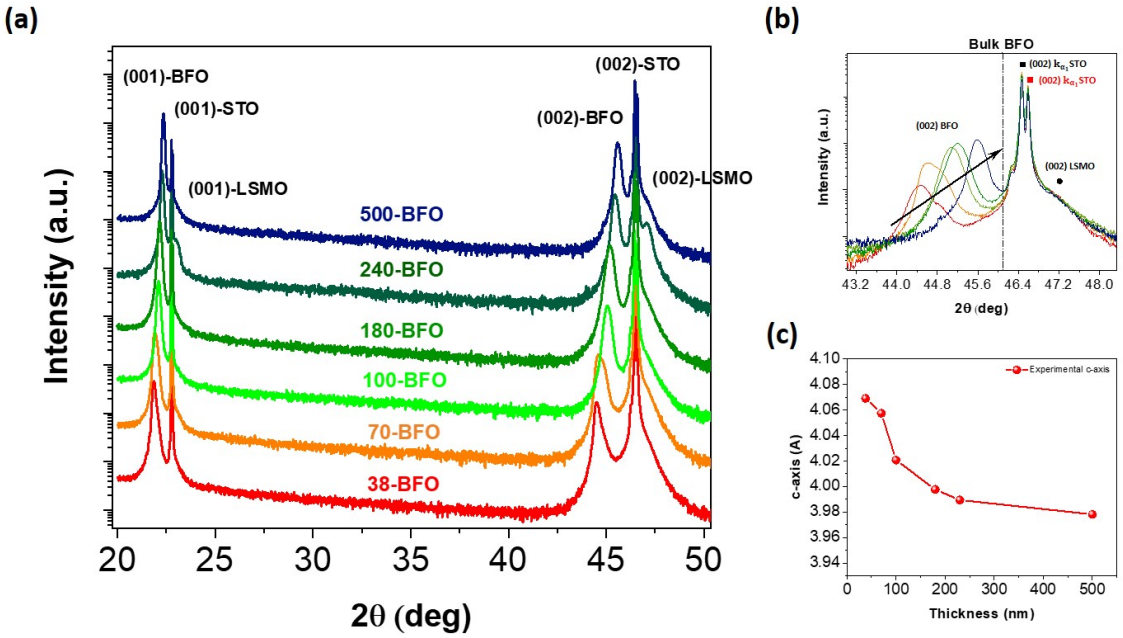

Figure 4.5: High resolution x-ray diffraction patterns of the thickness-dependent BFO series grown on 10 nm LSMO/4STO. **(a)** Symmetric 2θ-ω scan revealing phase purity of the BFO films. **(b)** Zoomed-in image around (002) peaks in which BFO peaks gradually shift to higher 2θ values. **(c)** Analysis of the out-of-plane lattice parameter indicates the strain release in BFO films by reducing the c_{pc} axis in thicker films.

A magnified image around (002) peaks is split into Figure 4.5 (b). The LSMO $(002)_{pc}$ peak is observed at 47.159° indicating a reduction in bulk c_{pc} to 3.849 A and the film is in fully strained state. It is also apparent from the plot that the BFO peak shift towards the STO peak as the film thickness increases. By extracting the c_{pc} parameters into Figure 4.5 (c), it decreases from 4.069 A in 38-BFO to 3.978 A in 500-BFO films. Although the compressive strain relaxes in thicker films, still under compressive strain.

4.5 Macroscopic ferroelectric properties

The macroscopic ferroelectric characteristics of the samples were obtained through measuring the polarization-electric field (PE) hysteresis loops. This is to complement the microscopic ferroelectric measurements in section (4.3). For this purpose, an array of platinum (Pt) square pads of $40 \times 40\ \mu m^2$ in size are sputtered on top of the BFO film forming ferroelectric vertical capacitors Pt/BFO/LSMO which are exploited for the photovoltaic measurements presented in next section. The Sawyer-Tower circuit is used to measure the PE loops as explained in section (3.4.1).

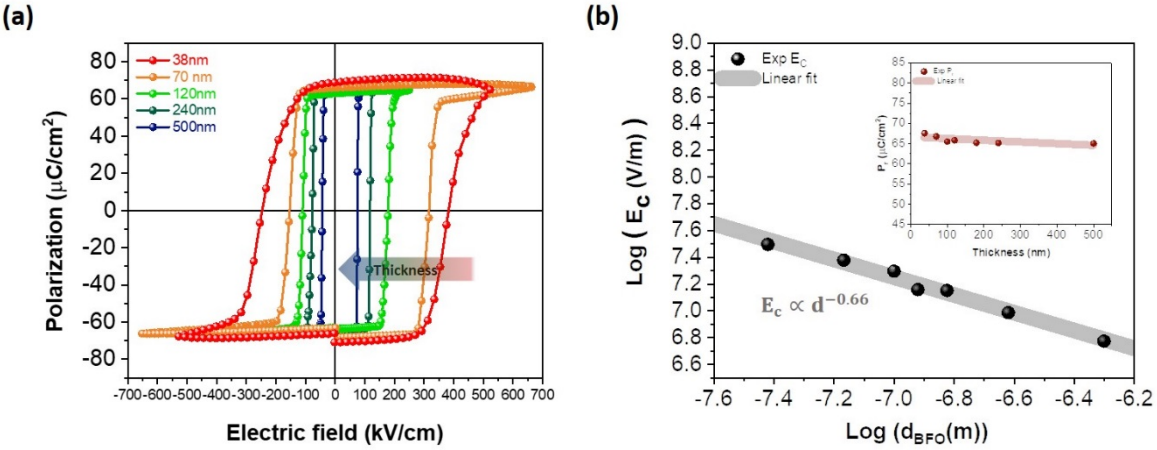

Figure 4.6: Thickness-dependent macroscopic ferroelectric properties of BFO films. **(a)** The polarization-electric field hysteresis loops of the BFO capacitors with different thicknesses **(b)** Typical Janovec-Kay-Dunn coercive field law. The straight line is a least-squares fit yields scaling exponent of K = -0.66. The inset shows a slight increase in the remnant polarization in thinner films from 65 $\mu C/cm^2$ to 67 $\mu C/cm^2$.

Figure 4.6 (a) presents the evolution of the PE hysteresis loops with BFO layer thickness. The acquired loops show rectangular-shaped and well-saturated PE loops reflecting the intrinsic and monodomain ferroelectricity of the $BiFeO_3$ films. On the other hand, the remnant polarization P_r remained constant for all samples (65 $\mu C/cm^2$) along $[001]_{pc}$ except for the 38-BFO in which a slightly larger P_r (67 $\mu C/cm^2$) was revealed and could be attributed to the larger compressive strain state in correlation with XRD results in Figure 4.5 (c).[33] At such small thickness, the rhombohedral symmetry likely coexist with the monoclinic one evidenced by the emergence of a second peak as shown in figure 4.5 (b). In this case, the c_{pc} axis is elongated enhancing the magnitude of the out-of-plane polarization.[34]

Furthermore, there is a clear trend of decreasing the coercive field (defined as $(|E_{C+}| + |E_{C-}|)/2$ where E_{C+} and E_{C-} are the positive and negative coercive fields, respectively) as the BFO thickness increases. Interestingly, the coercive field can be modeled as $E_C \propto d_{BFO}^{-0.66}$ with the thickness as set out in the log-log plot shown in Figure 4.6 (b). This result is explained by the Janovec-Kay-Dunn (JKD) scaling law for coercive fields in ferroelectrics which suggests nucleation-growth switching mechanism in the films.[35,36] Similar findings were obtained in stripe domain-structured BFO films,[37] PZT[38] and PVDF[39,40] while deviated from JKD law in other studies.[41,42] However, the breakdown of the law has been ascribed to the depolarization field and the interfacial dielectric layer.

4.6 Photovoltaic properties

In this section, photovoltaic (PV) studies are introduced. In order to investigate the photovoltaic mechanism in BFO heterostructures, different strategies were employed such as varying the films thickness, tuning the light intensity and upside-down light illumination. Also, the top electrode work function was changed by varying the type of metal. In all cases, the current density (J-V) curves were collected using source-meter device in the downward- and upward-polarization states under unpolarized white lightening to evaluate the PV response. Further, the sample poling process was carried out by applying the voltage to the bottom electrode prior to the PV data collection.

4.6.1 Thickness scaling of photovoltaic effect

To begin, the photovoltaic behavior (PV) of the thickness variable BFO series is presented. Current-voltage curves (J-V) were collected under white lightening with 50 mW/cm^2 through the top electrode. The (J-V) curves were measured in the downward and upward polarization states, as presented in Figure 4.7 (a) and (c), respectively. It is apparent from the figure that the PV behavior is switchable for all the films, i.e., the polarity of the short-circuit current density J_{sc} and open-circuit voltage V_{oc} change upon reversing the ferroelectric polarization. V_{oc}^{down} has a negative value in case of polarization is downward while V_{oc}^{up} is positive when the polarization points upward.

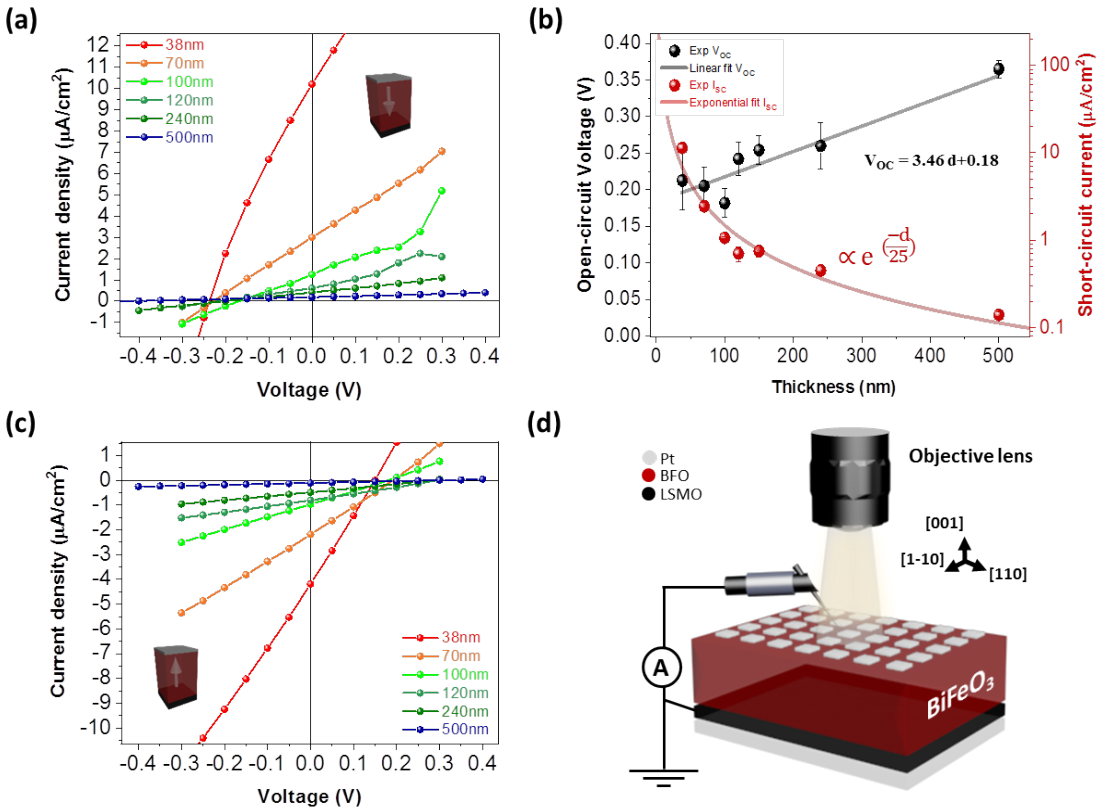

Figure 4.7: Thickness-scaling of photovoltaic effects in BFO vertical capacitors. Current density - voltage J-V curves measured under light in the down- **(a)** and up- **(c)** ferroelectric polarization states. **(b)** Plot of the extracted values of the V_{OC} and I_{SC} as a function of the BFO thickness fitted as straight line and exponential decay, respectively. **(d)** Schematic of the device under test. The unpolarized white light is provided through the objective lens to the platinum pad.

Further analysis revealed two discrete observations from the extracted J_{sc} and V_{oc} values (see Figure 4.7 (b)). First, the exponential decay of the J_{sc} as the thickness increases. Surprisingly, J_{sc} of the 38-BFO sample has a value of 11.49 μA/cm^2 which is one order-of-magnitude larger than the current density in the 500-nm film (0.122 μA/cm^2). Second, and in contrary to J_{sc}, V_{oc} is found to be linearly proportional to the BFO film thickness (rise from 0.2 V in 38-BFO to 0.36 V in 500-BFO). These two findings raise the question regarding the dominating driving mechanism(s) of the switchable ferroelectric photovoltaic effect in vertical BFO structures; bulk polarization-related (BPVE), interface band-bending or depolarization field (E_d)?

Before proceeding to address this, it is necessary to examine the nature of the interface at the Pt/BFO and BFO/LSMO contacts. The electrical transport of the devices was tested in dark in which the bias voltage is applied in the same direction of the polarization avoiding any polarization switching during the data collection. Figure 4.8 shows the J-E$^{0.5}$ curves for a representative sample - 240-BFO - which demonstrate asymmetric curves. This indicates asymmetric contacts and interface-limited conduction in the heterostructure. Furthermore, fitting the curves reveals 1.1 V and 0.86 V Schottky barriers corresponding to the Pt/BFO and BFO/LSMO contacts, respectively. Having established that the Schottky emission is dominating the conduction mechanism in the PV cells, the possible dominating PV mechanism(s) can be then discussed.

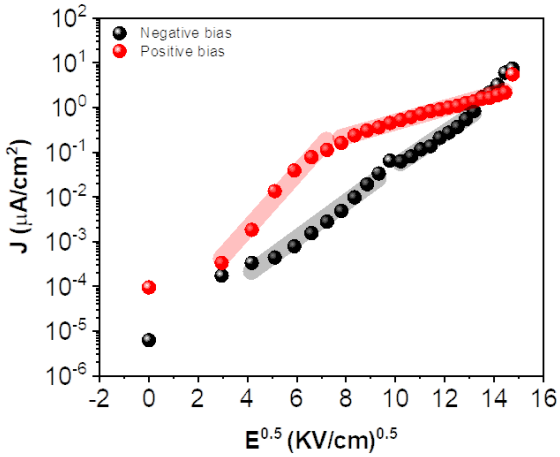

Figure 4.8: Fits of the typical J-E0.5 curves of Pt/(240 nm) BFO/LSMO heterostructure at 300 K.

Overall, the photovoltaic effect is obviously enhanced in the thinnest Pt/BFO/LSMO cell, i.e., 38-BFO manifested by the significant increase of the photocurrent in contrary to the slight reduction of V_{OC}. However, the ferroelectric results clearly demonstrated well-screened polarization. Moreover, the depolarization field scales as 1/d with the thickness which may exclude any involvement from the depolarization field in the photocurrent. Now the likely originations of the photovoltaic effect in BFO films can be narrowed down to BPVE and Schottky barrier-driven PV. It is apparent that there is a weak monotonic increase of V_{OC} with increasing BFO film thickness which one may correlate with equation (2.11).[25] For example, Z. Gu, *et al.*[9] have proven experimentally the rise of the V_{OC} as the thickness scales up in ITO/$BaTiO_3$/$SrRuO_3$ stacks with vertical geometry. Obviously, further experimental design is needed to elaborate on this point.

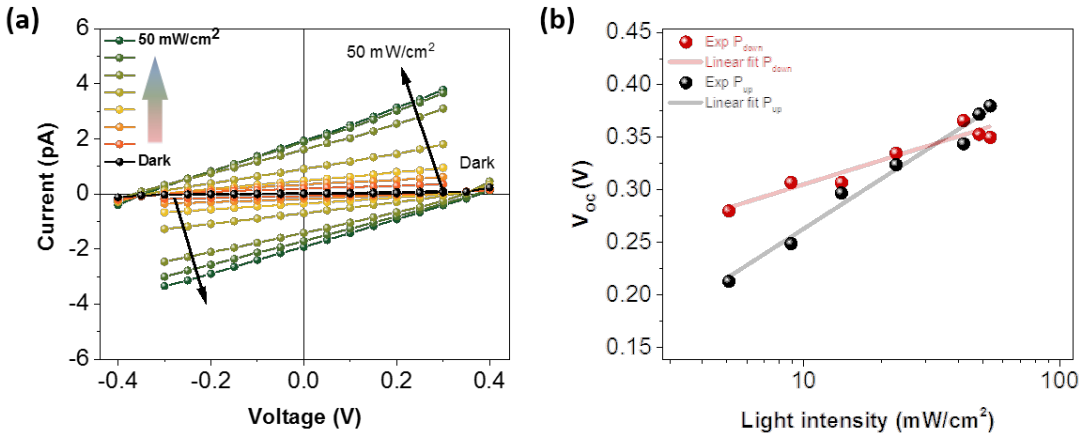

Figure 4.9: Light intensity response of the device performance. **(a)** J-V curves in up- and down-polarization states under different white light intensities. **(b)** Linear dependence of V_{OC} on logarithmic light intensity. Despite the linearity in both polarization orientations, the fitted lines' slopes are different which might be correlated with the interface band-bending.

On the other hand, the V_{OC} generated through BPVE was found to be independent on the light intensity as reported in references ([7,25]). This contradicts the results in Figure 4.9 presenting the (J-V) dependence on the light intensity for the 500-BFO sample (in which the BPVE is conceptually maximized among the series' samples). Intriguingly, the V_{OC} increases with light intensity in case of upward and downward polarization states. This behavior is characteristic to the junction-based photovoltaic effect.[43,44] Based on this, it is

reasonable to suggest that the BPVE can be excluded as a major mechanism to the ferroelectric photovoltaic effect.

Although the white light absorption gain in the 38-nm $BiFeO_3$ film dropped by around 13%[45] (compared to the 500-nm film), the photocurrent is enhanced by one-order of magnitude. On the other hand, BFO is characterized by short charge carrier diffusion lengths (~10 nm).[46] The implication here is that only charge carriers in the proximity of BFO/metal interfaces can contribute to the photovoltaic response. To this end, the observed decay of the photocurrent with the thickness (despite the higher light absorption gain) can be now explained by the intense charge carrier recombination. In other words, the thickness shrinking leads to enhanced collection efficiency. This discussion consolidates the idea that the interface band-bending dominates the photovoltaic response in BFO cells under test with an insignificant contribution from the bulk photovoltaic effect. Ideally, to make the most of the BFO cell, a Schottky barrier width that is comparable to the BFO thickness is recommended, i.e., ultrathin BFO films can be employed for highly efficient ferroelectric PV cell. This is crucial for the compensation for the short diffusion length of the charge carriers and hence a maximized photocurrent.

4.6.2 Upside-down $BiFeO_3$ PV cells

The magnitudes of the J_{SC} in downward polarization state J_{SC}^{down} is larger than in upward polarization state J_{SC}^{up} in all BFO samples. Also, J_{SC}^{up} can be compared with J_{SC}^{down} data which shows different decay constants within 5 decades of thicknesses (0.025 nm^{-1} and 0.04 nm^{-1}, respectively). This provides further support for the hypothesis that the interface-induced photovoltaic effect in our devices dominates the overall response.

Hence, an experiment was designed to further explore the reason behind this asymmetric PV response by back illuminating the cell, i.e., through the bottom electrode. As depicted in Figure 4.10 (b), a Pt/(500 nm)BFO/(10 nm)LSMO stack was grown on a two-side-polished STO substrate with miscut angle of 4° along [110] direction so that the top and bottom electrodes are effectively separated. Intriguingly, and as shown in Figure 4.10 (a), there is a difference between the (J-V) measurements in the two configurations

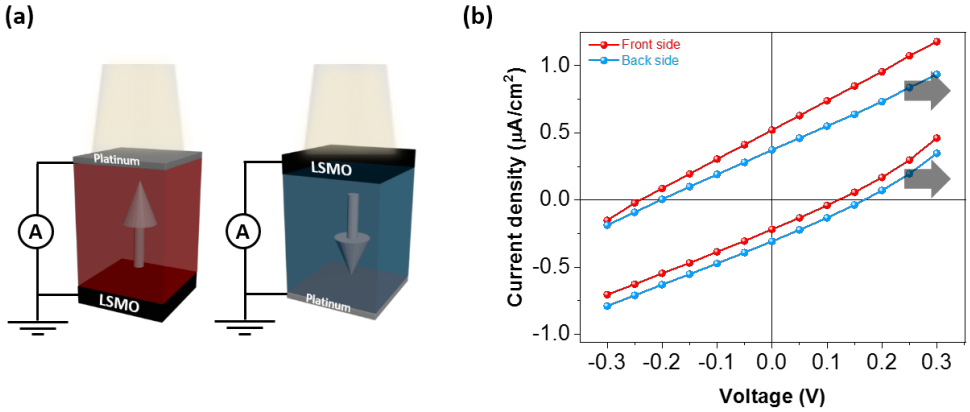

Figure 4.10: Comparison of the PV behavior upon front- and back-irradiation of the transparent device. **(a)** Sketch of the setup for the testing device. BFO/LSMO bilayer is grown on top of a transparent STO substrate to allow light transmission. Both measuring configurations are in upstate which is defined by polarization arrow points to the Pt electrode. **(b)** A parallel shift of the (J-V) curves (indicated by the gray arrows) after illuminating through the transparent STO/LSMO.

demonstrated by the parallel shift of the curves towards the right direction. Obviously, the photovoltaic behavior associated with the upward polarization state is enhanced in contrast to the downward one when the LSMO/BFO interface is directly exposed to the light. Since the light is absorbed in the BFO layer following Beer-Lambert law ($I = I_o e^{-\alpha d}$) before reaching the bottom interface, it gives rise to the asymmetry in PV behavior.

Once again, this result is consistent with the band-bending induced PV picture proposed in this work with the cell modelled as two back-to-back Schottky diodes with the PV stems from the diode that is reverse-biased. In general, therefore, it is possible to confirm that PV response in P_{up} state mainly stems from bottom interface (BFO/LSMO) while in P_{down} state is principally from the top interface (Pt/BFO) as shown in Figure 4.11. It is now possible

to hypothesize that tuning the nature of either the interfaces can greatly modulate the overall photovoltaic response in the ferroelectric cell.

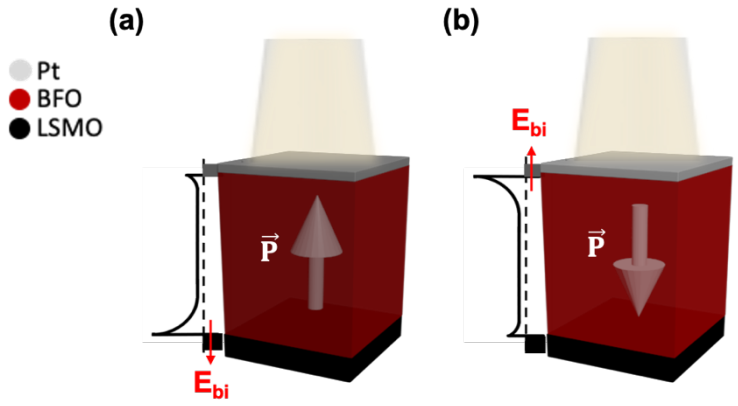

Figure 4.11: Schematic representation of the polarization-modulated interface ferroelectric photovoltaic effect. The ferroelectric photovoltaic cell can be modelled as two back-to-back rectifying diodes. **(a)** Upward polarization state in which the bottom interface band-bending dominates the overall photovoltaic output. **(b)** Downward polarization induces a higher band-bending at the top interface. The electronic band structure is plotted to the left side of the stack. Dashed straight lines represent Fermi levels. E_{bi} is the built-in electric field due to the band-bending at $BiFeO_3$/metal interfaces.

4.6.3 Effect of top interface on PV response

In this section, the characteristics of the interfaces at the top electrode/BFO are tuned by varying the type of the electrode in order to get further insight into the interface effect on the ferroelectric photovoltaic performance. For this, a series of monodomain BFO samples of fixed thickness (120 nm) and bottom electrode (LSMO) were grown on 4STO substrates. The top metal electrodes (10 nm thick) were varied among Au, Pt, Ag, Cu, Ta and Fe metals making samples named Au-BFO, Pt-BFO, Ag-BFO, Cu-BFO, Ta-BFO and Fe-BFO, respectively.

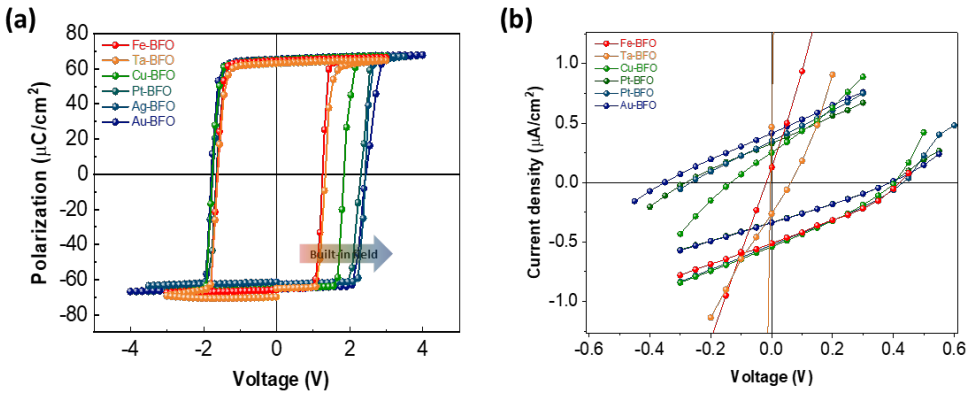

Figure 4.12: Tuning the top metal/BFO interface in the vertical capacitors. **(a)** (P-V) loops of metal electrode/BFO/LSMO films showing progressive offset in the positive side of the loop **(b)** Light (J-V) curves for the BFO/LSMO heterostructures with different top electrodes.

Figure 4.12 (a) displays the polarization-voltage (P-V) hysteresis loops measured for the whole series showing rectangular shape and P_r = 65 μC/cm^2 in all samples. Surprisingly, a horizontal shift of the (P-V) hysteresis loop towards the positive direction emerges leading to coercivity evolving from V_c^+= 1.25 V in Fe-BFO to 2.45 V in Au-BFO. In Figure 4.12 (b), a set of (J-V) curves under white light illumination from the different cells in P_{up} and P_{down} states are compared showing significant differences. However, the most striking result to emerge from the P_{down} (J-V) curves, which was proven to stem from the top interface, is the suppression of the photovoltaic effect in the Ta-BFO. In P_{up} state, all the devices showed sizable photovoltaic response. Furthermore, the extracted switchable open-circuit voltage values (given by $1/2\,(V_{OC}^{up} - V_{OC}^{down})$) are correlated with the coercive voltages as summarized in Figure 4.13 (a).

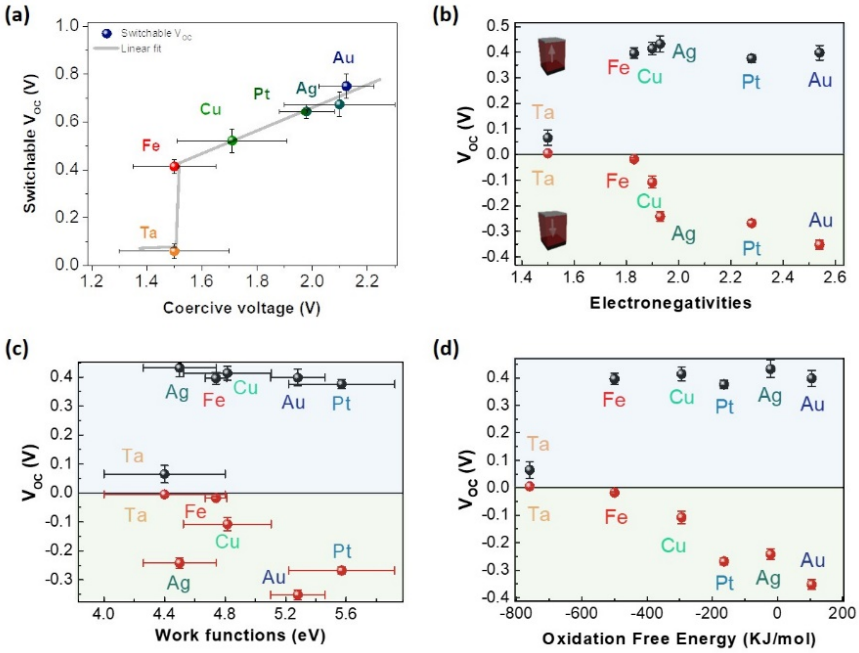

Figure 4.13: (a) Correlation between the switchable V_{OC} against coercive field extracted from P-V and J-V plots. Dependence of extracted V_{OC} on **(b)** electronegativities, **(c)** work function and **(d)** oxidation free energies of the top electrode metals.

The findings demonstrate that an additional negative built-in electric field is introduced at the top interface and increases as the metal electronegativity increases[47] as shown in Figure 4.13 (b). This may gradually change the ohmic-like contact with the Ta and Fe metals to a rectifying one in Cu, Ag, Pt and Au matching the previous studies on PZT.[48,49]. However,

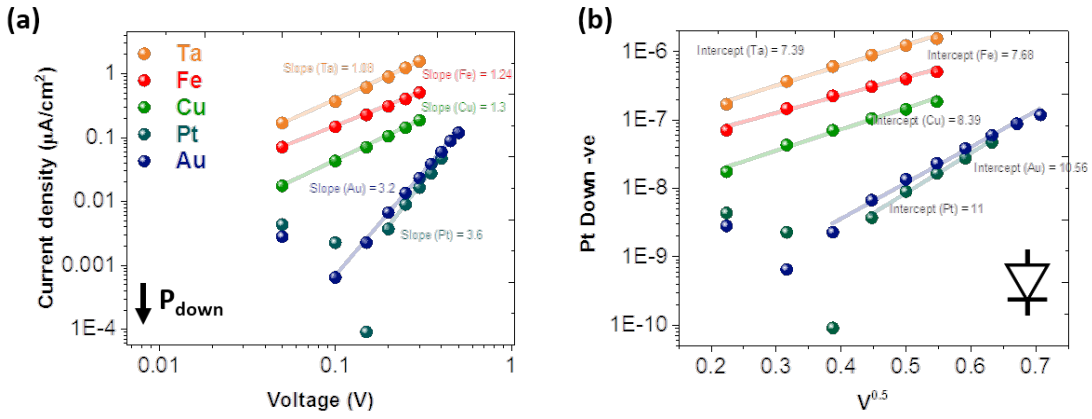

Figure 4.14: Electrical measurements of BFO/LSMO heterostructures in dark at room temperature. **(a)** J-V curves collected in dark. **(b)** Schottky plots.

the Schottky barrier heights with noble metals, i.e., Ag, Pt and Au, are larger than the Cu-BFO case. Additionally, no clear correlation with the metal work function trend is observed as in Figure 4.13 (c).

To further analyze this, dark (J-V) curves of the samples in down-polarization state were collected as shown in Figure 4.14. The linear fitting of the curves indicates the ohmic contact at Ta/BFO interface. Turning to the up-polarization and assuming that changing the top electrode should not affect the properties at the bottom interface, the (J-V) curves are expected to remain the same for different top electrodes. However, V_{oc}^{up} and J_{sc}^{up} are very small in Ta-BFO compared to the other devices. The reason for this is not clear but it may have something to do with the formation of high density of trap states at the interface. As shown in Figure 4.13 (d) emphasizes that Ta metal has a low oxidation free energy (-760 KJ/mol) which likely creates an oxide layer in contact with $BiFeO_3$ film. This is evidenced in the tantalum pentoxide (Ta_2O_5) that is exploited as a charge-trapping layer in non-volatile memories[50,51] and probably lead to a heavy trap-assisted recombination in our device.

4.7 Summary

Together, these results suggest that Schottky barrier is a requirement to measure photovoltaic effect in ferroelectric samples with vertical geometries. The ability to modulate the Schottky diode characteristics by the reversal of the polarization gives rise to a switchable PV behavior. Based on this premise, light is absorbed by the bulk of the ferroelectric layer producing the electron-hole pairs before being injected into the metal electrodes with the assistance of Schottky barrier at the interface. Additionally, the higher the Schottky barrier, the greater the photovoltaic response which can be realized by the choice of a noble metal as a top electrode. Also, shrinking the device thickness is crucial for the compensation for the short diffusion length of the charge carriers and hence a maximized photocurrent. This chapter provides a recipe for realizing a high ferroelectric photovoltaic performance in $BiFeO_3$ with vertical capacitors.

References

1. Fridkin, V. M. *Photoferroelectrics*. Vol. 9 (Springer, Berlin, Heidelberg, 1979).

2. Lopez-Varo, P. *et al.* Physical aspects of ferroelectric semiconductors for photovoltaic solar energy conversion. *Physics Reports* **653**, 1-40, doi:10.1016/j.physrep.2016.07.006 (2016).

3. Paillard, C. *et al.* Photovoltaics with Ferroelectrics: Current Status and Beyond. *Adv Mater* **28**, 5153-5168, doi:10.1002/adma.201505215 (2016).

4. Polman, A., Knight, M., Garnett, E. C., Ehrler, B. & Sinke, W. C. Photovoltaic materials: Present efficiencies and future challenges. *Science* **352**, aad4424, doi:10.1126/science.aad4424 (2016).

5. Glass, A. M., Linde, D. v. d. & Negran, T. J. High-voltage bulk photovoltaic effect and the photorefractive process in $LiNbO_3$. *Applied Physics Letters* **25**, 233-235, doi:10.1063/1.1655453 (1974).

6. Yang, S. Y. *et al.* Above-bandgap voltages from ferroelectric photovoltaic devices. *Nature Nanotechnology* **5**, 143-147, doi:10.1038/nnano.2009.451 (2010).

7. Spanier, J. E. *et al.* Power conversion efficiency exceeding the Shockley–Queisser limit in a ferroelectric insulator. *Nature Photonics* **10**, 611-616, doi:10.1038/nphoton.2016.143 (2016).

8. Shockley, W. & Queisser, H. J. Detailed Balance Limit of Efficiency of p-n Junction Solar Cells. *Journal of Applied Physics* **32**, 510-519, doi:10.1063/1.1736034 (1961).

9. Gu, Z. *et al.* Mesoscopic Free Path of Nonthermalized Photogenerated Carriers in a Ferroelectric Insulator. *Phys Rev Lett* **118**, 096601, doi:10.1103/PhysRevLett.118.096601 (2017).

10. Qin, M., Yao, K. & Liang, Y. C. Photovoltaic characteristics in polycrystalline and epitaxial $(Pb_{0.97}La_{0.03})(Zr_{0.52}Ti_{0.48})O_3$ ferroelectric thin films sandwiched between different top and bottom electrodes. *Journal of Applied Physics* **105**, doi:10.1063/1.3073822 (2009).

11. Zheng, F. *et al.* Above 1% efficiency of a ferroelectric solar cell based on the $Pb(Zr,Ti)O_3$ film. *J. Mater. Chem. A* **2**, 1363-1368, doi:10.1039/c3ta13724d (2014).

12. Zheng, F., Xu, J., Fang, L., Shen, M. & Wu, X. Separation of the Schottky barrier and polarization effects on the photocurrent of Pt sandwiched $Pb(Zr_{0.20}Ti_{0.80})O_3$ films. *Applied Physics Letters* **93**, doi:10.1063/1.3009563 (2008).

13. Glass, A. M., von der Linde, D., Auston, D. H. & Negran, T. J. Excited state polarization, bulk photovoltaic effect and the photorefractive effect in electrically polarized media. *Journal of Electronic Materials* **4**, 915-943, doi:10.1007/BF02660180 (1975).

14. Arizmendi, L. Photonic applications of lithium niobate crystals. *physica status solidi (a)* **201**, 253-283, doi:10.1002/pssa.200303911 (2004).

15. Wang, J. *et al.* Epitaxial $BiFeO_3$ Multiferroic Thin Film Heterostructures. *Science* **299**, 1719-1722, doi:10.1126/science.1080615 (2003).

16. Choi, T., Lee, S., Choi, Y. J., Kiryukhin, V. & Cheong, S.-W. Switchable Ferroelectric Diode and Photovoltaic Effect in BiFeO3. *Science* **324**, 63-66, doi:10.1126/science.1168636 (2009).

17. Nechache, R. *et al.* Bandgap tuning of multiferroic oxide solar cells. *Nature Photonics* **9**, 61-67, doi:10.1038/nphoton.2014.255 (2014).

18. Sturman, B. & Podivilov, E. Tip-enhanced bulk photovoltaic effect. *Physical Review B* **96**, doi:10.1103/PhysRevB.96.134107 (2017).

19. Tan, Z. *et al.* Thinning ferroelectric films for high-efficiency photovoltaics based on the Schottky barrier effect. *NPG Asia Materials* **11**, doi:10.1038/s41427-019-0120-3 (2019).

20. Yang, M.-M., Kim, D. J. & Alexe, M. Flexo-photovoltaic effect. *Science* **360**, 904-907, doi:10.1126/science.aan3256 (2018).

21. Nadupalli, S., Kreisel, J. & Granzow, T. Increasing bulk photovoltaic current by strain tuning. *Science Advances* **5**, eaau9199, doi:10.1126/sciadv.aau9199 (2019).

22. Young, S. M., Zheng, F. & Rappe, A. M. First-principles calculation of the bulk photovoltaic effect in bismuth ferrite. *Phys Rev Lett* **109**, 236601, doi:10.1103/PhysRevLett.109.236601 (2012).

23. Young, S. M. & Rappe, A. M. First principles calculation of the shift current photovoltaic effect in ferroelectrics. *Phys Rev Lett* **109**, 116601, doi:10.1103/PhysRevLett.109.116601 (2012).

24. Wang, F. & Rappe, A. M. First-principles calculation of the bulk photovoltaic effect in $KNbO_3$ and $(K,Ba)(Ni,Nb)O_{3-\delta}$. *Physical Review B* **91**, doi:10.1103/PhysRevB.91.165124 (2015).

25. Zenkevich, A. *et al.* Giant bulk photovoltaic effect in thin ferroelectric $BaTiO_3$ films. *Physical Review B* **90**, doi:10.1103/PhysRevB.90.161409 (2014).

26. Qin, M., Yao, K. & Liang, Y. C. Photovoltaic mechanisms in ferroelectric thin films with the effects of the electrodes and interfaces. *Applied Physics Letters* **95**, doi:10.1063/1.3182824 (2009).

27. Okazaki, A. & Kawaminami, M. Lattice constant of strontium titanate at low temperatures. *Materials Research Bulletin* **8**, 545-550 (1973).

28. Guo, R., You, L., Chen, L., Wu, D. & Wang, J. Photovoltaic property of $BiFeO_3$ thin films with 109° domains. *Applied Physics Letters* **99**, doi:10.1063/1.3641905 (2011).

29. Seidel, J. *et al.* Efficient photovoltaic current generation at ferroelectric domain walls. *Phys Rev Lett* **107**, 126805, doi:10.1103/PhysRevLett.107.126805 (2011).

30. Guo, R. *et al.* Non-volatile memory based on the ferroelectric photovoltaic effect. *Nat Commun* **4**, 1990, doi:10.1038/ncomms2990 (2013).

31. Connell, J. G., Isaac, B. J., Ekanayake, G. B., Strachan, D. R. & Seo, S. S. A. Preparation of atomically flat $SrTiO_3$ surfaces using a deionized-water leaching and thermal annealing procedure. *Applied Physics Letters* **101**, doi:10.1063/1.4773052 (2012).

32. Béa, H. *et al.* Influence of parasitic phases on the properties of $BiFeO_3$ epitaxial thin films. *Applied Physics Letters* **87**, doi:10.1063/1.2009808 (2005).

33. Biegalski, M. D. *et al.* Strong strain dependence of ferroelectric coercivity in a $BiFeO_3$ film. *Applied Physics Letters* **98**, doi:10.1063/1.3569137 (2011).

34. Kim, D. H., Lee, H. N., Biegalski, M. D. & Christen, H. M. Effect of epitaxial strain on ferroelectric polarization in multiferroic $BiFeO_3$ films. *Applied Physics Letters* **92**, 012911, doi:10.1063/1.2830799 (2008).

35. Kay, H. F. & Dunn, J. W. Thickness dependence of the nucleation field of triglycine sulphate. *Philosophical Magazine* **7**, 2027-2034, doi:10.1080/14786436208214471 (1962).

36. Janovec, V. On the theory of the coercive field of single-domain crystals of $BaTiO_3$. *Cechoslovackij fiziceskij zurnal* **8**, 3-15, doi:10.1007/bf01688741 (1958).

37. Steffes, J. J., Ristau, R. A., Ramesh, R. & Huey, B. D. Thickness scaling of ferroelectricity in $BiFeO_3$ by tomographic atomic force microscopy. *Proc Natl Acad Sci U S A* **116**, 2413-2418, doi:10.1073/pnas.1806074116 (2019).

38. Lee, H. N. *et al.* Suppressed dependence of polarization on epitaxial strain in highly polar ferroelectrics. *Phys Rev Lett* **98**, 217602, doi:10.1103/PhysRevLett.98.217602 (2007).

39. Chandra, P., Dawber, M., Littlewood, P. B. & Scott, J. F. Scaling of the Coercive Field with Thickness in Thin-Film Ferroelectrics. *Ferroelectrics* **313**, 7-13, doi:10.1080/00150190490891157 (2004).

40. Ducharme, S. *et al.* Intrinsic ferroelectric coercive field. *Phys Rev Lett* **84**, 175-178, doi:10.1103/PhysRevLett.84.175 (2000).

41. Dawber, M., Chandra, P., Littlewood, P. B. & Scott, J. F. Depolarization corrections to the coercive field in thin-film ferroelectrics. *Journal of Physics: Condensed Matter* **15**, L393-L398, doi:10.1088/0953-8984/15/24/106 (2003).

42. Maksymovych, P. *et al.* Ultrathin limit and dead-layer effects in local polarization switching of $BiFeO_3$. *Physical Review B* **85**, doi:10.1103/PhysRevB.85.014119 (2012).

43. Du, T. *et al.* Elucidating the Origins of Subgap Tail States and Open-Circuit Voltage in Methylammonium Lead Triiodide Perovskite Solar Cells. *Advanced Functional Materials* **28**, 1801808, doi:10.1002/adfm.201801808 (2018).

44. Zhang, Y. *et al.* High light intensity effects on nanoscale open-circuit voltage for three common donor materials in bulk heterojunction solar cells. *Energy & Environmental Science* **6**, 1766-1771, doi:10.1039/C3EE40457A (2013).

45. Han, H. *et al.* Switchable ferroelectric photovoltaic effects in epitaxial h-RFeO3 thin films. *Nanoscale* **10**, 13261-13269, doi:10.1039/C7NR08666K (2018).

46. Seidel, J. *et al.* Efficient Photovoltaic Current Generation at Ferroelectric Domain Walls. *Physical Review Letters* **107**, 126805, doi:10.1103/PhysRevLett.107.126805 (2011).

47. Mönch, W. Barrier heights of real Schottky contacts explained by metal-induced gap states and lateral inhomogeneities. *Journal of Vacuum Science & Technology B: Microelectronics and Nanometer Structures* **17**, doi:10.1116/1.590839 (1999).

48. Pintilie, L., Vrejoiu, I., Hesse, D. & Alexe, M. The influence of the top-contact metal on the ferroelectric properties of epitaxial ferroelectric $Pb(Zr_{0.2}Ti_{0.8})O_3$ thin films. *Journal of Applied Physics* **104**, doi:10.1063/1.3021293 (2008).

49. Ramesh, R. *et al.* Fatigue and retention in ferroelectric Y-Ba-Cu-O/Pb-Zr-Ti-O/Y-Ba-Cu-O heterostructures. *Applied Physics Letters* **61**, 1537-1539, doi:10.1063/1.107488 (1992).

50. Wang, X., Liu, J., Bai, W. & Kwong, D. L. A Novel MONOS-Type Nonvolatile Memory Using High-k Dielectrics for Improved Data Retention and Programming Speed. *IEEE Transactions on Electron Devices* **51**, 597-602, doi:10.1109/ted.2004.824684 (2004).

51. Zhu, H. *et al.* Design and Fabrication of Ta2O5 Stacks for Discrete Multibit Memory Application. *IEEE Transactions on Nanotechnology* **12**, 1151-1157, doi:10.1109/tnano.2013.2281817 (2013).

Chapter 5*

Untying bulk and interface photovoltaic effects

This chapter attempts to untie the entangled interface and bulk photovoltaic effects in vertical $BiFeO_3$ capacitors exploiting linearly polarized lights. It is demonstrated that single ferroelectric domain $BiFeO_3$ exhibits two competitive photo-induced phenomena. Namely, anisotropic photoabsorption and bulk photovoltaic effects. More specifically, illuminated by in-gap photon energies, the interface band-bending photovoltaic effects dominates the photovoltaic output in $BiFeO_3$ which is evidenced by the angular dependence originating from the anisotropic absorption. On the other hand, bulk photovoltaic action dominates the photovoltaic response upon illumination by above-bandgap laser (405 nm). This chapter demonstrates distinguishing the two aforementioned photovoltaic effects which is of great importance to unlock the potential of the ferroelectric photovoltaic effect.

*This section published substantially as Yiqi Hu, Amr Abdelsamie, et al., Effect of polarization rotation on the optical and photovoltaic properties of $BiFeO_3$ thin films, **2021** J. Phys.: Condens. Matter 33 354002, DOI: 10.1088/1361-648X/ac0d19.

5.1 Introduction

It is well-established that Schottky barrier forms at ferroelectric/metal interfaces.[1-3] This built-in electric field assists in the separation of photogenerated electron-hole pairs. Additionally, such interface-induced ferroelectric photovoltaic effect is switchable following the polarization reversal.[4-6] On the other hand, ferroelectrics manifest themselves as noncentrosymmetric materials by exhibiting bulk photovoltaic effects (BPVE). That is, the separation of the photoexcited charge carriers in the bulk of the homogeneous crystals upon illuminated by above-bandgap light.[7-9] Similarly, bulk PV is switchable since the crystal asymmetry can be switched by external electric fields in ferroelectrics. Hence, the two phenomena are likely to coexist in the same material system making it challenging to disentangle the effects. It was concluded in chapter 4 that ferroelectric photovoltaic effects under white light is dominated by the interface band-bending. However, a signature of bulk photovoltaic effect was detected in thicker $BiFeO_3$ films evidenced by the enhanced open-circuit voltage, although a strong evidence of its contribution to the total photocurrent, if any at all, is still missing.

One of the distinctive features of the BPVE is the angular dependence of photovoltaic output on the light polarization.[10] Most of the studies have been reported so far are carried out by means of a linearly polarized monochromatic light on noncentrosymmetric crystals with either single crystal[11-13] or thin films with co-planar electrodes[14-17]. In these structures, the role of Schottky barrier is either minimized or totally excluded. On the other hand, interface-based solar cells do not exhibit angular modulation. Consequently, linearly polarized light can be utilized to attempt to distinguish the two phenomena in vertical photovoltaic cells.

The material system centered in this chapter is bismuth ferrite with monodomain ferroelectric structure. $BiFeO_3$ offers a rich platform to investigate the ferroelectric photovoltaic. When grown with $(001)_{pc}$ orientation, it exhibits two ferroelectric polarization components, namely, out-of-plane component (towards $[001]_{pc}$) and in-plane component (to $[110]_{pc}$). Interestingly, by gradual aliovalent doping of BFO, the total

polarization progressively rotates towards c-axis. However, at the morphotropic phase boundary, for example 20% lanthanum doping, a mixture of "polar" rhombohedral and "nonpolar" orthorhombic phases exist in the same crystal.[18] This offers a tunable crystal system providing additional degree of freedom to explore ferroelectric PV. On the other hand, and as described in chapter 2, $BiFeO_3$ was found to exhibit anisotropic absorption under linearly polarized light which originates from its polar nature.[19,20] Consequently, there exist two potential competing/cooperating photo-induced anisotropies in $BiFeO_3$, i.e., bulk photovoltaic and anisotropic absorption.

In this chapter, linearly polarized light is exploited to study its interaction with the photoferroelectric $(001)_{pc}$-$BiFeO_3$. White light and below-bandgap (520 nm) and above-bandgap (405 nm) lasers are exploited to explore the photovoltaic effects and anisotropic absorption in vertical capacitors. Upon illumination of $BiFeO_3$ by below bandgap light (520 nm), bulk photovoltaic effect is absent. This is verified by the emergence of anisotropic absorption which can be, thus, correlated with the interface band-bending driven photovoltaic effects. Also, the predomination of bulk photovoltaic effects under 405 nm (3.1 eV) laser source is confirmed by comparing the experiment and theory. The results provide new insights on the competitive bulk photovoltaic and anisotropic absorption in $(001)_{pc}$-oriented $BiFeO_3$.

5.2 Light polarization-dependent photovoltaic performance: white light

In this section, the dependence of the photovoltaic output on light polarization is studied in vertical-type ferroelectric photovoltaic cells. For this purpose, a linearly polarized white light is adopted to excite monodomain $BiFeO_3$ thin films sandwiched between platinum and $La_{0.7}Sr_{0.3}MnO_3$. In order to develop a further insight into photovoltaic performance, the crystal symmetry of $BiFeO_3$ is tailored towards the morphotropic phase boundary via lanthanum doping. Current-voltage curves were collected in both up- and down ferroelectric polarization states. Eventually, the experimental data are compared to the calculated bulk photovoltaic.

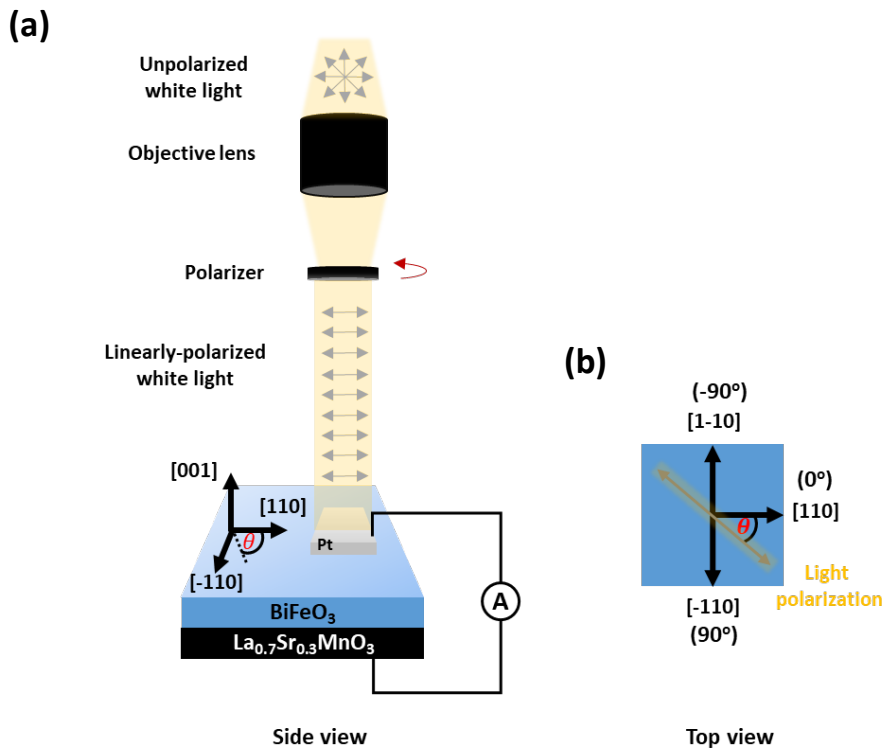

Figure 5.1: Illustration of the orientation of $BiFeO_3$-based photovoltaic cell with respect to the light polarization. In **(a)** Incoming white light propagates along z-direction through an objective lens before being linearly polarized by Glan-Thomson calcite-type polarizer. The sample is being rotated to the targeted azimuthal angle θ. Additionally, the in-plane ferroelectric polarization, along $[110]_{pc}$, is taken as a reference such that $\theta=0^o$ at which light polarization is parallel to the in-plane ferroelectric polarization **(b)**.

Pt/(120nm) BFO/LSMO, or 120-BFO, sample was initially used to study the dependence of the photovoltaic performance on the light polarization of intensity of 20 mW/cm^2. Prior to the PV measurements, the sample is poled in up- and down- ferroelectric polarization directions. Afterwards, a linear Glan-Thomson calcite polarizer was placed between the sample surface and the focusing lens to illuminate the sample through the top electrode (Pt) as depicted in Figure 5.2 (a). In the schematic illustration shown in Figure 5.1 (b), the light polarization makes an angle θ relative to the in-plane ferroelectric polarization of BFO, i.e., $[110]_{pc}$. Hence, $\theta=0^o$ is defined at which light polarization is parallel to the in-plane ferroelectric polarization. The out-of-plane photovoltaic behavior was measured for different azimuthal orientations of the light polarization as shown in Figure 5.2.

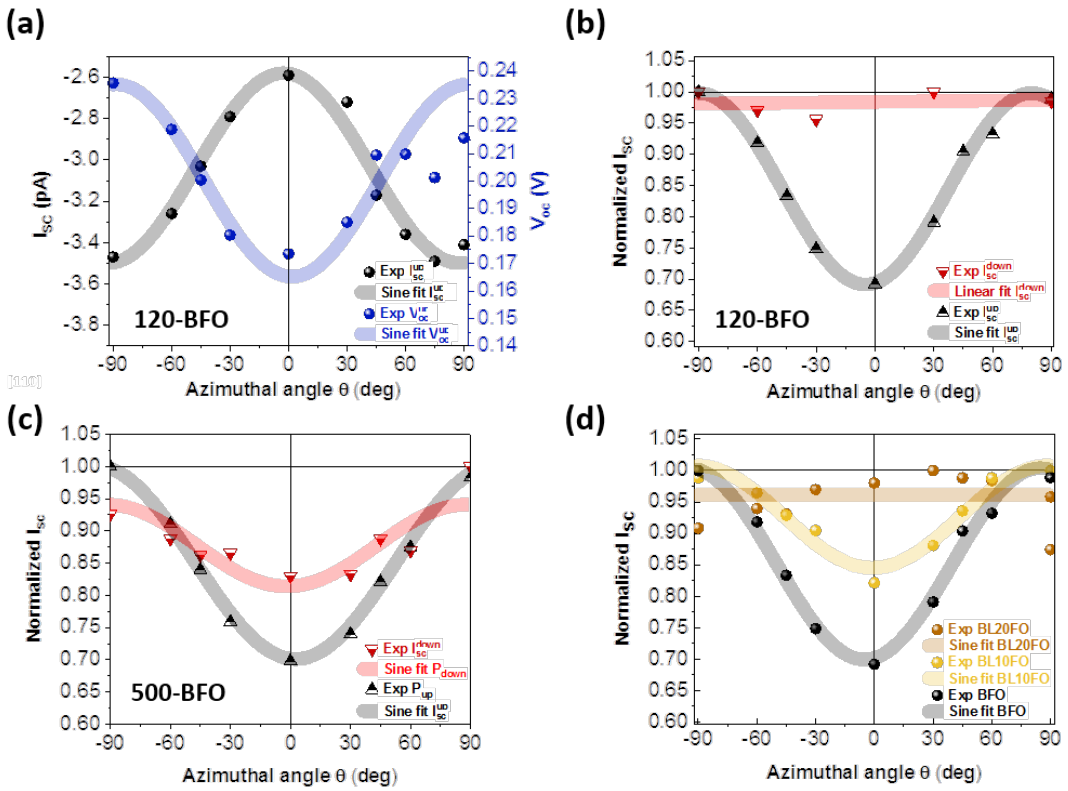

Figure 5.2: Modulation of photovoltaic performance in vertical $BiFeO_3$ heterostructures with light polarization. **(a)** Sinusoidal signal of the short-circuit current (black) and open-circuit voltage (blue) in 120-BFO sample in up-polarization state. **(b)** Normalized I_{SC} versus polarization angle in the same sample measured in up- (black) and down (red) ferroelectric polarizations. **(c)** Normalized I_{SC} in 500-BFO sample measured in up- and down ferroelectric polarization. **(d)** Tuning the crystal symmetry of BFO via lanthanum doping led to notable change in the modulation behavior in I_{SC}.

Figure 5.2 (a) reveals the modulation of the photovoltaic output measured in 120-BFO heterostructures in up-polarization state. The absolute photocurrent and photovoltage exhibit angular dependence with their maxima at θ = 90° and minima at θ = 0°. More precisely, the PV is minimized (maximized) when the light polarization is set parallel (normal) to the in-plane polarization. It is worth noting that both the short-circuit current and open-circuit voltage do not change their sign, i.e., I_{sc}^{up} (V_{oc}^{up}) is negative (positive) for the entire angles range. The more surprising result is that the normalized short-circuit currents (I_{sc}^{up} *and* I_{sc}^{down}) behave differently as presented in Figure 5.2 (b). A peak-to-peak deviation of 30% with respect to the light polarization direction change was observed in

I_{sc}^{up} while I_{sc}^{down} demonstrates a negligible modulation. More intriguingly, a similar angular dependence is measured in ferroelectric cell based on thicker (500 nm) BFO in P_{up} Figure 5.2 (c). However, in difference with PV measured in 120-BFO, although under the same illumination conditions, I_{sc}^{down} (500-BFO) demonstrates a pronounced sinusoidal behavior yielding ~17% variation.

The above-mentioned results show that the linearly polarized light largely influenced the photovoltaic performance. To further elaborate on this, the correlation between $BiFeO_3$ crystal symmetry and current modulation with angle was examined. In this regard, a series of Pt/$Bi_{1-x}La_xFeO_3$/LSMO samples were employed where x= 0, 0.1 and 0.2 and denoted as BFO, BL10FO and BL20FO, respectively. In fact, lanthanum substitutes Bi in BFO resulting in reduced in-plane polarization component which ultimately vanishing at the morphotropic phase boundary (in BL20FO).[21-23] The findings are set out in Figure 5.2 (d) showing a decrease of the deviations from 30% (in Pure BFO) to 15% (in BL10FO) to almost a scattered behavior in BL20FO. This combination of results indicates a strong correlation between the light polarization and the in-plane ferroelectric polarization of BFO. However, further analysis is required.

It is interesting to mention that Schottky barrier-based solar cells do not exhibit any angular dependence with the light polarization.[24] It should be emphasized again that $BiFeO_3$ with single ferroelectric domain is used in PV devices which excludes any contribution from local noncentrosymmetry at domain walls. At a glance, such anisotropy in photovoltaic behavior might suggest a considerable contribution from the bulk photovoltaic effect. Obviously, testing the bulk photovoltaic theory in $BiFeO_3$ is desirable in order to compare to the experimental results.

5.2.1 Tensor calculation of the bulk photovoltaic effect

It is established that bulk photovoltaic effect is described by tensor of third rank order.[25,26] In other words, the photovoltaic response can be modulated under linearly polarized light.

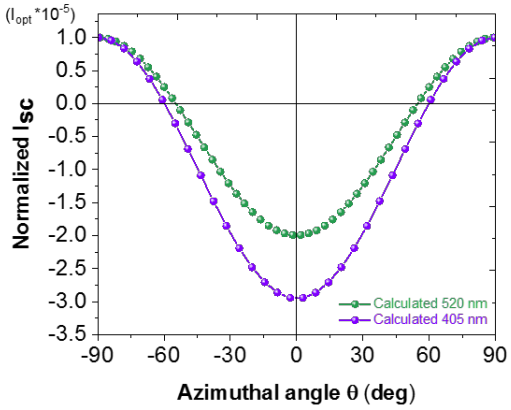

Figure 5.3: Calculated out-of-plane bulk photocurrent in monodomain (001)-oriented $BiFeO_3$ at different azimuthal angles in up- ferroelectric polarization state. The calculations were carried out for 405 nm (3.1eV) and 520 nm (2.4 eV) wavelengths. The generated photocurrents under both lights are in phase with different amplitudes.

To put it more, when linearly polarized light is incident on a noncentrosymmetric crystal, the generated photocurrent is given by:

$$J_i = I_{opt}\beta_{ijk}e_j e_k \qquad (5.1)$$

where I_{opt} is the light intensity, β_{ijk} is a third-rank bulk photovoltaic tensor and e_j and e_k are the projections of light polarization vector. More specifically, in this work, the light propagates along z-axis to the surface of monodomain (001)-$BiFeO_3$ thin film (space group of *R3c*) giving rise to a photocurrent:

$$J_i = I_o \begin{pmatrix} 0 & 0 & 0 & 0 & \beta_{15} & -\beta_{22} \\ -\beta_{22} & \beta_{22} & 0 & \beta_{15} & 0 & 0 \\ \beta_{31} & \beta_{31} & \beta_{33} & 0 & 0 & 0 \end{pmatrix} \begin{pmatrix} e_1^2 \\ e_2^2 \\ 0 \\ 0 \\ 0 \\ 2e_1e_2 \end{pmatrix} \qquad (5.2)$$

For the sake of consistency with experimental measurements, the in-plane ferroelectric polarization is taken as reference. Therefore, the out-of-plane photocurrent can be written as:

$$J_{[001]} = \frac{I_{opt}}{3\sqrt{3}}\left[-2\beta_{15} - \sqrt{2}\beta_{22} + 2\beta_{31} + \beta_{33}\right] + \frac{I_{opt}}{3\sqrt{3}}\left[-2\beta_{15} + 2\sqrt{2}\beta_{22} - \beta_{31} + \beta_{33}\right]\sin(2\theta + \frac{\pi}{2}) \quad (5.3)$$

Where θ is the angle between the light polarization and in-plane ferroelectric polarization, i.e. $[110]_{pc}$. The current-azimuthal angle relationship represents a sin2θ dependence. Moreover, β_{ijk} values are $BiFeO_3$-specific for a defined illumination light wavelength.

The simulated data using (405 nm) 3.1 eV and (520 nm) 2.4 eV lights revealed sinusoidal curves presented in figure 5.3. Here, the β_{ijk} values were extracted from experimental work on $BiFeO_3$ with co-planar configurations, i.e., from purely measured bulk photocurrents as listed in Table 5..[8] As the figure points out, the calculated photocurrent has negative sign at $[110]_{pc}$ while the amplitude flips its polarity along directions normal to the in-plane ferroelectric polarization. Also, the photocurrent at θ=0 is around larger in magnitude than that at 90°. More interestingly, both 405 nm- and 520 nm-induced photocurrents are in phase in which 520 nm is smaller in amplitude. Apparently, the bulk photovoltaic theory and experiment do not match if one compares Figure 5. (a) and Figure 5.3 which leaves this part inconclusive.

Table 5.1: Bulk photovoltaic tensor elements of $BiFeO_3$ at 405 nm (3.1 eV) and 520 nm (2.4 eV)

	β_{15} (V^{-1})	β_{22} (V^{-1})	β_{31} (V^{-1})	β_{33} (V^{-1})
405 nm (3.1 eV)	8.1×10^{-5}	-1.1×10^{-5}	6.4×10^{-5}	-1.1×10^{-4}
520 nm (2.4 eV)	3.0×10^{-6}	-4.4×10^{-7}	1.6×10^{-6}	-4.4×10^{-6}

The discrepancy between the calculated and experimental results could be due to the fact that the governing mechanism of the photocurrent modulation in BFO-based devices is not the BPVE. This discrepancy could be a consequence of dominant role played by Schottky barrier-induced photovoltaic effect. Rather, the spatial anisotropy in one of the photovoltaic elementary processes, namely, light absorption or carriers transport can be correlated with

the results. However, the absorption anisotropy may have played a significant role here similar to the case of noncentrosymmetric semiconductors.[24] The imaginary part of the dielectric constant ε_2 of $BiFeO_3$ was shown to exhibit an anisotropic behavior in the visible range.[19,27] Therefore, polarization-dependent-absorption coefficient in monodomain BFO films were explored in next section by means of UV-vis spectrophotometer.

5.3 Light polarization-dependent absorption properties

The optical absorption properties of $BiFeO_3$ films are determined by means of Perkin Elmer Lambda 950 UV-vis spectrophotometer. $BiFeO_3$ films (170 nm) were directly grown on double-side-polished $SrTiO_3$ substrates ensuring transparency. Again, STO substrates' surfaces were offcut by 4° along $[110]_{pc}$ to obtain single ferroelectric domain structures. In this section, the absorption properties are firstly measured by means of unpolarized light. Further, the absorption coefficients modulated by linearly-polarized light are introduced. All curves were collected for wavelengths 400 nm to 600 nm at room temperatures. It should be noted that it is meaningless to collect data for wavelengths shorter than 400 nm due to substrate absorption.

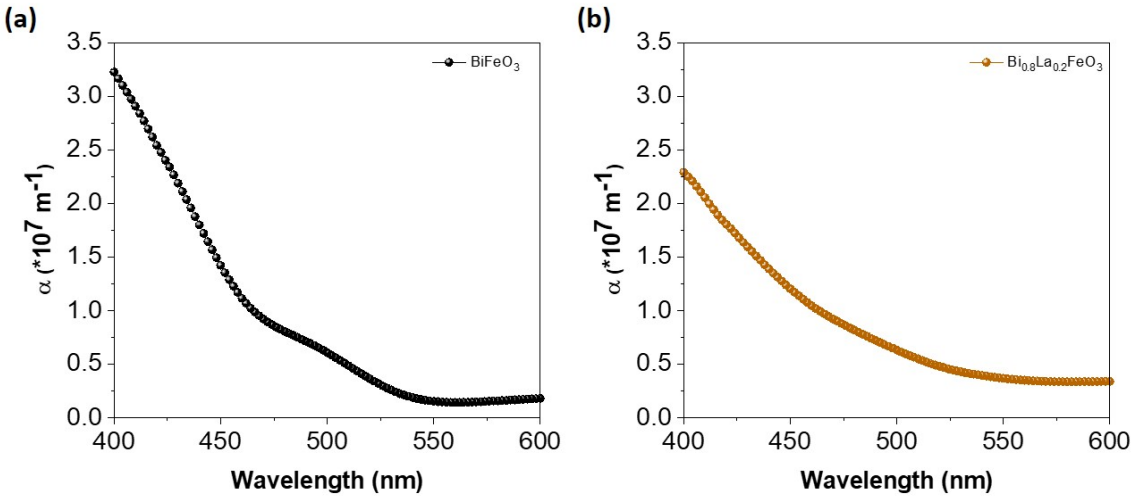

Figure 5.4: Absorption coefficients of 170 nm $BiFeO_3$ **(a)** and $Bi_{0.8}La_{0.2}FeO_3$ **(b)** grown on transparent $SrTiO_3$ and measured by UV-vis spectrophotometer.

The optical absorption coefficient α of $BiFeO_3$ (black) is measured by unpolarized light and compared to 170 nm $Bi_{0.8}La_{0.2}FeO_3$ (orange) as presented in Figure 5.4 (a) and (b). Note that $Bi_{0.8}La_{0.2}FeO_3$ possesses a mixture of rhombohedral (polar)/orthorhombic (nonpolar) crystal structure. The data were deduced from absorbance spectra after removing contributions from STO substrate. BFO spectrum displays a small shoulder centered at 490 nm (~2.53 eV) BFO. However, this shoulder is smeared in case of BL20FO film. Although both absorption spectra show different features, both films exhibit optical absorption onset at 560 nm (~2.2 eV). This is suggested as charge transfer dipole-forbidden *p-d* transition.[19,28] However, further analysis is presented in the coming paragraphs.

Absorption properties of pure- and lanthanum-doped bismuth ferrite films are further

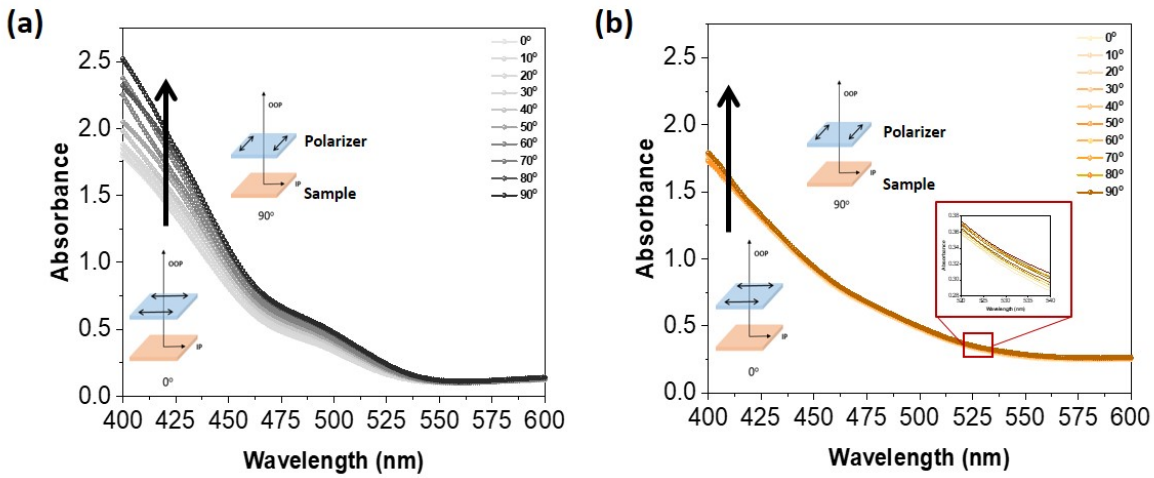

Figure 5.5: Polarized absorption spectra of $BiFeO_3$ **(a)** and $Bi_{0.8}La_{0.2}FeO_3$ **(b)** thin films. The absorption spectra were collected from -90° to 90°.

investigated under linearly polarized light. For this purpose, the spectrometer was equipped by Glan-Thomson calcite-type polarizer (resembling the one used to measure the photovoltaic performance presented in previous section). Moreover, the sample is mounted on a rotatable stand to enable rotation from -90° to 90° while ensuring constant light intensities. Figure 5.5 displays the light polarization-dependent absorption of BFO and BL20FO in the range 0° to 90°. The plots show different absorption behaviors which require more analysis revealing the direct and indirect bandgaps as well as the angle-dependent absorptions.

Absorption coefficient spectra presented in this section are contributed by both direct and indirect bandgaps. The optical bandgap can be determined using Tauc method following the relation:

$$\alpha h\nu = A(h\nu - E_g)^n \quad (5.4)$$

where A is constant, hν is photon energy, E_g is materials bandgap and n determines the type of bandgap. To extract the direct and indirect bandgaps, n is set to 1/2 and 2, respectively. Then, figure of $(\alpha h\nu)^{1/n}$ versus hν are plotted allowing extraction of the aimed bandgap by linear extrapolating to $\alpha h\nu = 0$.[29] It is worth noting that the indirect bandgap plot should demonstrate a two-linear regimes corresponding to emitted/absorbed phonons.[30]

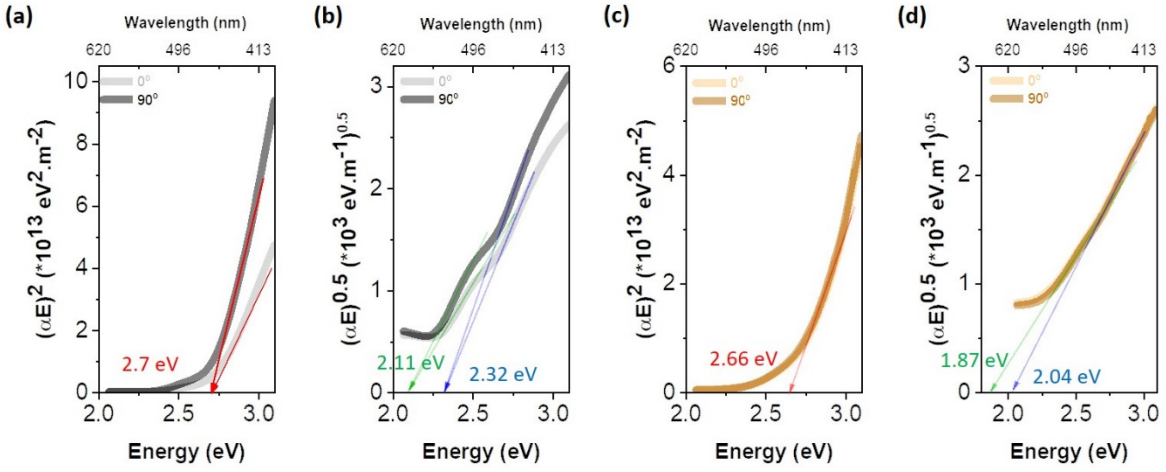

Figure 5.6: Tauc plots indicating the direct and indirect bandgaps for $BiFeO_3$ **(a)** and **(b)** and $Bi_{0.8}La_{0.2}FeO_3$ **(c)** and **(d)**. The extracted bandgaps show the same value for the two orthogonal directions in both samples.

Figure 5.6 (a) and (b) plots square and square root of αhν versus hν for $BiFeO_3$ and $Bi_{0.8}La_{0.2}FeO_3$ at which light polarization is aligned 0° and 90° with respect to the ferroelectric polarization. In case of $BiFeO_3$, the linear extrapolation leads to direct bandgap of 2.7 eV (~460 nm) for both directions as shown in Figure 5.6 (a). In case of $Bi_{0.8}La_{0.2}FeO_3$, the first direct transition for both axes is observed at 2.66 eV (~466)

indicating a redshift of 40 meV relative to pure BFO. These results are in good agreement with previous reports.[18,19]

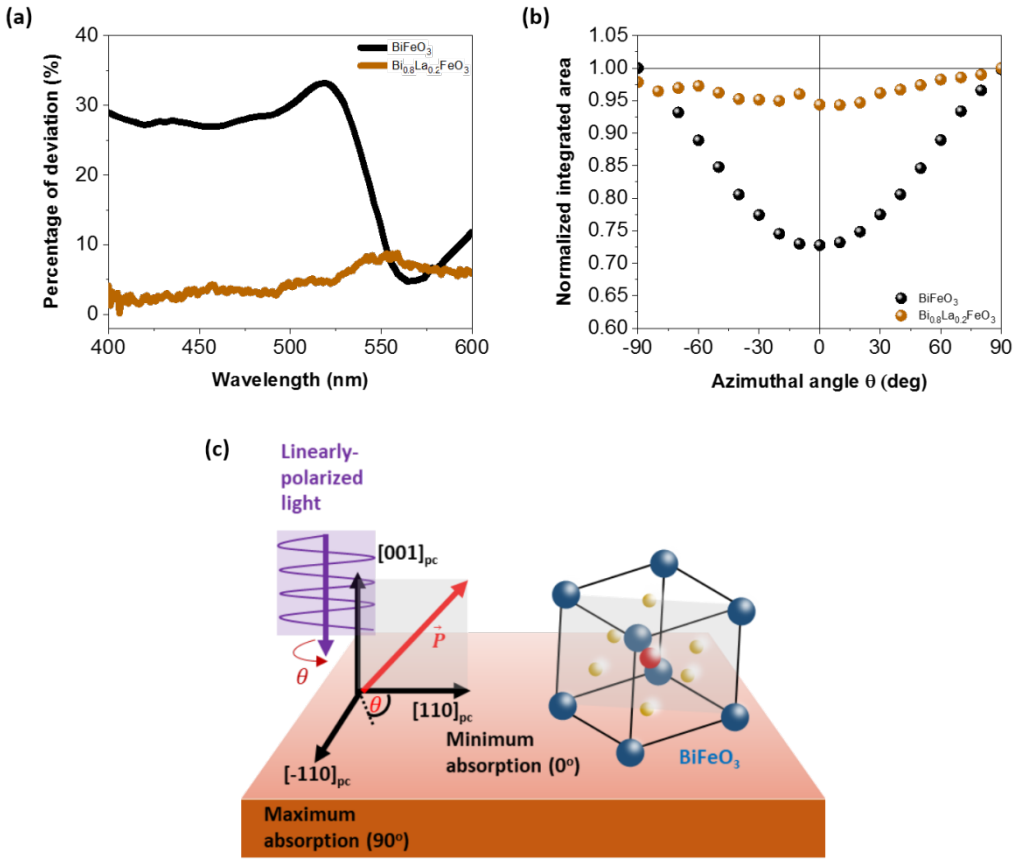

Figure 5.7: Anisotropic light absorption in $BiFeO_3$ and $Bi_{0.8}La_{0.2}FeO_3$. **(a)** Wavelength-dependent percentage of deviation in light absorption between two orthogonal light polarizations. **(b)** Normalized integrated areas under the absorption curves from 400 nm to 600 nm as a function of the polarization angle. **(c)** Schematic illustrating the anisotropy in absorption in $BiFeO_3$ unit cell.

On the other hand, $(\alpha h\nu)^{1/2}$ versus hν exhibit two linear regimes in both compounds. For $BiFeO_3$, the first transition located at 2.32 eV (~535 nm) which is likely assigned to presence of defect states such as oxygen vacancies.[19,31,32] Moreover, there exists an optical transition at 2.11 eV (~590 nm) that originates from $t_{1g}(\pi) \rightarrow t_{2g}$ dipole-forbidden charge transfer transition.[33] For $Bi_{0.8}La_{0.2}FeO_3$, two transitions are recognized, namely, 2.04 eV (~608 nm) and 1.87 eV (~663 nm). Once more, the two transitions are redshifted with

respect to $BiFeO_3$. Having established the major optical transitions in $BiFeO_3$ and $Bi_{0.8}La_{0.2}FeO_3$, it is worth to extract the absorption anisotropies.

At a glance, Figure 5.5 points out different anisotropic absorption behaviors in $BiFeO_3$ and $Bi_{0.8}La_{0.2}FeO_3$ which is worth further analysis. As shown in Figure 5.7 (a), and by extracting the percentage of deviation between the minimum and maximum absorptions, given by $\alpha(90^o) - \alpha(0^o)/\alpha(90^o)$, the result is positive value over the whole measured wavelength range. This indicates that the absorption is maximized at which the light and ferroelectric polarizations are orthogonal while minimum at parallel. For BFO, the percentage of deviation peaks at 518 nm (33.3%) and minimized at 565 nm (4.5%) while for BL20FO, ranging from 0.2% to maximum 9% at 550 nm. Furthermore, the angle-dependent integrated area under the absorption curves in Figure 5.7 (b) demonstrates white light absorption anisotropy in BFO (percentage of deviation ~28%) while BL20FO exhibits around 5%.

This concludes the polarization-dependent measurements as follows; when the white light polarization is set along (001)-oriented BFO $[110]_{pc}$, the optical absorption in BFO is minimized. The optical excitation increases as the azimuthal angle enlarged and the strongest absorption occurs at light polarization is perpendicular to the $[110]_{pc}$. This further confirms the optical anisotropy that single domain BFO exhibits giving rise to such linear dichroism behavior. In contrary, BL20FO possesses polar/nonpolar phases lead to reduction of the linear dichroism. The experimental anisotropic absorption findings here are consistent with the calculated band structure of BFO (R3c).[34,35] The anisotropy of effective mass of electrons along different directions tends to induce different optical excitations under different light polarizations.

5.4 Photovoltaic effects under linearly polarized lasers: photon energy dependence

In order to clarify the discrepancy found in the photovoltaic response measured under white light, photovoltaic measurements were further performed on (500 nm) BFO film using

linearly polarized lasers. Here, lasers of wavelengths 650 nm (hν=1.9 eV), 520 nm (2.4 eV) and 405 nm (3.1 eV) and 50 mW power were employed. All the results are presented in Figure 5.8 in down- and up ferroelectric polarization states and compared to the white light illumination. Photovoltaic output is maximum in case of 520 nm lightening, while no photovoltaic response was detected under 650 nm illumination. This is reasonable since light with 650 nm wavelength is below the absorption edge revealed by the absorption measurements on BFO. Moreover, it is obvious that the photovoltaic effects are found switchable confirming its ferroelectric origin. Next, the angular-dependent photocurrents are measured under 520 nm and 405 nm and compared to the results presented in Figure 5..

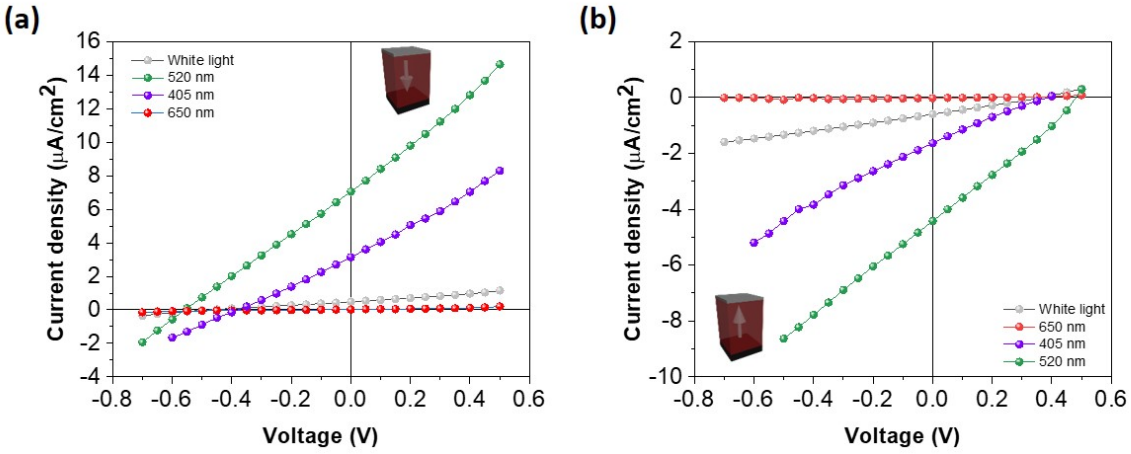

Figure 5.8: Photovoltaic output under monochromatic light compared to white light. Light current density-voltage in **(a)** Down polarization state and **(b)** Up polarization state.

Figure 5.9 presents the modulation of the photocurrents with the azimuthal angle (from -90° to +90°) in BFO film under 520 nm (in green) and 405 nm (in purple). The photocurrents were collected following the sample poling to down- (Figure 5.9 (a) and (b)) and up- (Figure 5.9 (c) and (d)) polarization states. The results demonstrate significant difference for different light wavelengths.

In down polarization state, positive photocurrents were observed over the whole angle range under both 520 nm and 405 nm lights. However, photocurrent is one order of magnitude larger under 520 nm laser. Figure 5.9 (a) presents the modulation of the

photocurrent under 520 nm which maximizes at θ=90°, -90° (I_{down}~310 pA) while minimizes at θ=0° (I_{down}= 180 pA). In difference, under illumination at 405 nm, the generated photocurrent peaks at θ=-20° as shown in Figure 5.9 (b).

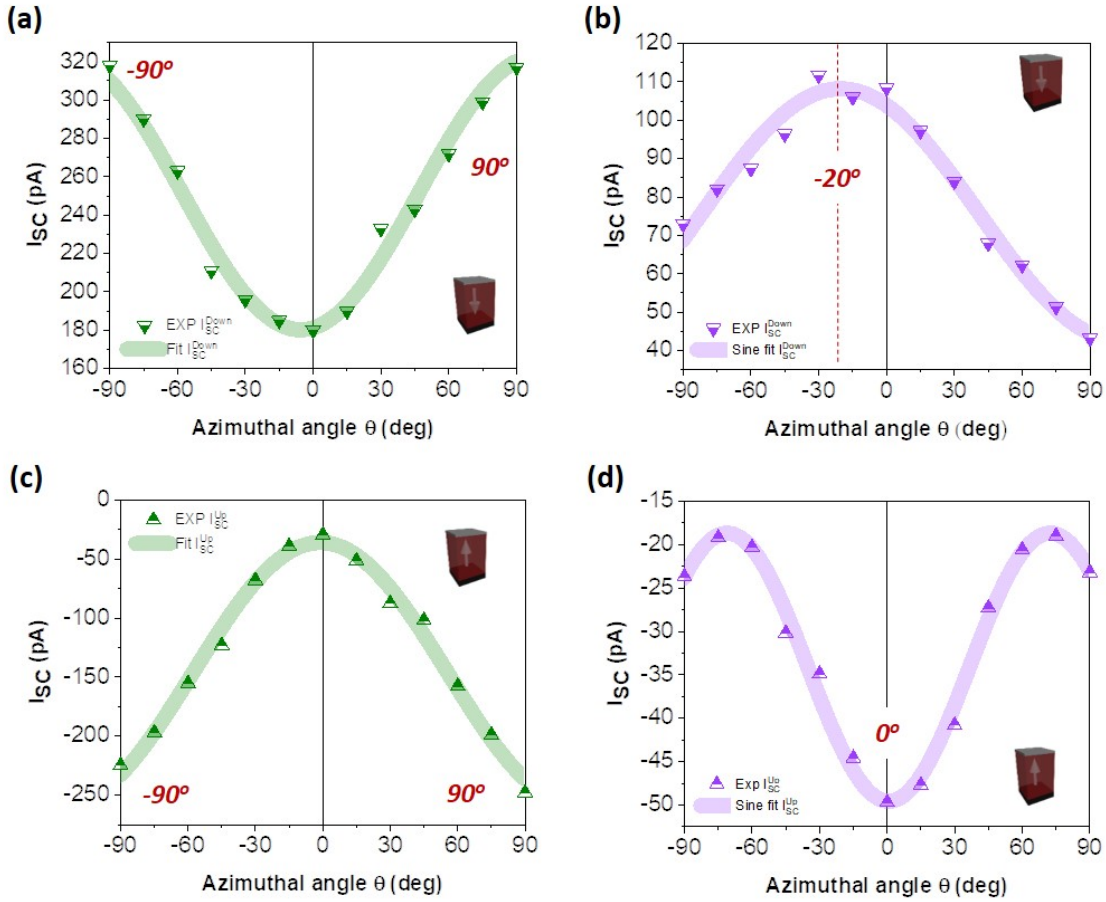

Figure 5.9: Angular dependence of the photocurrents in Pt/BFO/LSMO. **(a)** Short-circuit current under 520 nm illumination in down ferroelectric polarization state. **(b)** I_{SC} under 405 nm illumination in down polarization state. Short-circuit current in up polarization state in illuminated 520 nm **(c)** and 405 nm **(d)** conditions.

Comparing the two results in up polarization state (Figure 5.9 (c) and (d)) demonstrate distinctive features. In case of 520 nm illumination, short-circuit current is -25 pA at θ=0° and increases as the polarization angle increases before maximizing at θ=90° and -90°. In contrary, photocurrent peaks at θ=0° under 405 nm illumination while the minimum value is measured at θ=73° and -73°. It should be noted that under both illumination conditions,

photocurrents flow in negative direction. Apparently, the photovoltaic results observed in this section cannot be interpreted solely by the bulk photovoltaic effects.

5.5 Discussion and summary

The results of this chapter indicate the presence of two competing photo-induced actions in (001)-oriented $BiFeO_3$. In other words, under linearly polarized light illumination, the optical anisotropy and bulk photovoltaic effects tend to coexist. Interestingly, the angular dependences of the calculated bulk photovoltaic and experimental absorption curves are 90^o out-of-phase. In this regard, the purely interface-induced photovoltaic effect would exhibit angular dependence originating from the anisotropic absorption. Consequently, the two phenomena can be distinguished based on this discussion. This section discusses the results of the angular dependences of photocurrents under linearly polarized white light and 520 nm and 405 nm lasers.

First, the experimental photovoltaic output under polarized white light does not stem from bulk photovoltaic. Rather, the anisotropic absorption lies at the origin of the modulated current in which one correlates with the interface photovoltaic effect. This is proved by the trend found in Figure 5.2 (d) that is correlated with the sensitivity of the light absorption to P_{IP} resulting in such scattered behavior in the BL20FO sample. In BFO, there exists an in-plane optical axis parallel to the ferroelectric polarization producing such anisotropic absorption. By doping with 10% La, the optical axis starts to tilt towards the normal to the film surface reducing the effect. At 20% La-doping, the in-plane optical axis disappears and hence a suppressed angular dependence.

Another evidence to the anisotropic absorption-induced current modulation is the distinguished behaviors of I_{sc}^{up} and I_{sc}^{down} shown in Figure 5.2 (b). The results can be interpreted as follows, in P_{up} state, the light suffers from absorption in the bulk of the BFO film before reaching the bottom interface inducing the observed current modulation. It is worthy to note that the bottom interface is of superior quality compared to the top one since it is epitaxially established. In contrary, the top interface is formed after the post-sputtering

of the metal material. Therefore, In P_{down}, a stronger trap-assisted recombination at the top interface could weaken the current modulation. To further elaborate on this, the 500-BFO was investigated as shown in Figure 5.2 (c) which demonstrates stronger angular dependence in case of P_{down} as the absorption gain is larger. This finding confirms the association between the anisotropic absorption driven by the in-plane component of the ferroelectric polarization and the photocurrent modulation. Therefore, it is concluded that the ferroelectric polarization-modulated Schottky barrier is the dominant origin of PV effect in the films. Accordingly, the absorption process is behind the modulated photovoltaic behavior. It has previously been shown that intrinsic optical anisotropies influence the response of optoelectronic devices.[36-39] Interestingly, this qualifies this class of materials as linear dichroism photodetectors. It is now worth to proceed to discuss the impact of photon energy on the overall Photovoltaic behavior of BFO/LSMO heterostructures.

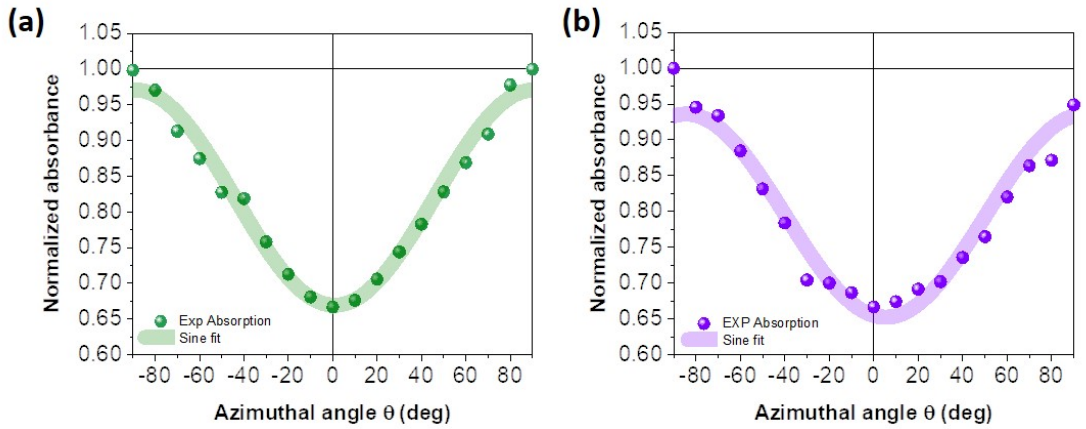

Figure 5.10: Normalized anisotropic absorption in $BiFeO_3$ film as a function of polarization angle at 520 nm **(a)** and 405 nm **(b)** wavelengths. The data are extracted from polarization-dependent absorption curves.

The most confusing finding in this chapter was the dissimilar behaviors of the polarization-dependent of photocurrent under 520 nm and 405 nm lightenings. Note that 520 nm ($h\nu$=2.4 eV) laser below the bandgap of $BiFeO_3$ while above-bandgap excitation is provided by 405 nm ($h\nu$=3.1 eV) as demonstrated by the absorption results in section (5.3).

In order to investigate the role of the anisotropic absorption on the photovoltaic output, the absorbance at 520 nm and 405 nm were extracted from the absorption spectra as shown in Figure 5.10 (a) and (b), respectively. Under optical excitation by the two aforementioned wavelengths, the absorbance has an angular dependence with percentage of deviation around ~33%. This light polarization dependence can be fitted by equation:

$$Absorbance = a + b.sin(2\theta - \frac{\pi}{2})$$

where a, b and c are constants. The absorption is minimized along the in-plane ferroelectric polarization while maximized along the orthogonal direction. Obviously, the photovoltaic performance under 520 nm is different from the bulk photovoltaic theory as shown in figure 5.10.

Under below-bandgap 520 nm (2.4 eV) optical excitation, photovoltaic output is dominated by the band-bending at Pt/$BiFeO_3$ and $BiFeO_3$/ LSMO. This is verified by the polarization-dependent photocurrent is well-fitted by the equation deduced from the anisotropic absorption. Optical structure of $BiFeO_3$ is characterized by self-trapped *p-d* charge transfer excitons. These localized self-trapped excitons exhibit short diffusion lengths which require internal field to dissociate. However, since films used in this study are monodomain, domain walls are excluded as the mechanism of photovoltaic behavior. Solely, the photogenerated excitons in the proximity of the interfacial region are dissociated by the interface band-bending. In this regard, the absorption process is modulated by the light polarization giving rise to modulated photocurrent.[33,40] Additionally, ferroelectric polarization reversal yields a modulated Schottky barrier which in turn results in switchable photocurrent.

In up-polarization state (see figure 5.9 (d)), although $BiFeO_3$ exhibits strong linear dichroism at 405 nm, optical excitation of vertical Pt/$BiFeO_3$/LSMO capacitor at 405 nm preferentially induces bulk photovoltaic effects, but the interfacial effects still exist. The data can be fitted by:

$$I_{sc} = A + B.\sin(\frac{5}{2}\theta + C)$$

which cannot be simply explained by either the anisotropic absorption or the bulk PV theory. The photocurrent curve is shifted towards the negative which might suggest a considerable contribution from the interface PV. In contrast, in down-state, photocurrent tends to be dominated by the interface effects with less contribution from bulk PV manifested by the shift of the photocurrent curve to -20°. The reason of such discrepancy can be explained as follows. As shown in chapter 5, in down-state where the top interface (Pt/BFO) is activated and directly exposed to the light which allows the interfacial effects. On the other hand, in up-state, the bottom interface (BFO/LSMO) is activated which requires the light to go through the whole film thickness. In this regard, the hole-electron

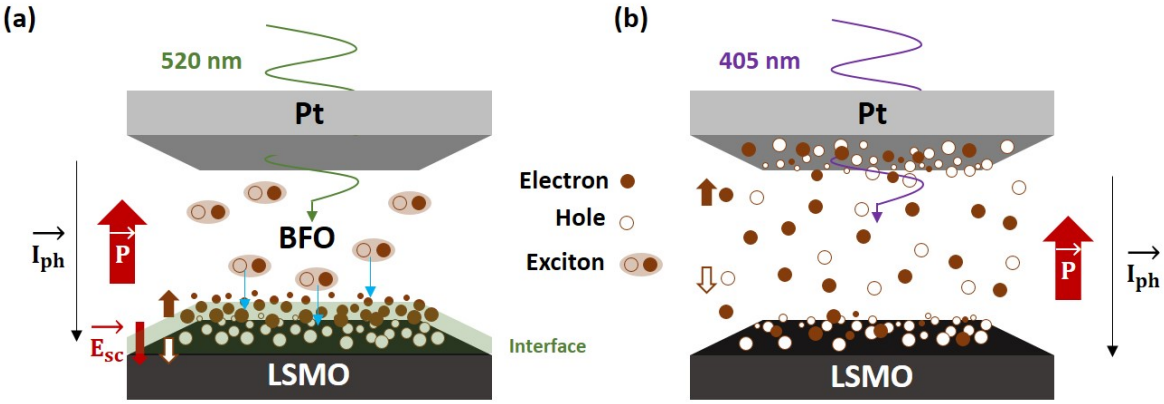

Figure 5.11: Depiction illustrates the origin of interface- and bulk-induced photovoltaic effects in vertical capacitor based on $BiFeO_3$. **(a)** In-gap photon energy produce photovoltaic response originating from the band-bending at BFO/metal interface. Illuminated by 520 nm laser, generated self-trapped exciton in the bulk of BFO which travel to the interface before being separated by Schottky barrier. **(b)** Above-bandgap illumination (405 nm) preferentially generates bulk photovoltaic effects in up ferroelectric polarization state with the interface effect still present. However, in down-state, the interface band-bending comes to the picture again since the top interface is activated and directly exposed to the illuminating light.

separation process is handled by the non-centrosymmetry of $BiFeO_3$, i.e., bulk photovoltaic effect. These findings support the idea that bulk photovoltaic requires band-band transition. Figure 5.11 explains the origin of the origin of interface- and bulk-induced photovoltaic effects in vertical capacitor based on $BiFeO_3$.

In summary, this chapter provides a new understanding of the interaction of linearly polarized light with single-phase ferroelectric absorber in vertical capacitors. On the one hand, $BiFeO_3$ is shown to exhibit uniaxial optical anisotropy which, in turn, induces linear dichroism. On the other hand, bulk photovoltaic effect is calculated to modulate the photocurrent with sin2θ dependence. It is established that both phenomena give rise to distinguishable sinusoidal angular dependences with 90^o phase difference. In this work, this property allowed to differentiate the interface-induced photovoltaic effects from bulk effects. Illumination by in-gap photon energies witnesses the absence of bulk photovoltaic effects. On the other hand, bulk photovoltaic emerges upon illumination by above-bandgap light (405 nm). However, the interface band-bending-driven photovoltaic action is still present. In addition, illuminated by white light, $BiFeO_3$-based photovoltaic cell is dominated by interface band-bending.

References

1. Blom, P. W., Wolf, R. M., Cillessen, J. F. & Krijn, M. P. Ferroelectric Schottky diode. *Phys Rev Lett* **73**, 2107-2110, doi:10.1103/PhysRevLett.73.2107 (1994).

2. Pintilie, L. & Alexe, M. Metal-ferroelectric-metal heterostructures with Schottky contacts. I. Influence of the ferroelectric properties. *Journal of Applied Physics* **98**, doi:10.1063/1.2148622 (2005).

3. Pintilie, L. *et al.* Metal-ferroelectric-metal structures with Schottky contacts. II. Analysis of the experimental current-voltage and capacitance-voltage characteristics of $Pb(Zr,Ti)O_3$ thin films. *Journal of Applied Physics* **98**, doi:10.1063/1.2148623 (2005).

4. Tan, Z. *et al.* Thinning ferroelectric films for high-efficiency photovoltaics based on the Schottky barrier effect. *NPG Asia Materials* **11**, doi:10.1038/s41427-019-0120-3 (2019).

5. Guo, R. *et al.* Non-volatile memory based on the ferroelectric photovoltaic effect. *Nat Commun* **4**, 1990, doi:10.1038/ncomms2990 (2013).

6. Lee, D. *et al.* Polarity control of carrier injection at ferroelectric/metal interfaces for electrically switchable diode and photovoltaic effects. *Physical Review B* **84**, 125305, doi:10.1103/PhysRevB.84.125305 (2011).

7. Ming-MinYang, Zheng-DongLuo, Kim, D. J. & Alexe, M. Bulk photovoltaic effect in monodomain $BiFeO_3$ thin films. *Applied Physics Letters* **110**, 183902, doi:10.1063/1.4983032 (2017).

8. Matsuo, H., Noguchi, Y. & Miyayama, M. Gap-state engineering of visible-light-active ferroelectrics for photovoltaic applications. *Nature communications* **8**, 1-8 (2017).

9. Spanier, J. E. *et al.* Power conversion efficiency exceeding the Shockley–Queisser limit in a ferroelectric insulator. *Nature Photonics* **10**, 611-616, doi:10.1038/nphoton.2016.143 (2016).

10. Fridkin, V. M. Bulk photovoltaic effect in noncentrosymmetric crystals. *Crystallography Reports* **46**, 654-658, doi:10.1134/1.1387133 (2001).

11. Choi, T., Lee, S., Choi, Y. J., Kiryukhin, V. & Cheong, S.-W. Switchable Ferroelectric Diode and Photovoltaic Effect in $BiFeO_3$. *Science* **324**, 63-66, doi:10.1126/science.1168636 (2009).

12. Festl, H. G., Hertel, P., Krätzig, E. & von Baltz, R. Investigations of the Photovoltaic Tensor in Doped $LiNbO_3$. *physica status solidi (b)* **113**, 157-164, doi:10.1002/pssb.2221130115 (1982).

13. Fridkin, V. M. Parity nonconservation and bulk photovoltaic effect in a crystal without symmetry center. *IEEE Trans Ultrason Ferroelectr Freq Control* **60**, 1551-1555, doi:10.1109/TUFFC.2013.2734 (2013).

14. Ji, W., Yao, K. & Liang, Y. C. Evidence of bulk photovoltaic effect and large tensor coefficient in ferroelectric $BiFeO_3$ thin films. *Physical Review B* **84**, doi:10.1103/PhysRevB.84.094115 (2011).

15. Matsuo, H. *et al.* Bulk and domain-wall effects in ferroelectric photovoltaics. *Physical Review B* **94**, doi:10.1103/PhysRevB.94.214111 (2016).

16. Kim, D. J. & Alexe, M. Bulk photovoltaic effect in monodomain $BiFeO_3$ thin films. *Applied Physics Letters* **110**, doi:10.1063/1.4983032 (2017).

17. Matsuo, H., Noguchi, Y. & Miyayama, M. Gap-state engineering of visible-light-active ferroelectrics for photovoltaic applications. *Nat Commun* **8**, 207, doi:10.1038/s41467-017-00245-9 (2017).

18. You, L. *et al.* Enhancing ferroelectric photovoltaic effect by polar order engineering. *Science advances* **4**, eaat3438 (2018).

19. Schmidt, D., You, L., Chi, X., Wang, J. & Rusydi, A. Anisotropic optical properties of rhombohedral and tetragonal thin filmBiFeO3phases. *Physical Review B* **92**, doi:10.1103/PhysRevB.92.075310 (2015).

20. Choi, S. G. *et al.* Optical anisotropy and charge-transfer transition energies in $BiFeO_3$ from 1.0 to 5.5 eV. *Physical Review B* **83**, doi:10.1103/PhysRevB.83.100101 (2011).

21. González-Vázquez, O. E., Wojdeł, J. C., Diéguez, O. & Íñiguez, J. First-principles investigation of the structural phases and enhanced response properties of the $BiFeO_3$-$LaFeO_3$ multiferroic solid solution. *Physical Review B* **85**, doi:10.1103/PhysRevB.85.064119 (2012).

22. Cheng, C.-J., Kan, D., Anbusathaiah, V., Takeuchi, I. & Nagarajan, V. Microstructure-electromechanical property correlations in rare-earth-substituted $BiFeO_3$ epitaxial thin films at morphotropic phase boundaries. *Applied Physics Letters* **97**, doi:10.1063/1.3520642 (2010).

23. You, L. *et al.* Enhancing ferroelectric photovoltaic effect by polar order engineering. *Science Advances* **4**, eaat3438, doi:10.1126/sciadv.aat3438 (2018).

24. Bube, R. H. *Photoconductivity of solids*. (J. Wiley and Sons, 1960).

25. Fradkin, V. & Magomadov, R. Anomalous photovoltaic effect in $LiNbO_3$:Fe in polarized light. *JETP Letters* **30**, 686-688 (1979).

26. Fridkin, V. M. *Photoferroelectrics*. (Springer Berlin Heidelberg, 2012).

27. Choi, S. G. *et al.* Optical anisotropy and charge-transfer transition energies in $BiFeO_3$ from 1.0 to 5.5 eV. *Physical Review B* **83**, doi:10.1103/PhysRevB.83.100101 (2011).

28. Pisarev, R. V., Moskvin, A. S., Kalashnikova, A. M. & Rasing, T. Charge transfer transitions in multiferroic $BiFeO_3$ and related ferrite insulators. *Physical Review B* **79**, doi:10.1103/PhysRevB.79.235128 (2009).

29. Pankove, J. Optical processes in semiconductors Prentice-Hall. *New Jersey* **92** (1971).

30. Johnson, E. J. in *Semiconductors and Semimetals* Vol. 3 (eds R. K. Willardson & Albert C. Beer) 153-258 (Elsevier, 1967).

31. Wang, H., Zheng, Y., Cai, M.-Q., Huang, H. & Chan, H. L. W. First-principles study on the electronic and optical properties of $BiFeO_3$. *Solid State Communications* **149**, 641-644, doi:https://doi.org/10.1016/j.ssc.2009.01.023 (2009).

32. Clark, S. J. & Robertson, J. Energy levels of oxygen vacancies in $BiFeO_3$ by screened exchange. *Applied Physics Letters* **94**, 022902, doi:10.1063/1.3070532 (2009).

33. Pisarev, R. V., Moskvin, A. S., Kalashnikova, A. M. & Rasing, T. Charge transfer transitions in multiferroic $BiFeO_3$ and related ferrite insulators. *Physical Review B* **79**, 235128, doi:10.1103/PhysRevB.79.235128 (2009).

34. Shenton, J. K., Bowler, D. R. & Cheah, W. L. Influence of crystal structure on charge carrier effective masses in
$BiFeO_3$. *Physical Review B* **100**, doi:10.1103/PhysRevB.100.085120 (2019).

35. He, C. *et al.* Inorganic photovoltaic cells based on $BiFeO_3$: spontaneous polarization, lattice matching, light polarization and their relationship with photovoltaic performance. *Phys Chem Chem Phys* **22**, 8658-8666, doi:10.1039/d0cp01176b (2020).

36. Ding, J. *et al.* Polarization-Dependent Optoelectronic Performances in Hybrid Halide Perovskite $MAPbX_3$ (X = Br, Cl) Single-Crystal Photodetectors. *ACS Appl Mater Interfaces* **10**, 845-850, doi:10.1021/acsami.7b13111 (2018).

37. Yang, Y. *et al.* Air-Stable In-Plane Anisotropic $GeSe_2$ for Highly Polarization-Sensitive Photodetection in Short Wave Region. *Journal of the American Chemical Society* **140**, 4150-4156, doi:10.1021/jacs.8b01234 (2018).

38. Yuan, H. *et al.* Polarization-sensitive broadband photodetector using a black phosphorus vertical p–n junction. *Nature Nanotechnology* **10**, 707-713, doi:10.1038/nnano.2015.112 (2015).

39. Liu, F. *et al.* Highly Sensitive Detection of Polarized Light Using Anisotropic 2D ReS2. *Advanced Functional Materials* **26**, 1169-1177, doi:10.1002/adfm.201504546 (2016).

40. Li, Y. *et al.* Nanoscale excitonic photovoltaic mechanism in ferroelectric $BiFeO_3$ thin films. *APL Materials* **6**, doi:10.1063/1.5030628 (2018).

Chapter 6

Conclusions and recommendations

This chapter wraps up the research outcome obtained in this dissertation. In this regard, the main conclusions are summarized. Then, future research directions are suggested in order to follow up the research carries out in this work towards the enhancement of ferroelectric photovoltaic performance. Also, preliminary results obtained on the double perovskite ferroelectric Bi_2FeCrO_6 are presented.

6.1 General discussion

Bulk photovoltaic effect (BPVE) is one of the most striking manifestation of non-linear optical phenomena that occur in special class of materials.[1] Under uniform illumination, light-to-electricity conversion is induced in spatially homogeneous ferroelectrics.[2-4] BPVE takes the advantage of the crystal asymmetry of ferroelectrics to separate the photoexcited charge carries before making their way to the electrodes. This implies that photocurrent is generated in the bulk of the active layer and above-bandgap-photovoltages can be achieved, unlike conventional photovoltaics.[5-9] Thus, solar cells based on BPVE are regarded as a promising alternative to exceed the Shockley-Queisser (SQ) limit.[10] On the other hand, there is a widely accepted argument that Schottky diodes form at the ferroelectric/metal electrodes and can provide additional photoexcited charge separation platform.[11-13] Additionally, such interface-induced photovoltaic effect is switchable following the polarization reversal.[14-16] Similarly, BPVE is switchable since the noncentrosymmetry can be reversed by external electric fields. Hence, the two phenomena are likely to coexist in ferroelectric capacitors making it challenging to disentangle the effects. This raised a controversy in the scientific community on the origin of the photovoltaic output in ferroelectric thin films. This dissertation is concerned about exploring the origin(s) of the ferroelectric photovoltaic effects in vertical cells.

The material system centered in this research is the prototypical ferroelectric bismuth ferrite ($BiFeO_3$) which offers a rich platform to investigate the ferroelectric photovoltaic. In terms of pseudo-cubic (pc) coordinates, it crystallizes in the rhombohedral space group R3c (lattice parameters a_{pc} = 3.965 Å, α_{pc} = 89.4 ◦). BFO possesses spontaneous polarization towards $<111>_{pc}$ with remnant polarization P_r = 100 μC/cm^2.[17] On the other hand, it has been shown that $BiFeO_3$ exhibits uniaxial optical anisotropy which coincides on the polar axis, i.e., $[111]_{pc}$. In other words, linearly polarized light would undergo linear dichroism and birefringence in BFO films.[18,19] Thus, anisotropic absorption should be taken into consideration when measuring polarized-light-induced PV effects.

First, the foundational properties are investigated in the device under test. For this a (001)-oriented $BiFeO_3$ monodomain are successfully grown by Pulsed Laser deposition (PLD) establishing a single crystal thin film (or epitaxial thin film). For the purpose of electrical measurements, BFO films were sandwiched between metallic electrodes. The metallic oxide, $La_{0.7}Sr_{0.3}MnO_3$, was employed as bottom electrode while platinum is used as top electrode. The surface topography was measured by means of Atomic Force Microscope

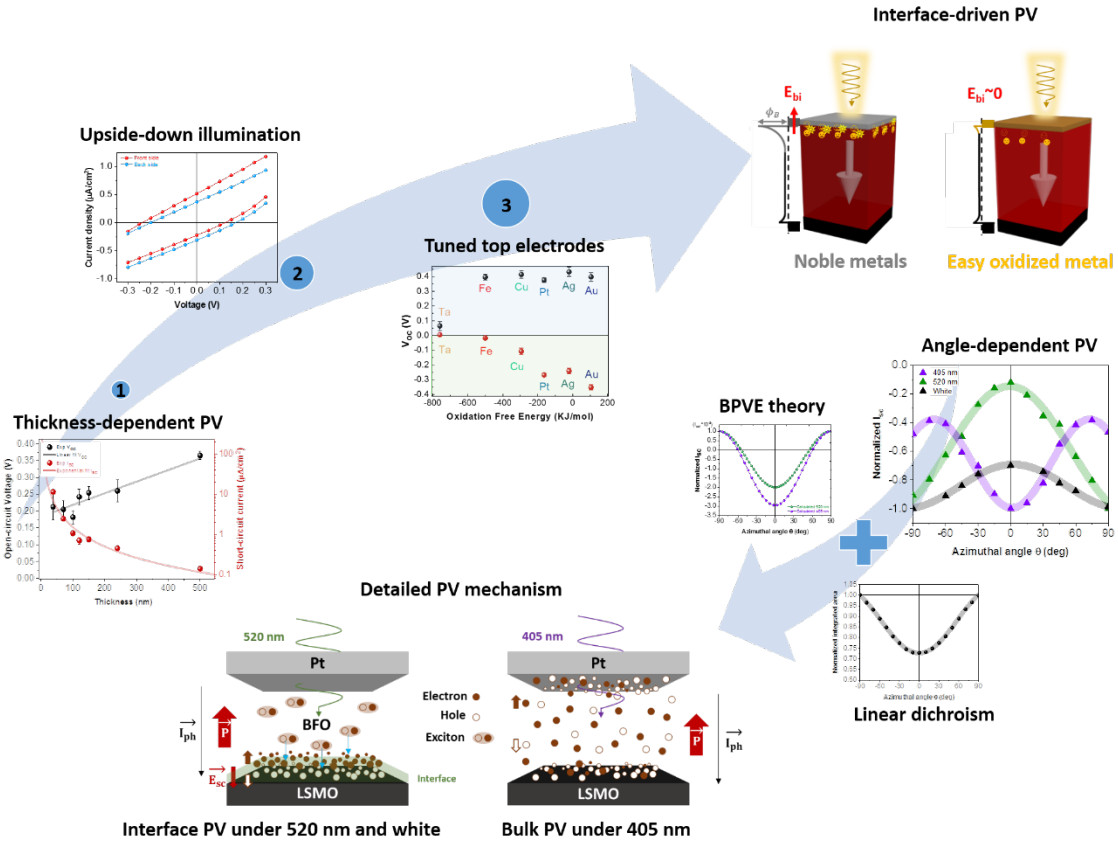

Figure 6.1: Summary of the findings in this PhD dissertation. This dissertation researches the photovoltaic mechanism in vertical $BiFeO_3$ heterostructures. Adopting white light yields photovoltaic output dominated by the interface band-bending at the $BiFeO_3$/metal. Three experimental strategies were designed including thickness-dependent PV, upside-down illumination and tuning the top electrode material. In addition, noble metals are recommended to be used with $BiFeO_3$ for maximized performance. Exploiting linearly polarized lights confirms the hypothesis that interface band-bending dominates the overall output by illuminating the cell by white light. In contrast, above-bandgap illumination gave rise to bulk photovoltaic action in which the interface PV still presents.

(AFM) revealing the distinctive sawtooth features of monodomain BFO. Additionally, the crystal structure was probed using High-Resolution X-Ray Diffraction (HRXRD) ensuring a phase-pure material and providing the crystal lattice parameters. Finally, the ferroelectric property was explored by complementary microscopic and macroscopic experiments. The Piezoresponse Force Microscope (PFM) revealed monodomain ferroelectric structure of the BFO films used in this thesis. Also, the polarization-electric field hysteresis measurements demonstrated square-like shape and well-saturated loops. Having established the structural and ferroelectric characteristics, the photovoltaic properties are then investigated adopting several strategies. Figure 6.1 summarizes the results revealed in this dissertation.

Upon illumination by white light, it was found that the interface band-bending at the interface dominates the photovoltaic output of Pt/BFO/LSMO vertical capacitors. The polarization reversal is found to modulate Schottky barrier height yielding a modulated photovoltaic effect. This was concluded based on experimental tuning of the size of the active layer (thicknesses between 38 nm and 500 nm were used). Interestingly, the photocurrent showed exponential decay as BFO layer thickness increases. Surprisingly, the photocurrent was enhanced by one order-of-magnitude in the 38 nm film which predicts the domination of interface-induced PV mechanism. Also, by comparing the photovoltaic output of the cell illuminated from front- and backsides, the collected IV curves showed a horizontal shift. As a further step, the top interface was tuned by employing different metallic materials. In fact, different metals varied the nature of the top interface leading to a Schottky-to-ohmic modulation as revealed by the dark transport measurements. Once more, the photovoltaic performance was greatly affected for different top electrodes. Specifically, the device with ohmic contact showed almost null photovoltaic performance emphasizing the role of Schottky barrier on deciding the photovoltaic output. However, monitoring the evolution of open-circuit voltage V_{oc} with BFO thickness pointed to a linear behavior which signifies a trace of bulk photovoltaic effect. This motivated the next research line.

As a follow-up of the previous work on the photovoltaic mechanism in vertical-type ferroelectric capacitors, linearly polarized lights were utilized. The aim is to investigate the existence of bulk photovoltaic mechanism, if any, by tensorial nature. Interestingly, white, 520 nm and 405 nm lights gave rise to oscillated photocurrents. Also, examining the bulk photovoltaic theory enabled the discrimination of bulk and interface PV effects. On the one hand, the above-bandgap illumination leads to dominating BPVE mechanism with minor contribution from interface band-bending. On contrary, white light and below-bandgap illumination gave rise to photovoltaic effects dominated by the interface band-bending.

This doctoral work not only provides new understanding of the light-matter interaction in photoferroelectrics, but also opens up new possibilities for real-life applications. The angle-resolved photocurrents measurements demonstrate sinusoidal behaviors leading to BPVE and linear dichroism in which a phase shift of 90^{o} between the two waves exists. Consequently, and having distinguished the competitive anisotropies in monodomain $BiFeO_3$ films, an application towards building light polarization detectors can be achieved.

6.2 Future work

Based on the research outcome in this dissertation, several research lines can be suggested extending the fundamental exploration of the origin of ferroelectric photovoltaic effects in vertical configurations. Regardless of the microscopic mechanism, bulk photovoltaic effects can be distinguished according to the research conducted in this work. However, optimization of the BPVE-based solar cell is crucial to exploit the full potential of ferroelectric photovoltaic in applications. Consequently, a natural progression of this work is to gain more details regarding intrinsic and extrinsic characteristics as follows.

When it comes to photo-induced phenomena, device size matters. It was experimentally shown that efficiency of photovoltaic effects is significantly increased by using Atomic Force Microscope metallic tip as a top electrode. This was demonstrated in $BiFeO_3$ single crystal and $BaTiO_3$ epitaxial films which, in turn, shed the light on the role of size effects on the BPVE.[20,21] In fact, the tip apex in contact with the ferroelectric layer allows shrunken

contact area (a). However, it should be noted that bringing AFM tip in contact with ferroelectric material might induce strain gradients or even polarization enhancement adding more complexities.[22,23] To carefully analyze this, a systematic experimental study is to be conducted to monitor the PV output with deposited top electrodes in which sizes ranging from a >> d to a << d can be tuned. Apparently, the photovoltaic effect should be measured by means of linearly polarized light in order to distinguish the bulk PV mechanism. Furthermore, the size of the ferroelectric layer d can be tuned while the top electrode size remained constant. Hence, the PV cell can be optimized to work in the bulk PV regime which is determined by the mean free path of the charge carriers.

Although the bulk photovoltaic effect was revealed in this work, the microscopic mechanism was not elucidated. As explained in chapter 2, the bulk photovoltaic theory has

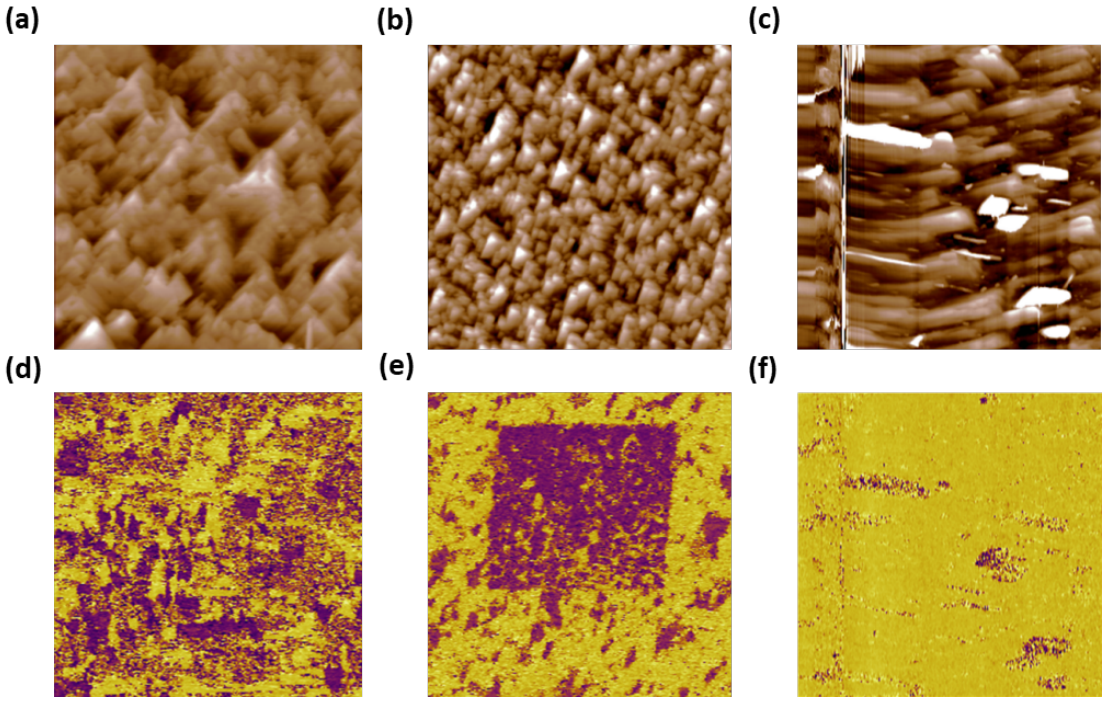

Figure 6.2: Topography and PFM images of Bi_2FeCrO_6 thin films. Topography of BFCO grown in mixed oxygen/argon 1Pa/0Pa **(a)**, 1Pa/6Pa **(b)** and 1Pa/9Pa **(c)**. In-plane PFM phase signal at oxygen/argon 1Pa/0Pa **(d)**, 1Pa/6Pa **(e)** and 1Pa/9Pa **(f)**.

proposed two possible mechanisms: ballistic and shift currents. The former involves the asymmetric distribution of the momenta of hot charge carriers in k-space. Shift currents is

associated with the shift of the charge carriers in real space yielding electric currents. However, differentiating these mechanisms is challenging. Indeed, the ballistic current can be disentangled through probing the photo-Hall effects which involves applying external magnetic field while probing photocurrents. One should be cautious with this experiment since $BiFeO_3$ possesses weak ferromagnetism that can confuse the results. On the other hand, shift current can be probed by circularly polarized light which requires the noncentrosymmetric crystal to be of gyrotropic nature. Unfortunately, BFO lacks this property and the search for other gyrotropic crystal is needed.

6.2.1 Photovoltaic effects beyond $BiFeO_3$

Another potential research direction is improving the absorption process. Even though $BiFeO_3$ is a fabulous material from both the optical and ferroelectric aspects to study photovoltaic effects, the bandgap is relatively high compared to conventional semiconductors such as Si. Nevertheless, in 2015, researchers developed photovoltaic cell comprising the double perovskite Bi_2FeCrO_6 (BFCO) which gave rise to power conversion efficiency of 3.3 %.[24] In this complex oxide, the unit cell consists of two neighboring perovskites connected at corners in which each contain either Fe^{3+} or Cr^{3+} cations. Grown by pulsed laser deposition technique, the deposition conditions can be tuned leading to ordered/disordered regions in the same crystal. The researchers succeeded to tune the bandgap from 1.4 eV to 2.1 eV. Consequently, BFCO is even a more intriguing ferroelectric system to investigate photovoltaic effects towards solar cell applications. However, BFCO suffers from polar instability, i.e., the rotation of ferroelectric polarization in space.[24-26] Here, preliminary results are introduced with aim to stabilize the ferroelectric polarization since the usage of polarized light requires a well-defined ferroelectric direction.

The polarization rotation may be attributed to the low oxygen pressure window (~ 1 Pa) during PLD growth.[27] As a matter of fact, the role of oxygen gas in PLD chamber during the film growth is threefold; compensation for oxygen loss, oxidation of the constituent cations and controlling the ions kinetic energies. Here, argon gas is mixed with oxygen in the PLD chamber with the aim to increase the total pressure during the deposition while maintaining the stoichiometry as Bi_2FeCrO_6 since Ar is nonreactive. For this, BFCO grown on miscut STO covered by LSMO. The substrate temperature is kept at 650 C, oxygen pressure at 1 Pa while argon pressure was tuned from 0 Pa, 6 Pa to 9 Pa. Also, the growth time is maintained at 20 min.

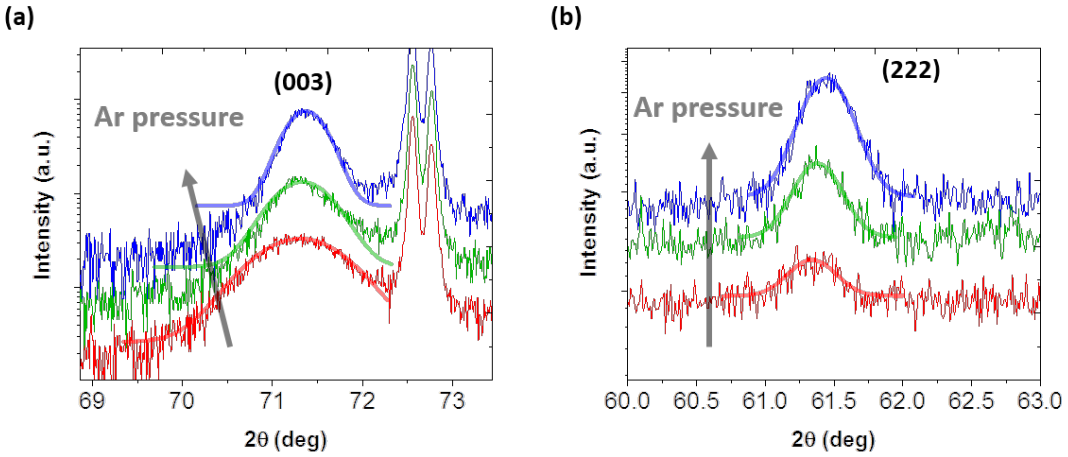

Figure 6.3: X-ray diffraction results of the samples series. **(a)** Symmetric 2θ-ω scan around (003) peak. **(b)** Asymmetric 2θ-ω scan around (222) peak.

As shown in figure 6.2 (d), the in-plane PFM phase signal indicates random orientations. Upon adding 6 Pa argon gas, the majority of the polarization stabilize following the substrate miscut direction. Ultimately, at 1 Pa/9 Pa oxygen/argon gas pressure, the measured signal points to a monodomain ferroelectric structure. By means of HRXRD, the symmetric 2θ-ω scan shows improved crystallinity as the argon pressure increases (here, (003) peak FWHM becomes narrower although shrunken thickness is expected as the argon increases in the chamber environment). In figure 6.3 (b), the asymmetric XRD scan around (222) is presented which again indicates the enhancement of the peak as Ar pressure increases. This result implies the improvement of the Fe/Cr cationic ordering which is associated with the bandgap tuning.[24] Apparently, the results should be complemented by the optical measurements. Figure 6.4 (a) shows the direct bandgap curves obtained from

the experimental absorption curves. By extracting the direct bandgap values, figure 6.4 (b), the bandgap reduced from 2 eV (0 Pa Ar) to 1.82 eV (9 Pa Ar).

Although the current results show promising approach to stabilize the ferroelectric polarization in BFCO, the study is limited by the lack of macroscopic polarization-electric

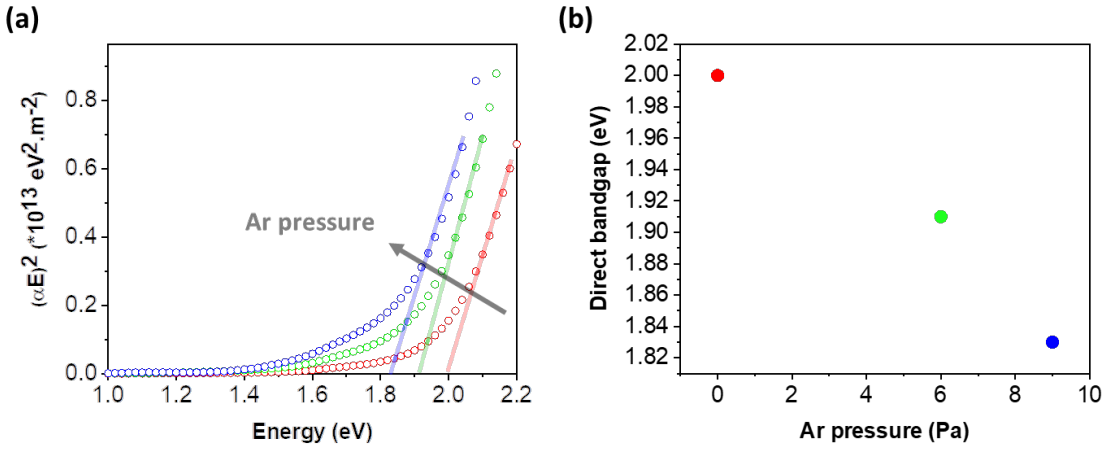

Figure 6.4: Direct bandgap of the BFCO series. **(a)** Direct bandgap plot. **(b)** Extracted bandgap values.

field loops. Hence, scaling up the film thickness is crucial for such macroscopic measurements in addition to exploring the photovoltaic effects. Also, future trials should assess the individual photovoltaic processes; light absorption, electron-hole separation and charge carriers transport to the electrodes. The findings of this intriguing project not only open up a new direction towards discover the origin of the photovoltaic effects in noncentrosymmetric crystals but may also lead to commercial solar cells considering the narrow bandgap of Bi_2FeCrO_6.

6.3 Organic-inorganic ferroelectrics

Hybrid organic-inorganic perovskites (HOIPs) have shown their great potential in solar cell applications.[28,29] This class of materials is chemically described by the ABX_3 formula where A and B are the organic and metal cations, respectively, and X is the halogen ion.[30] From the optoelectronic point of view, HOIPs are characterized by narrow bandgaps, long carrier diffusion lengths and large absorption coefficient.[31-33] Furthermore, it is widely believed that ferroelectricity in HOIPs might lie at the heart of its outstanding performance

in solar cells.[34-36] First-principles calculations showed that $CH_3NH_3PbI_3$ generates shift current comparable to $BiFeO_3$ despite their smaller ferroelectric polarization (~5 μC/cm^2).[37] Understanding the BPVE mechanism in hybrid perovskite may lead to a cooperative interface/bulk photovoltaics enhancing the overall power conversion efficiency. In particular, HOIP ferroelectrics are also attractive for ferroelectric photovoltaic applications owing to the combined spontaneous polarization and tunable bandgap. For example, organic-inorganic ferroelectrics including [R- and S-1-(4-chlorophenyl)ethylammonium]$_2PbI_4$[38], (4-(aminomethyl)piperidinium)PbI_4[39] and $(C_4H_9NH_3)_2(CH_3NH_3)_2Pb_3Br_{10}$[40] offer an intriguing platform for investigating the BPVE mechanism which further enhance our understanding of such fascinating phenomenon.

References

1. Sturman, B. I. & Fridkin, V. M. *Photovoltaic and Photo-refractive Effects in Noncentrosymmetric Materials*. Vol. 8 (CRC Press, 1992).

2. Young, S. M. & Rappe, A. M. First principles calculation of the shift current photovoltaic effect in ferroelectrics. *Physical review letters* **109**, 116601 (2012).

3. Fridkin, V. Bulk photovoltaic effect in noncentrosymmetric crystals. *Crystallography Reports* **46**, 654-658 (2001).

4. Tan, L. Z. *et al.* Shift current bulk photovoltaic effect in polar materials—hybrid and oxide perovskites and beyond. *Npj Computational Materials* **2**, 1-12 (2016).

5. Fridkin, V. *Photoferroelectrics*. (Springer-Verlag Berlin Heidelberg New York, 1979).

6. Kim, D. J. & Alexe, M. Bulk photovoltaic effect in monodomain $BiFeO_3$ thin films. *Applied Physics Letters* **110**, doi:10.1063/1.4983032 (2017).

7. Bhatnagar, A., Roy Chaudhuri, A., Heon Kim, Y., Hesse, D. & Alexe, M. Role of domain walls in the abnormal photovoltaic effect in $BiFeO_3$. *Nature Communications* **4**, doi:10.1038/ncomms3835 (2013).

8. Matsuo, H. *et al.* Bulk and domain-wall effects in ferroelectric photovoltaics. *Physical Review B* **94**, doi:10.1103/PhysRevB.94.214111 (2016).

9. Matsuo, H., Noguchi, Y. & Miyayama, M. Gap-state engineering of visible-light-active ferroelectrics for photovoltaic applications. *Nat Commun* **8**, 207, doi:10.1038/s41467-017-00245-9 (2017).

10. Shockley, W. & Queisser, H. J. Detailed balance limit of efficiency of p-n junction solar cells. *Journal of applied physics* **32**, 510-519 (1961).

11. Blom, P. W., Wolf, R. M., Cillessen, J. F. & Krijn, M. P. Ferroelectric Schottky diode. *Phys Rev Lett* **73**, 2107-2110, doi:10.1103/PhysRevLett.73.2107 (1994).

12. Pintilie, L. & Alexe, M. Metal-ferroelectric-metal heterostructures with Schottky contacts. I. Influence of the ferroelectric properties. *Journal of Applied Physics* **98**, doi:10.1063/1.2148622 (2005).

13. Pintilie, L. *et al.* Metal-ferroelectric-metal structures with Schottky contacts. II. Analysis of the experimental current-voltage and capacitance-voltage characteristics of $Pb(Zr,Ti)O_3$ thin films. *Journal of Applied Physics* **98**, doi:10.1063/1.2148623 (2005).

14. Tan, Z. *et al.* Thinning ferroelectric films for high-efficiency photovoltaics based on the Schottky barrier effect. *NPG Asia Materials* **11**, doi:10.1038/s41427-019-0120-3 (2019).

15. Guo, R. *et al.* Non-volatile memory based on the ferroelectric photovoltaic effect. *Nat Commun* **4**, 1990, doi:10.1038/ncomms2990 (2013).

16. Lee, D. *et al.* Polarity control of carrier injection at ferroelectric/metal interfaces for electrically switchable diode and photovoltaic effects. *Physical Review B* **84**, 125305, doi:10.1103/PhysRevB.84.125305 (2011).

17. Catalan, G. & Scott, J. F. Physics and Applications of Bismuth Ferrite. *Advanced Materials* **21**, 2463-2485, doi:10.1002/adma.200802849 (2009).

18. Schmidt, D., You, L., Chi, X., Wang, J. & Rusydi, A. Anisotropic optical properties of rhombohedral and tetragonal thin film $BiFeO_3$ phases. *Physical Review B* **92**, doi:10.1103/PhysRevB.92.075310 (2015).

19. Choi, S. G. *et al.* Optical anisotropy and charge-transfer transition energies in BiFeO3 from 1.0 to 5.5 eV. *Physical Review B* **83**, doi:10.1103/PhysRevB.83.100101 (2011).

20. Alexe, M. & Hesse, D. Tip-enhanced photovoltaic effects in bismuth ferrite. *Nature communications* **2**, 1-5 (2011).

21. Spanier, J. E. *et al.* Power conversion efficiency exceeding the Shockley–Queisser limit in a ferroelectric insulator. *Nature Photonics* **10**, 611-616, doi:10.1038/nphoton.2016.143 (2016).

22. Yang, M.-M., Kim, D. J. & Alexe, M. Flexo-photovoltaic effect. *Science* **360**, 904-907, doi:10.1126/science.aan3256 (2018).

23. Wang, L. *et al.* Flexoelectronics of centrosymmetric semiconductors. *Nature Nanotechnology* **15**, 661-667, doi:10.1038/s41565-020-0700-y (2020).

24. Nechache, R. *et al.* Bandgap tuning of multiferroic oxide solar cells. *Nature Photonics* **9**, 61-67, doi:10.1038/nphoton.2014.255 (2014).

25. Nechache, R. *et al.* Growth, structure, and properties of epitaxial thin films of first-principles predicted multiferroic Bi_2FeCrO_6. *Applied Physics Letters* **89**, doi:10.1063/1.2346258 (2006).

26. Huang, W. *et al.* Multiferroic Bi2FeCrO6 based p–i–n heterojunction photovoltaic devices. *Journal of Materials Chemistry A* **5**, 10355-10364, doi:10.1039/c7ta01604b (2017).

27. Nechache, R. *et al.* Epitaxial thin films of the multiferroic double perovskite Bi_2FeCrO_6 grown on (100)-oriented $SrTiO_3$ substrates: Growth, characterization, and optimization. *Journal of Applied Physics* **105**, 061621, doi:10.1063/1.3073826 (2009).

28. Köhnen, E. *et al.* Highly efficient monolithic perovskite silicon tandem solar cells: analyzing the influence of current mismatch on device performance. *Sustainable Energy & Fuels* **3**, 1995-2005 (2019).

29. Zhang, Y. *et al.* Achieving reproducible and high-efficiency (> 21%) perovskite solar cells with a presynthesized $FAPbI_3$ powder. *ACS Energy Letters* **5**, 360-366 (2019).

30. Zhang, F., Wang, S., Li, X. & Xiao, Y. Recent progress of perovskite solar cells. *Curr. Nanosci* **12**, 137-156 (2016).

31. Xing, G. *et al.* Long-range balanced electron-and hole-transport lengths in organic-inorganic $CH_3NH_3PbI_3$. *Science* **342**, 344-347 (2013).

32. Stoumpos, C. C., Malliakas, C. D. & Kanatzidis, M. G. Semiconducting tin and lead iodide perovskites with organic cations: phase transitions, high mobilities, and near-infrared photoluminescent properties. *Inorganic chemistry* **52**, 9019-9038 (2013).

33. Wehrenfennig, C., Eperon, G. E., Johnston, M. B., Snaith, H. J. & Herz, L. M. High charge carrier mobilities and lifetimes in organolead trihalide perovskites. *Advanced materials* **26**, 1584-1589 (2014).

34. Nandi, P., Topwal, D., Park, N.-G. & Shin, H. Organic-inorganic hybrid lead halides as absorbers in perovskite solar cells: a debate on ferroelectricity. *Journal of Physics D: Applied Physics* **53**, 493002 (2020).

35. Seol, D. *et al.* Screening effect on photovoltaic performance in ferroelectric $CH_3NH_3PbI_3$ perovskite thin films. *Journal of Materials Chemistry A* **3**, 20352-20358 (2015).

36. Seol, D. *et al.* Origin of hysteresis in $CH_3NH_3PbI_3$ perovskite thin films. *Advanced Functional Materials* **27**, 1701924 (2017).

37. Zheng, F., Takenaka, H., Wang, F., Koocher, N. Z. & Rappe, A. M. First-Principles Calculation of the Bulk Photovoltaic Effect in $CH_3NH_3PbI_3$ and $CH_3NH_3PbI_{3-x}Cl_x$. *The Journal of Physical Chemistry Letters* **6**, 31-37, doi:10.1021/jz502109e (2015).

38. Yang, C. K. *et al.* The first 2D homochiral lead iodide perovskite ferroelectrics:[R-and S-1-(4-chlorophenyl) ethylammonium]$_2PbI_4$. *Advanced Materials* **31**, 1808088 (2019).

39. Park, I.-H. *et al.* Ferroelectricity and Rashba effect in a two-dimensional Dion-Jacobson hybrid organic–inorganic perovskite. *Journal of the American Chemical Society* **141**, 15972-15976 (2019).

40. Li, L. *et al.* Tailored engineering of an unusual $(C_4H_9NH_3)_2(CH_3NH_3)_2Pb_3Br_{10}$ two-dimensional multilayered perovskite ferroelectric for a high-performance photodetector. *Angewandte Chemie* **129**, 12318-12322 (2017).